Sustainable Energy & Fuels

ROYAL SOCIETY OF CHEMISTRY

REVIEW

View Article Online
View Journal

Check for updates

Cite this: DOI: 10.1039/d6se00363j

Nickel-based electrocatalysts for hydrogen production through hydrazine electrolysis

Irsa Tariq,†[a] Waheed Iqbal,†[b] Maham Almas,[c] Arslan Hameed,[a] Ali Haider,[c] C. Richard A. Catlow,[def] Jamal Abdul Nasir *[d] and Peng Li *[ag]

Hydrazine-coupled electrolysis (OHzS) offers an energy-efficient route for hydrogen production by replacing the sluggish oxygen evolution reaction (OER) with the faster hydrazine oxidation reaction (HzOR, $E° = -0.33$ V *vs.* Reversible Hdrogen Electrode (RHE)). This approach significantly lowers cell voltage and yields environmentally benign byproducts (N_2 and H_2O), making it promising for green energy applications. However, the multistep proton-coupled electron transfer process in HzOR necessitates the development of highly active, stable, and cost-effective electrocatalysts. Nickel-based materials stand out due to their earth abundance, tunable Ni^{2+}/Ni^{3+} redox chemistry, excellent conductivity, and strong hydrazine affinity. This review summarises recent advances in Ni-based catalysts, including alloys, oxides, hydroxides, phosphides, nitrides, chalcogenides, and MOFs, emphasising synthesis strategies, hierarchical architectures, and key activity enhancement mechanisms such as synergistic effects, electronic structure modulation, defect engineering, and interfacial coupling. Insights from experiments and Density Functional Theory (DFT) calculations are discussed to elucidate reaction pathways and guide bifunctional catalyst design for concurrent HzOR and HER. Additionally, the integration of machine learning (ML) is highlighted as a promising approach to accelerate catalyst discovery and optimisation. We conclude with future directions toward scalable, high-performance, and low-voltage hydrogen generation by uniting mechanistic understanding, materials design, and predictive modelling.

Received 29th March 2026
Accepted 6th May 2026

DOI: 10.1039/d6se00363j

rsc.li/sustainable-energy

Open Access Article. Published on 12 May 2026. Downloaded on 6/5/2026 6:21:18 AM.
This article is licensed under a Creative Commons Attribution 3.0 Unported Licence.

1 Introduction

The transition from fossil fuels to renewable energy is critical for sustainable development, and hydrogen-based energy has emerged as a leading candidate due to its high energy density and zero-emission potential.[1,2] While hydrogen can be produced through various methods, water electrolysis has distinct advantages because of water's abundance and ease of storage.[3] Conventional water splitting involves two key reactions: the hydrogen evolution reaction (HER) at the cathode and oxygen evolution reaction (OER) at the anode.[4–6] However, OER's sluggish kinetics result in high overpotentials (1.8–2.0 V), significantly exceeding the thermodynamic minimum of 1.23 V *vs.* RHE. This inefficiency increases energy consumption and operational costs, driving the search for alternative strategies.[7,8]

To overcome the limitations of OER, researchers have explored substituting it with thermodynamically favourable oxidation reactions, such as those involving ammonia, urea, or hydrazine.[9–12] Among these, hydrazine oxidation reaction (HzOR) offers exceptional advantages due to its remarkably high energy density (5.4 kWh L^{-1}, 1 atm), and is fully miscible in water.[13] Moreover, hydrazine has a very low theoretical oxidation potential (−0.33 V *vs.* RHE), drastically reducing energy input compared to OER.[14] It is important to note that although the overall cell reaction may be formally written to resemble hydrazine splitting, the hydrogen detected as H_2 is produced at the cathode *via* the conventional HER from water. Hydrazine is oxidised exclusively at the anode, where it serves as an electron donor and replaces the oxygen evolution reaction, thereby lowering the anodic overpotential and overall energy consumption. Additionally, HzOR produces only nitrogen and water as byproducts, eliminating the risk of hazardous gas mixtures and simplifying hydrogen purification.[15] From a practical perspective, hydrazine is already produced on a large industrial scale *via* established processes such as the Raschig and peroxide routes and is widely used in pharmaceuticals,

[a]School of Materials Science and Engineering, Anhui University, Hefei, Anhui 230601, PR China. E-mail: peng-li@ahu.edu.cn

[b]Key Laboratory of Precision and Intelligent Chemistry, Department of Chemistry, University of Science and Technology of China, Hefei, Anhui, 230026, China

[c]Department of Chemistry, Quaid-i-Azam University, Islamabad, Pakistan

[d]Kathleen Lonsdale Materials Chemistry, Department of Chemistry, University College London, 20 Gordon Street, London, WC1H 0AJ, UK. E-mail: jamal.nasir.18@ucl.ac.uk

[e]UK Catalysis Hub, Research Complex at Harwell, Rutherford Appleton Laboratory, R92 Harwell, Oxfordshire OX11 0FA, UK

[f]Cardiff Catalysis Institute, School of Chemistry, Cardiff University, Cardiff CF103AT, UK

[g]Key Laboratory of Structure and Functional Regulation of Hybrid Materials, Ministry of Education, Anhui Province Key Laboratory of Chemistry for Inorganic/Organic Hybrid Functionalized Materials, Anhui University, Hefei 230601, PR China

† Irsa Tariq and Waheed Iqbal contributed equally to this work.

Open Access Article. Published on 12 May 2026. Downloaded on 6/5/2026 6:21:18 AM. This article is licensed under a Creative Commons Attribution 3.0 Unported Licence.

agrochemicals, polymers, and aerospace applications.[16] In addition, hydrazine frequently appears as a hazardous contaminant in industrial wastewater streams. Integrating hydrazine oxidation into electrolysis systems, therefore, offers a dual benefit of energy-efficient hydrogen production and simultaneous remediation of hydrazine-containing effluents.

Despite its advantages, HzOR suffers from sluggish reaction kinetics due to its complex four-electron transfer mechanism, necessitating highly active catalysts.[17] Noble metals like Pt, Rh and Ru exhibit excellent catalytic performance for HzOR, but their high cost and scarcity limit their practical application.[18,19] To this end, transition metal-based catalysts, particularly nickel (Ni), have emerged as promising alternatives due to their low cost and abundant nature.[20] They exhibit excellent stability in alkaline conditions and efficient redox cycling due to their multiple oxidation states (Ni^{2+}/Ni^{3+}).[21,22] Their strong hydrazine adsorption and tunable electronic structure further enhance performance.[23] Several Ni-based materials, including foams,[24] alloys,[25,26] oxides/hydroxides,[24] phosphides,[23,25] sulfides,[27] selenides,[28] layer double hydroxides[29] and metal–organic frameworks,[30] have shown superior electrocatalytic activity in both monofunctional and bifunctional systems. These materials combine high mechanical strength, thermal stability, electrochemical activity and conductivity, making them ideal for energy-related applications.[31]

Recent breakthroughs in hydrazine-assisted hydrogen production highlight the potential of Ni-based catalysts. For example, Zhu *et al.* developed Ni–C hybrid nanosheets, which demonstrated record-low operational voltages (−0.037 V for HER and −0.020 V for HzOR at 10 mA cm^{-2}), enabling hydrazine-assisted electrolysis at just 0.14 V for 50 mA cm^{-2}.[32] The Ni(Cu) CNP catalyst achieved low overpotentials of 41 mV for HER and −18 mV for HzOR at 10 mA cm^{-2}, enabled by its hierarchical nanoporous structure and optimised electronic configuration.[33] More recently, superhydrophilic Ni-based nanorod-nanoflake arrays (Ni-NCNA) were shown to require only −26 mV for HzOR and 47 mV for HER at 10 mA cm^{-2}. When integrated into a hydrazine-assisted seawater electrolyser powered by a waste AAA battery (1.5 V), this system achieved a hydrogen production rate of 1.074 mmol h^{-1} at an ultralow cell voltage of 0.485 V.[34]

The advances in Ni-based HzOR catalysts have stimulated substantial research into understanding their development, as highlighted in several key review articles: Liu *et al.* examined transition metal catalysts for hydrazine-assisted water splitting,[35] while Khalafallah *et al.* (2020) focused on Ni-based electrocatalysts for direct hydrazine fuel cells.[36] More recently, Tong *et al.* (2024) and Li *et al.* (2025) provided updated perspectives on electrocatalyst development and hydrogen production *via* hydrazine-assisted electrolysis, respectively.[13,37] Similarly, Yu *et al.* (2025) further expanded on performance enhancement strategies and application potential.[38]

Despite these several recent reviews mentioned above on hydrazine-assisted hydrogen production, a unified perspective that integrates reaction mechanisms, catalyst classification, activity enhancement strategies, and data-driven design principles remains lacking. In this review, we focus first on fundamental mechanisms of hydrazine coupled electrolysis across different pH environments, followed by an analysis of fabrication methods and activity enhancement strategies for Ni-based catalysts. The article subsequently explores advances in various Ni-based electrocatalysts, including oxides/hydroxides, sulfides/phosphides, selenides/nitrides, alloys, and metal–organic frameworks. Special attention is given to catalytic enhancement mechanisms, including interface engineering, electronic structure modulation, and defect engineering. The review also introduces the emerging paradigm of machine learning in electrocatalysis, drawing lessons from HER and OER to propose a framework for data-driven catalyst discovery in HzOR. The concluding sections present design principles derived from literature and future perspectives, with particular focus on breakthroughs from the past five years. By consolidating these multidisciplinary developments, we aim to assist innovation in Ni-based catalyst design for energy-efficient hydrogen production through both traditional materials science and cutting-edge computational approaches.

2 Hydrazine-assisted electrochemical reaction, safety and mechanisms

Hydrazine-coupled electrolysis (OHzS) presents a highly efficient approach for hydrogen generation by integrating the HER at the cathode and HzOR at the anode, which we discuss later in this section after describing in more detail the anodic and cathodic processes.

2.1 Safety considerations

Although hydrazine-coupled electrolysis offers a compelling route to low-voltage hydrogen production, its wider deployment must be assessed in light of the intrinsic hazards associated with hydrazine itself.[39] Furthermore, it is a highly reactive and toxic reductant; authoritative safety agencies identify it as hazardous by inhalation, skin contact, and ingestion, and note its flammability, corrosivity, and ready skin absorption.[40]

2.1.1 Minimized hazardous inventory *via* high catalyst activity. The most direct way to reduce hydrazine risk is to minimize the amount present in the system at any time, achieved through catalysts with high activity at low hydrazine concentrations. State-of-the-art Ni-based catalysts perform exceptionally well at concentrations as low as 0.1–0.3 M. For example, Ni–C HNSA achieves 50 mA cm^{-2} with only 0.1 M N_2H_4,[38] while Ni/NCNFs-Rh delivers 10 mA cm^{-2} using 0.5 M N_2H_4.[41] This high low-concentration activity enables operation with dilute feed streams (*e.g.*, directly from industrial wastewater), reducing the hazardous hydrazine inventory by orders of magnitude compared to systems requiring concentrated storage. Key catalyst design strategies enhancing low-concentration activity include defect engineering (oxygen vacancies in NiIr-BDC MOF),[42] single-atom catalysts (Ni SACs on MXene),[43] and heterostructure interfaces (Ni_3N–Co_3N).[44]

2.1.2 Intensified flow configurations *via* engineered wettability. Intensified flow configurations—such as microchannel reactors and flow-through electrodes—reduce

Open Access Article. Published on 12 May 2026. Downloaded on 6/5/2026 6:21:18 AM. This article is licensed under a Creative Commons Attribution 3.0 Unported Licence.

residence time and hydrazine inventory but require catalysts with optimised surface wettability. Several Ni-based catalysts exhibit superhydrophilic and superaerophobic properties that enable such configurations. Ni NCNA shows a contact angle of approximately 0° and bubble-repelling behaviour, enabling rapid gas release in flow-through operation.[34] Similarly, Ni/Ni_3S_4/1T-MoS_3/CC achieves superhydrophilic/superaerophobic surfaces for seawater electrolysis at only 17 mV overpotential,[45] and Ni–Zn–Cu/Ni foam achieves near-zero contact angle *versus* 123° for bare Ni foam.[46] These properties enable rapid electrolyte penetration, fast bubble detachment, and reduced residence time. The combination of superhydrophilicity and superaerophobicity, achieved through hierarchical nanostructuring, simultaneously ensures electrolyte access while promoting gas release.

2.1.3 Inherently safer design *via* selective catalysis. Inherently safer design eliminates hazards rather than controlling them, requiring catalysts that completely convert hydrazine to harmless N_2 and H_2O with no residual toxicity. Several Ni-based catalysts demonstrate near-complete degradation: Mo–Ni_2-Pv@MNF achieves <5 ppb residual,[39] Fe–CoNiP@NC shows >99% removal efficiency,[47] Pt@NiFe-MOF degrades 718 ppb to 6 ppb in 120 minutes,[48] and NiCo@C/MXene/CF achieves <3 ppb residual.[49] This complete conversion relies on high selectivity for the 4-electron pathway ($N_2H_4 \rightarrow N_2$) over side reactions like NH_3 formation. Ni-based catalysts achieve this through electronic structure modulation (d-band tuning in W–Ni_3N),[50] heterointerface design (Ni_3N–Co_3N),[44] and surface reconstruction (Ni/β-Ni$(OH)_2$).[51] The output stream contains only H_2, N_2 and H_2O, eliminating downstream hydrazine removal, particularly valuable for on-site fuel cell feed.

2.1.4 Toward integrated safety-by-design. The three concepts above reinforce each other. High activity at low concentrations (minimised inventory) and high selectivity (inherently safer design) enable intensified flow configurations with smaller reactors and shorter residence times. Conversely, superhydrophilic surfaces improve mass transport, further enhancing low-concentration activity. The most promising Ni-based catalysts such as Ni–C HNSA, Ni NCNA, and Mo/Ni_2-Pv@MNF—already embody multiple aspects of this integrated framework. Future catalyst development should explicitly target this triple optimization: high dilute-concentration activity, superhydrophilic/superaerophobic surfaces, and complete 4-electron pathway selectivity.

From the perspective of catalyst and device design, these safety constraints should be seen not merely as external limitations, but as design parameters. In this regard, Ni-based electrocatalysts remain attractive because their high HzOR activity and tunable redox chemistry may enable operation at lower hydrazine concentrations, lower overpotentials, and shorter residence times, thereby potentially reducing the hazardous inventory needed in a working system.[32] However, even highly active catalysts do not eliminate the underlying toxicological and handling concerns. The real challenge for the field is therefore to couple advances in catalyst discovery, including DFT-guided design and emerging ML-assisted optimisation, with safety-by-design concepts such as minimised hydrazine inventory, intensified flow configurations, on-demand feed strategies, and integrated destruction or capture of residual hydrazine in the product stream.

2.2 Anodic HzOR

Several reviews have discussed the mechanism of hydrazine oxidation in alkaline media (pH 14).[13,35,38] However, there is a lack of comprehensive studies on reaction mechanisms in acidic and neutral media, limiting the understanding of hydrazine's behaviour across different pH conditions.

In alkaline media (*e.g.* 1 M KOH), hydrazine oxidation is highly efficient due to the presence of OH^- ions, which act as proton acceptors.[52] N_2H_4 adsorbs onto the catalyst surface and undergoes a stepwise four-electron, four-proton dehydrogenation. Each step is facilitated by OH^-, enabling gradual N–H bond cleavage and formation of intermediates like $N_2H_3^*$, $N_2H_2^*$ and N_2H^* (Fig. 1a). The removal of each hydrogen involves simultaneous electron transfer and water formation. Favourable kinetics in alkaline media therefore, result from rapid proton abstraction by OH^- and stabilised intermediates.[36] For example, the Ni_2Fe_2N/NF catalyst achieved a high current density of 1017 mA cm^{-2} at just 0.3 V *vs.* RHE with excellent stability and near-perfect $4e^-$ selectivity.[53] Similarly, the Ni@$NiP_{3.0}$/C catalyst delivered a remarkable mass activity of 2675.1 A g_{Ni}^{-1} at 0.25 V *vs.* RHE, outperforming Ni/C and Pt/C catalysts in both activity and stability.[23]

Neutral electrolytes (*e.g.*, 1 M phosphate buffer saline (PBS), ~pH 7) offer safer, more environmentally friendly conditions and better compatibility with biological and practical devices.[54] In neutral conditions, hydrazine oxidation follows the same four-electron pathway, but H_2O acts as a proton acceptor instead of OH^-. Since water is a weak base, proton abstraction is sluggish, leading to slower kinetics and high energy barriers.[55] Effective catalysis in neutral media requires materials with strong adsorption ability and efficient charge transfer. For example, in a phosphate buffer, the catalyst $Pt_{0.2}Ni_{0.8}$/C exhibited efficient electrocatalytic activity for hydrazine oxidation, delivering a current density of ~44 mA cm^{-2} and mass activity of 132 mA mg_{metal}^{-1} at 0.5 V *vs.* RHE. In alkaline media, the same catalyst achieved a TOF of 673 h and H_2 production rate of 188 L h^{-1} g_{metal}^{-1} at 50 °C with 100% H_2 selectivity.[56] In 1.0 M PBS-buffered seawater, Fe–Ni_2P/CeO_2 exhibited excellent HzOR performance with a low overpotential of 161 mV at 10 mA cm^{-2}, sustaining 200 mA cm^{-2} for 10 hours without degradation.[57] A high entropy alloy (AgAuCuPtPd) achieved 74 mA cm^{-2} at 1.13 V *vs.* RHE with gas analysis confirming 75% HzOR and 25% OER contribution.[58] Metal hexacyanoferrates (In, Co, Cu, Mn hcf) showed promising neutral HzOR performance, with Cu hcf active at 400–500 mV and In hcf at ~700 mV.[59]

In acidic media (*e.g.*, 0.5 M H_2SO_4), hydrazine oxidation proceeds *via* a stepwise proton-coupled electron transfer (PCET) mechanism, with each hydrogen removal yielding a proton (H^+) and electron, forming intermediates, including $N_2H_3^*$, $N_2H_2^*$ and N_2H^* (Fig. 1b). Unlike alkaline or neutral media, proton transfer in acidic HzOR proceeds *via* direct solvation by water molecules, forming hydronium species rather than requiring an external

Open Access Article. Published on 12 May 2026. Downloaded on 6/5/2026 6:21:18 AM.
This article is licensed under a Creative Commons Attribution 3.0 Unported Licence.

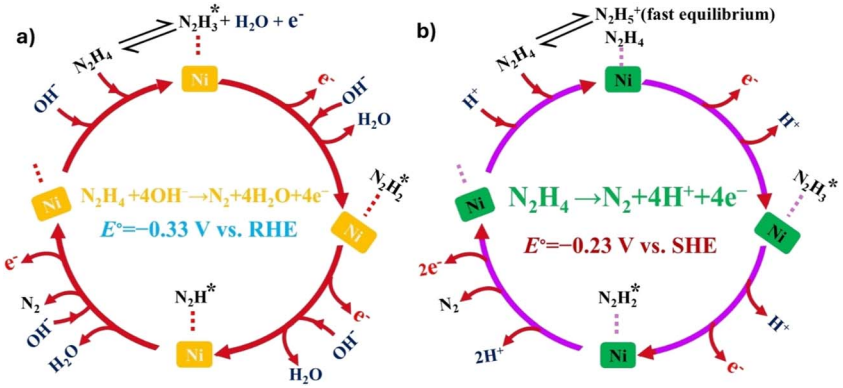

Fig. 1 Electrochemical reaction mechanism of hydrazine oxidation (a) alkaline media, (b) acidic media.

proton acceptor. Although thermodynamically favourable, HzOR in acidic media is often hindered by severe competition from cathodic HER and by poor catalyst stability under strongly acidic conditions.[60] At platinum (Pt) electrodes, hydrazine oxidation occurs directly (−0.1 to −0.2 V) or *via* PtO mediated pathways (~0.5 V), but side reactions ($3N_2H_4 + H^+ \rightarrow N_2 + 4NH_4^+$) and N_2 bubble formation reduce efficiency.[61] At gold (Au) electrodes, irreproducible behaviour arises from difficulties in oxidising the $N_2H_5^+$, while alkaline media provide consistent, efficient oxidation *via* a $4e^-$ pathway.[62] Nonetheless, Rh/RhO_x nanosheets in 0.5 M H_2SO_4 delivered efficient HzOR with 0.348 V at 10 mA cm^{-2}, outperforming Pt/C. Rh–O–Rh interfaces enhanced N–H bond weakening and reduced energy barriers. Yet, the same catalyst in alkaline conditions achieved 0.068 V at 10 mA cm^{-2}, demonstrating faster kinetics and fewer side reactions.[63] Nickel-based catalysts typically degrade into acidic media due to corrosion and HER competition, which limit their use for HzOR. However, strategies such as alloying with acid-stable metals,[64] metal oxide doping,[65,66] core–shell structures,[67,68] or carbon encapsulation[69] improve their performance and stability, enabling evaluation in acidic environments.

2.3 Cathodic HER

HER occurs at the cathode through a two-electron electrochemical reduction. While the fundamental mechanism mirrors that of conventional water splitting, the pH of the electrolyte environment significantly affects reaction kinetics and catalyst choice. HER generally proceeds through either the Volmer–Tafel or Volmer–Heyrovsky pathways.[70] The process begins with the Volmer step (eqn (1)), where a proton (or water molecule in alkaline media) accepts an electron and adsorbs onto the active site M, forming the adsorbed hydrogen intermediate M–H*:

$$H^+/H_2O + e^- + M \rightarrow M\text{–}H^* \quad (1)$$

The subsequent hydrogen evolution can occur *via* either the Heyrovsky step (eqn (2)), which involves an electrochemical desorption process:

$$M\text{–}H^* + H^+/H_2O + e^- \rightarrow M + H_2 \quad (2)$$

or the Tafel step (eqn (3)), which proceeds through a recombination of two adsorbed hydrogen intermediates to release molecular hydrogen:

$$2M\text{–}H^* \rightarrow 2M + H_2 \quad (3)$$

In acidic electrolytes, HER proceeds through proton reduction ($2M\text{–}H^* \rightarrow 2M + H_2$). High proton concentration results in fast kinetics, especially on noble metals. However, few hydrazine-assisted systems operate in acids due to hydrazine's lower stability.[13] Still, Rh/RhO_x nanosheets demonstrated bifunctional activity in all media, achieving 10 mA cm^{-2} at cell voltages of 0.068 V (alkaline), 0.268 V (neutral), and 0.348 V (acidic), with HER stability maintained for 65 h in neutral conditions.[63]

In alkaline electrolytes, HER follows water reduction ($2H_2O + 2e^- \rightarrow H_2 + 2OH^-$). The Volmer step (water dissociation) is typically rate-limiting. Catalysts must promote water activation and H* adsorption.[71] Alkaline media are preferred for HzOR due to better kinetics and stability. For example, W–O–CoP/NF achieved an HER overpotential of 185.60 mV at 1000 mA cm^{-2} and HzOR overpotential of 78.99 mV at the same current density. The full hydrazine-assisted cell operated at just 1.634 V at 100 mA cm^{-2}, much lower than conventional electrolysis.[72] In another example, a PtCo alloy nanosheet enabled HER at 0.28 V (10 mA cm^{-2}) with 3000 h durability, and in a PEM cell, hydrogen yield of 1.87 mmol h^{-1} cm^{-2} at 100 mA cm^{-2} with 60 h stability and 100% hydrazine removal.[73]

In neutral electrolytes, HER proceeds more slowly due to lower ionic conductivity and poor proton availability.[74] However, the Ru-doped α-MnO_2 PEM electrolyzer enabled energy-efficient hydrogen production in near-neutral media, achieving ultralow cell voltages of 0.254 V (10 mA cm^{-2}) and 0.935 V (100 mA cm^{-2}) in weak alkaline conditions (pH 8.3), and 0.491 V (10 mA cm^{-2}) and 1.145 V (100 mA cm^{-2}) in weak acidic conditions (pH 5.9). This hydrazine-assisted approach significantly outperforms conventional water electrolysis while maintaining excellent stability.[75]

This journal is © The Royal Society of Chemistry 2026

Open Access Article. Published on 12 May 2026. Downloaded on 6/5/2026 6:21:18 AM.
This article is licensed under a Creative Commons Attribution 3.0 Unported Licence.

Table 1 Showing the synthesis cost and toxicological handling of hydrazine

Parameter	Conventional alkaline OWS	Hydrazine-assisted OHzS (state-of-the-art)	Ref.
Typical cell voltage (V)	1.80–2.00 (at 0.5–1.0 A cm^{-2})	0.016–0.070 V (at 10–50 mA cm^{-2}): Ni/NCNFs-Rh (0.016 V), Ni–C HNSA (0.14 V at 50 mA cm^{-1}); 0.50–0.70 V (at 500–1000 mA cm^{-2}): Ni–Co–P/NF (0.498 V at 500 mA cm^{-2}), Mo–Ni_2Pv@MNF (0.571 V at 1000 mA cm^{-2}), RuC–NiCoP	32, 39, 41, 84 and 85
Electrical energy consumption (kWh per kg H_2)[1]	48–54	0.5–2.0 kWh kg^{-1} (at <100 mA cm^{-1}): 0.35 kWh m^{-1} (≈3.9 kWh kg^{-1}); 15–20 kWh kg^{-1} (at ≥500 mA cm^{-2}): 15.3 kWh kg^{-1} from 0.57 V cell; 48% reduction *vs.* OWS demonstrated at 500 mA cm^{-2} (2.75 kWh m^{-3} H_2)	39, 49 and 86
Electricity cost ($ per kg H_2)	$2.5–3.8	$0.03–0.10 (low current density): 0.43 kWh kg^{-1} $ $0.06 = $0.03 kg^{-1}; $0.8–1.2 (high current density): 15.3 kWh kg^{-1} × $0.06 = $0.92 kg^{-1}	39, 41 and 49
Hydrazine fuel cost ($ per kg H_2)	Not applicable	$25–37 (purchased pure hydrazine hydrate, stoichiometric calculation); $2.68 (reported net cost including wastewater treatment credit); $0 (if hydrazine is a free waste stream); negative (if disposal cost is avoided)	38 and 49
Total direct operating cost ($ per kg H_2)	$2.5–3.8	$2.68 (reported net cost including electricity and hydrazine); $0.8–1.5 (with waste hydrazine, electricity only)	38, 39 and 49
Capital cost multiplier *vs.* conventional OWS	1.0 (baseline)	∼1.3–1.5× (due to additional safety, containment, and monitoring systems)	40 and 87
Safety & handling requirements	H_2 explosion risk; alkaline KOH electrolyte (corrosive but manageable)	H_2 explosion + hydrazine hazards: acute toxicity (LD_{50} oral rat ≈ 60 mg kg^{-1}), carcinogenicity (group 2A, IARC), hepatotoxicity, flammability (autoignition 270 °C), corrosivity, dermal absorption. Requires closed systems, continuous monitoring, specialized materials	40, 87 and 88
Ideal application scenarios	Large-scale centralized green H_2 production; grid-integrated renewable energy; industrial electrolyzer parks	Wastewater treatment: pharmaceutical, agrochemical, polymer, aerospace effluents containing hydrazine; portable/marine power: liquid fuel logistics; self-powered systems: waste batteries (1.5 V AAA battery powered 0.485 V seawater electrolyser, 1.074 mmol h^{-1} H_2); solar-driven systems	34, 38 and 89
Energy savings *vs.* conventional OWS	Baseline (0% saving)	60–95% reduction in electrical energy consumption; 48% reduction reported at 500 mA cm^{-2} in seawater; >90% reduction reported at 150 mA cm^{-2}; >95% reduction at low current densities	32 and 86
CO_2 emission reduction potential	Depends on electricity source; zero if renewable	Similar to OWS with additional benefit: avoids hydrazine incineration (which produces NO_x and N_2O, potent greenhouse gases). Electrochemical oxidation produces only N_2 and H_2O	13 and 38
Hydrazine degradation efficiency	Not applicable	>99% removal demonstrated: from 718 ppb to 6 ppb in 120 min; <5 ppb residual after treatment; <10 ppb residual; 100% hydrazine removal in PEM cell	39, 48 and 73

Open Access Article. Published on 12 May 2026. Downloaded on 6/5/2026 6:21:18 AM. This article is licensed under a Creative Commons Attribution 3.0 Unported Licence.

2.4 Integrated hydrazine and HER as cathode and anode

The integration of HzOR at the anode with the HER at the cathode offers a highly efficient and energy-saving strategy for hydrogen production. Unlike conventional water electrolysis, which, as noted, is limited by the sluggish OER and requires high cell voltages (>1.6 V), the substitution of OER with the more thermodynamically favourable HzOR ($E^{\circ} = -0.33$ V *vs.* RHE) substantially reduces the energy input required,[76,77] resulting in markedly improved overall system efficiency. In these integrated systems, hydrazine undergoes a four-electron oxidation process at the anode ($N_2H_4 \rightarrow N_2 + 4H^+ + 4e^-$), while HER proceeds at the cathode through either the Volmer–Heyrovsky or Volmer–Tafel mechanisms, depending on the nature of the electrocatalyst. The synergy between the fast kinetics of HzOR and efficient proton reduction allows hydrogen production at remarkably low cell voltages, often in the range of 0.2–0.3 V.[78] For example, in alkaline media, the Rh nanoparticles doped Ni/N-doped carbon nanofibers (Ni/NCNFs-Rh) demonstrated exceptional outstanding bifunctional performance with HER overpotential as low as 17 mV at 10 mA cm^{-2} and HzOR onset potential of −0.014 V at 10 mA cm^{-2}, enabling hydrazine-assisted water splitting at an ultralow cell voltage of 0.016 V at 10 mA cm^{-2}.[41] In another report, Ni species-incorporated CoP@N-doped carbon nanosheet arrays (Ni–CoP@NC) achieved −143 mV for HER and 51 mV for HzOR to drive a current density of 1 A cm^{-2}, and enabled energy-efficient seawater electrolysis at 0.49 V.[79] The success of such systems depends critically on the rational design and pairing of electrocatalysts that can effectively catalyse both half reactions. Ideal catalysts for HER should possess hydrogen adsorption free energy ($\Delta G_{H^*} \approx 0$ eV), ensuring a balance between hydrogen adsorption and desorption.[80] Meanwhile, efficient HzOR catalysts must exhibit low activation energy for N–H bond cleavage, facilitating rapid dehydrogenation of hydrazine molecules.[13] Beyond these intrinsic properties, high electrical conductivity is essential to minimise internal resistance and promote fast electron transfer between active sites.[81] Furthermore, a high density of active sites, particularly on nanostructured or defect-rich surfaces, enhances catalytic current output. Corrosion and oxidation resistance, especially in acidic or neutral media, ensures long-term stability and durability.[82] Hydrophilicity or optimized surface wettability also improves the interaction between the catalyst and electrolyte, aiding reactant accessibility.[83] Finally, the synergistic interaction between catalytic components (*e.g.*, in heterostructures or alloy systems) can modulate the local electronic structure, leading to enhanced bifunctional performance.

These complementary physicochemical and electronic properties collectively accelerate charge transfer and reaction kinetics at both electrodes, enabling energy-efficient hydrogen production in hydrazine-assisted electrolysers (Table 1).

3 Catalyst activity enhancement mechanisms

Nickel-based catalysts have demonstrated considerable potential for HzOR due to their tunable electronic structure, abundant active sites, and high catalytic stability. A variety of strategies have been developed to enhance further their activity, selectivity, and durability.

3.1 Synergistic and interface engineering

The synergy between different catalyst components often originates from engineered interfaces, where unique electronic interactions and charge redistributions, which enhance catalytic activity by optimising adsorbate binding, accelerating charge transfer, and lowering energy barriers.[90] For example, Mo substitution into Ni_3N nanosheets interfaced with metallic Ni induced an upshift in the Ni d-band centre, optimising hydrazine intermediate binding energies (Fig. 2a). DFT calculations confirmed improved dehydrogenation kinetics, enabling more efficient HzOR.[91] In NiRh-BDC MOF, partial substitution of Ni by Rh created a heteroatomic lattice where Rh sites catalyse HER and Ni sites catalyse HzOR. The strong Rh–Ni electronic coupling at their interface enhanced adsorption of H* and H_2O*, while contraction of Ni–O bonds stabilised the structure. This cooperative interface effect yielded an ultralow operational voltage of 0.06 V at 10 mA cm^{-2} with excellent durability.[30] In NiFe-hydroxide/sulfide heterostructure (NFS@NF), the Fe–Ni interface facilitates charge transfer from Fe to Ni, confirmed by X-ray Photoelectron spectroscopy (XPS) binding energy shifts (Fe 2p positive, Ni 2p negative). This charge redistribution enriched Ni active sites, lowering hydrazine dehydrogenation energy and achieving an overpotential of 0.256 V at 100 mA cm^{-2}.[92]

In CoP nanoparticles integrated with NiCoP nanowires, the heterojunction formed at the CoP/NiCoP interface promotes electron transfer and reduces the energy barrier for a proposed N–N single-bond cleavage pathway in hydrazine oxidation to a remarkably low 0.10 eV, according to DFT calculations performed using the Vienna *Ab Initio* Simulation Package (VASP), employing the generalised gradient approximation with the Perdew–Burke–Ernzerhof (PBE)[25] exchange–correlation functional and the projector Augmented-Wave (PAW) method. This catalyst demonstrated a Tafel slope of 22.9 mV dec^{-1} and low charge transfer resistance, enhancing bifunctional HzOR/HER activity.[84] In $CoFe_2O_4$@nickel nanowires (NNWs) heterojunction, the close contact between $CoFe_2O_4$ and NNWs finely tunes electron density, improving hydrogen adsorption and hydrazine dehydrogenation kinetics. The resulting catalyst showed a Tafel slope of 35.9 mV dec^{-1} and reduced R_{ct} of 3.55 Ω, validated by DFT calculations, which revealed a lower energy barrier of 0.38 eV for the rate-limiting step.[93] In Ni_3N–Co_3N heterointerfaces, hierarchical porous nanosheet arrays with abundant heterointerfaces modulate catalytic sites *via* electronic coupling. This led to a low Tafel slope of 21.6 mV dec^{-1} and high specific activity, with DFT modelling indicating exothermic adsorption (−0.77 eV) of hydrazine on electron-deficient Co sites (Fig. 2b).[44] These studies confirm that designing interfaces between different phases or elements creates synergistic effects through charge redistribution and electronic coupling, significantly improving catalytic kinetics, lowers energy barriers for intermediate steps, and enhances both activity and durability for hydrazine oxidation.

Open Access Article. Published on 12 May 2026. Downloaded on 6/5/2026 6:21:18 AM.
This article is licensed under a Creative Commons Attribution 3.0 Unported Licence.

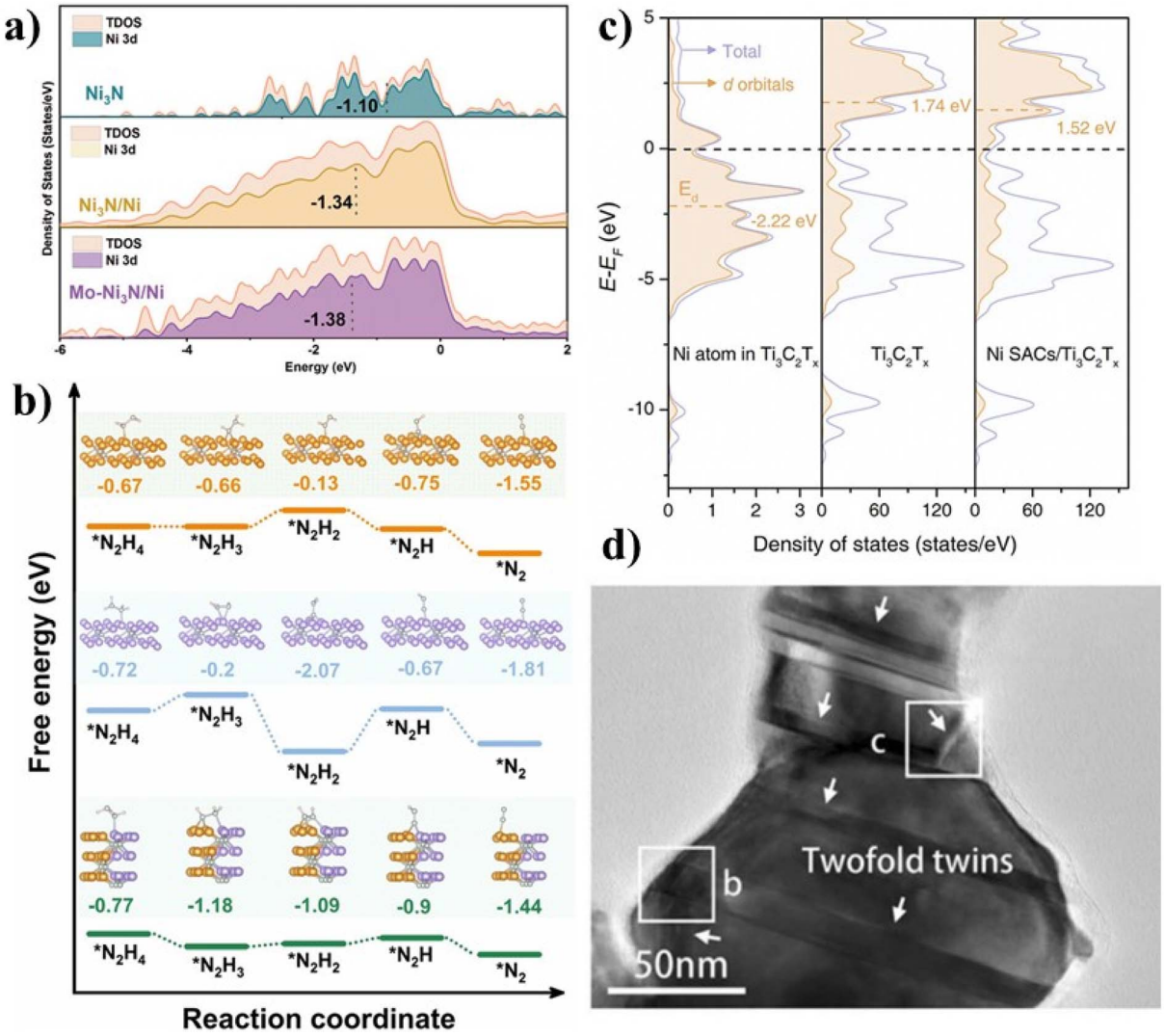

Fig. 2 (a) Comparative density of states (DOS) curves for Mo–Ni_3N/Ni, Ni_3N/Ni, and Ni_3N, Reproduced from ref. 91, with permission from Wiley, *Advanced Functional Materials*, 2021, **31**, 2103673, Copyright 2021. (b) Lowest energy adsorption geometries of all key intermediates and the corresponding free-energy diagrams for HzOR on Ni_3N, Co_3N, and Ni_3N–Co_3N heterostructure surfaces, Reproduced from ref. 44, with permission from Wiley, *Angewandte Chemie*, 2021, **133**, 6049–6058, Copyright 2021. (c) Atom-projected d-band density of states (PDOS) for Ni, together with total DOS, in $Ti_3C_2T_x$, $Ti_3C_2T_x$, and Ni SACs/$Ti_3C_2T_x$, Reproduced from ref. 43, with permission from Wiley, *Advanced Materials*, 2022, **34**, 2204388, Copyright 2022. (d) HRTEM image of twofold nanotwins of Ni–Cu–Zn alloy, Reproduced from ref. 46, with permission from Elsevier, *Journal of Alloys and Compounds*, 2024, **997**, 174898, Copyright 2024.

3.2 Electronic structure modulation and defect engineering

Deliberate tuning of the electronic structure through compositional doping, strain induction, and defect engineering is a key strategy to optimise the catalytic properties of nickel-based catalysts for HzOR. These modifications shift the d-band centre, alter charge density distribution, and stabilise reaction intermediates, thereby lowering activation energy barriers and enhancing reaction kinetics.[94] Qin *et al.* introduced compressive strain in W-doped Ni_3N that shifted the Ni d-band centre upward, optimising intermediate binding. The catalyst demonstrated low overpotential and stable operation for over 450 hours.[50] Cu-doped Ni–Co LDH nanosheets achieved improved hydrazine oxidation due to the presence of Ni^{3+} species formed *via* edge amorphisation and 4.5% Cu doping. This combination enhanced active site density, reduced charge transfer resistance, and enabled a current density of 185.1 mA cm^{-2} at 1.0 V with a Tafel slope of 73.3 mV dec^{-1}.[29] V-doped Ni_3N nanosheets showed lattice distortion and electron redistribution that shifted the Ni d-band centre closer to the Fermi level, enhancing intermediate adsorption and lowering activation barriers for both HzOR and HER.[95] Suryawanshi *et al.* reported Mn-dopant-induced hollow Ni_2P nanocrystals, in which Mn incorporation generated hollow $Ni_{1.4}Mn_{0.6}P$ structures and modulated the electronic structure of Ni_2P, thereby improving hydrazine dehydrogenation kinetics. The optimized catalyst delivered a low HzOR potential of 55 mV at 10 mA cm^{-2} and enabled hydrazine-assisted hydrogen production at only 59 mV in a two-electrode electrolyser.[96]

Open Access Article. Published on 12 May 2026. Downloaded on 6/5/2026 6:21:18 AM. This article is licensed under a Creative Commons Attribution 3.0 Unported Licence.

The density of states (DOS) of Ni_3N, Ni_3N/Ni, and Mo–Ni_3N/Ni were calculated and are shown in Fig. 2a, as obtained from DFT calculations using the Perdew–Burke–Ernzerhof (PBE) functional based on the optimised structures.[97] Upon formation of the hybrid structure, the DOS of Mo–Ni_3N/Ni at the Fermi level is markedly increased. Ni single-atom catalysts (SAC) on $Ti_3C_2T_x$ MXene (Ni SACs) utilised abundant Ti vacancies to induce electronic strain, shifting the d-band centre from 1.74 eV to 1.52 eV (Fig. 2c), which lowered the HzOR energy barrier from 0.583 eV (Ni nanoparticles) to 0.450 eV. This optimised electron transfer and intermediate stabilisation.[43] Oxygen vacancy (V_o)-rich benzene dicarboxylic acid-based MOF ($NiIr_{0.03}$-BDC) demonstrated enhanced OH^- adsorption and *in situ* formation of $Ni(OH)_x$ species during reaction. V_o sites created electron-rich regions that improved hydrazine adsorption, dehydrogenation, charge transfer, hydrophilicity, and mass transport.[42] N-doped activated wood-based carbon-supported Ni catalysts (AWC-Ni–N) showed enhanced surface area and electrical conductivity due to nitrogen heteroatom defects, which also acted as anchoring sites for Ni/NiO. This defect engineering improved hydrazine adsorption and activation, yielding superior electrocatalytic performance.[98]

In Rh-doped NiFe layered double hydroxide (Rh/NiFe LDH), atomically dispersed Rh introduced lattice distortions and defects, shifting d-band centres and optimising hydrazine adsorption, which resulted in an 80 mV lower overpotential compared to undoped NiFe LDH.[99] Fe doping in Ni_2P–Co_2P–Zn_3P_2 heterostructure (Fe–NiCoZnP/NF) shifted the d-band centre toward the Fermi level, enhancing hydrogen and hydrazine reaction kinetics. The catalyst reached 1000 mA cm^{-2} at just 13 mV *vs.* RHE, with a low Tafel slope of 11.9 mV dec^{-1} and excellent stability.[100] Zn-doped, oxygen-deficient $NiCoO_x$ nanoarrays (Zn–$NiCoO_{x-z}$/SSM) exhibited improved conductivity, increased active sites, and optimised electronic structure due to synergistic Zn doping and oxygen vacancies. This catalyst outperformed OER benchmarks, delivering HzOR at −0.116 V *vs.* RHE at 50 mA cm^{-2}.[101] In summary, the combined effects of dopants, vacancies, and strain lead to significant modulation of the electronic properties of nickel-based catalysts. By fine-tuning d-band centres and charge distributions, these strategies facilitate intermediate adsorption, accelerate charge transfer, and improve overall catalytic efficiency and durability for hydrazine oxidation.

3.3 Surface reconfiguration and structural engineering

Surface reconfiguration through vacancy formation, heteroatom incorporation, and amorphous-crystalline phase manipulation has emerged as a vital strategy to enhance HzOR activity. These modifications increase active site density, optimise charge/mass transfer, and stabilise reactive intermediates.[102,103] Mohammadi *et al.* demonstrated that incorporating reduced graphene oxide (rGO) into Ru–Ni/NF significantly improved catalytic activity. The Ru_{11}–Ni_3/rGO/NF catalyst showed an electrochemically active surface area (EASA) of 677.5 cm^2, 1.7 times greater than its rGO-free counterpart. The porous rGO matrix provided abundant defect sites and enhanced electrolyte diffusion, while EIS confirmed a substantial reduction in charge transfer resistance (from 1.4 Ω cm^2 to 0.1 Ω cm^2), leading to higher current density (34 mA cm^{-2} *vs.* 28 mA cm^{-2}).[104] Liu *et al.* developed a partially amorphous a-Ni_2P/Ni/NF catalyst that exhibited ultralow onset potential (0.04 V *vs.* RHE), high electrochemically active surface area (88.5 cm^2), and a Tafel slope of 69 mV dec^{-1}. The crystalline regions ensured high conductivity (sheet resistance ≈2.5 Ω sq^{-1}), while the amorphous domains stabilised intermediates and promoted faster reaction kinetics. This synergy enhanced HzOR activity, selectivity, and long-term durability.[77] These examples affirm that rational surface engineering promotes catalytic efficiency by tuning structural and electronic properties.

3.4 Morphology and phase engineering

Phase and morphology significantly impact HzOR performance by influencing surface area, conductivity, and intermediate interaction. Nanostructuring and crystallographic control enhance accessibility and electron transfer.[36] Vorms *et al.* studied the morphology-dependent activity of metallic nickel, showing that finely divided nanoparticles outperformed bulk nickel. The nanostructured form exhibited a lower Tafel slope (60 mV dec^{-1} *vs.* 80 mV dec^{-1} for bulk Ni), indicating faster kinetics. X-ray diffraction (XRD) revealed dominant Ni(111) and Ni(100) crystal planes, which are known to support more efficient electron transfer and intermediate adsorption, thereby enhancing catalytic activity.[105] Wei *et al.* synthesised a Ni–Zn–Cu alloy catalyst supported on Ni foam, exhibiting superior performance for HzOR. XPS and EDS showed negative shifts in Ni, Cu, and Zn binding energies, indicating strong electronic interactions that promoted electron delocalisation. The combination of Zn and Cu reduced stacking fault energy, facilitating nanotwin formation during annealing (Fig. 2d). Moreover, post-synthesis etching introduced vacancies and dislocations, accelerating electron transport. This catalyst achieved a high current density (170.2 mA cm^{-2} at 0.3 V) and the highest C_{dl} value (20.0 mF cm^{-2}) among tested samples, demonstrating high active site density and favourable reaction kinetics.[46]

Yu *et al.* developed a Ni-doped Co/CoP heterostructure (NiCoP), where nickel incorporation altered the electronic structure by modulating the density of states near the Fermi level. This facilitated favourable adsorption of hydrazine intermediates, enhancing catalytic performance. Electrochemical testing showed that NiCoP achieved nearly 50% higher current density than pristine CoP, along with an excellent faradaic efficiency of 96.4%. The low Tafel slope of 37 mV dec^{-1} reflected improved reaction kinetics and reduced overpotentials, confirming enhanced HzOR activity.[106] These findings show that tailoring nanoscale morphology and phase composition offers robust strategies to enhance catalytic performance.

3.5 Hydrophilicity and wettability enhancement

Improving catalyst hydrophilicity enhances mass transport, gas removal, and catalyst–electrolyte interaction during HzOR. For example, Hao *et al.* demonstrated that a Ni/Ni_3S_4/1T-MoS_2/

Open Access Article. Published on 12 May 2026. Downloaded on 6/5/2026 6:21:18 AM. This article is licensed under a Creative Commons Attribution 3.0 Unported Licence.

carbon cloth catalyst exhibited superior HzOR activity due to its engineered hydrophilic properties. Ni doping into 1T-MoS_2 accelerated charge transfer, while the superhydrophilic 1T-MoS_2 substrate enabled full electrolyte penetration and maximum exposure of active sites. This optimal wetting reduced mass transport barriers, enhanced gas product removal, and contributed to long-term electrochemical stability.[45] Similarly, Feng *et al.* synthesised nanoporous $(Ni, Co)_{0.85}Se$ anchored on reduced graphene oxide (rGO), where oxygen-containing functional groups on rGO significantly enhanced hydrophilicity. This improved wettability allowed better electrolyte access to active sites, facilitated OH^- and N_2H_4 diffusion, and prevented catalyst agglomeration. As a result, the catalyst delivered high current densities (211 mA cm^{-2} at 0.2 V *vs.* RHE) and retained 92.3% performance after 24 hours at 50 mA cm^{-2}, confirming the synergy between wettability and structural design.[107] Wei *et al.* showed that Ni–Zn–Cu/Ni foam achieved a near-zero contact angle (~0°) with the electrolyte compared to bare Ni foam (~123°), confirming significantly enhanced surface wettability. This improved interaction facilitated more efficient charge and mass transfer, leading to enhanced catalytic performance for HzOR.[46] Collectively, these studies underscore that optimising hydrophilicity is a critical design strategy. These studies confirm that wettability optimisation is a powerful design approach for boosting efficiency and long-term stability of Ni-based catalysts in HzOR systems.

3.6 DFT insights and limitations

DFT calculations are widely used to rationalise activity enhancement mechanisms of nickel-based catalysts for hydrazine oxidation, particularly for analysing electronic structure modulation, adsorption energetics of hydrazine-derived intermediates, charge redistribution at heterointerfaces, and reaction energy barriers. Most studies discussed in this section employ periodic slab models with plane-wave basis sets and projector augmented-wave (PAW) pseudopotentials,[108] using the generalised gradient approximation (GGA), typically the PBE functional.[97]

Within this GGA-PBE framework, DFT effectively captures qualitative trends such as d-band centre shifts induced by doping or interface formation, relative adsorption strengths of $N_2H_4^*$ and dehydrogenated intermediates, and comparative activation barriers across different catalyst compositions. These insights have been instrumental in explaining experimentally observed enhancements in HzOR kinetics for heterostructured, defect-rich, and electronically tuned Ni-based catalysts.

For example, DFT calculations on Mo–Ni_3N/Ni showed that Mo incorporation and Ni_3N/Ni interfacial coupling shift the Ni d-band centre and optimise adsorption energetics of hydrazine-derived intermediates, lowering the dehydrogenation barrier and rationalising the experimentally observed ultralow HzOR overpotential.[91] Similarly, Ni_3N–Co_3N heterointerfaces were shown to stabilise key N_2H_4-derived intermediates through interfacial charge redistribution and electron-deficient Co sites, promoting favourable dehydrogenation pathways.[44] In Ni single-atom catalysts supported on $Ti_3C_2T_x$ MXene, DFT revealed that Ti-vacancy-induced electronic perturbation reduces the reaction barrier relative to Ni nanoparticles.[43] Studies on W-doped Ni_3N50 and Mn-doped Ni_2P[96] further showed that strain and dopant-induced d-band shifts can tune adsorption strengths and lower activation barriers, while calculations on Ni–C hybrid nanosheets[43] and Ni–Zn nanotwinned alloys[109] linked surface electronic structure to enhanced hydrazine adsorption and catalytic activity. Together, these studies show that DFT has provided mechanistic insight into descriptor–activity relationships in Ni-based HzOR catalysts.

However, standard GGA-based DFT has well-known limitations for complex electrochemical reactions. It often underestimates reaction barriers, struggles with localised transition-metal d-states, and typically neglects explicit solvent effects, electric double-layer structure, applied electrode potential, and dynamic surface reconstruction. Consequently, calculated adsorption energies and activation barriers should be interpreted primarily in terms of relative trends rather than absolute values. Corrections such as DFT + U,[110] implicit solvation models (*e.g.*, VASPsol[111]), and constant-potential approaches[112] offer improved realism but remain computationally demanding and are not yet routinely applied in HzOR studies.

However, these studies also highlight persistent limitations. Most calculations employ idealised static slab models and neglect explicit solvent structure, electrolyte effects and constant-potential conditions. For example, studies on Mo–Ni_3N/Ni,[91] Ni_3N–Co_3N,[44] and Ni SAC/$Ti_3C_2T_x$ (ref. 43) focus primarily on adsorption energetics and free-energy diagrams, while transition-state treatment of N–H or N–N bond cleavage remains comparatively limited. Likewise, dynamic surface reconstruction into hydroxylated Ni phases, often implicated experimentally during operation, is rarely treated explicitly. Future progress will require more realistic approaches combining constant-potential DFT, explicit solvation, *ab initio* molecular dynamics and Pourbaix stability analysis.

3.7 Summary of activity enhancement strategies

In summary, six complementary strategies have been developed to enhance the HzOR activity of Ni-based electrocatalysts. Synergistic and interface engineering creates charge-redistributed heterointerfaces that lower reaction barriers (*e.g.*, Ni_3N–Co_3N, CoP/NiCoP). Electronic structure modulation and defect engineering tune the d-band center of Ni through doping (Mo, W, V, Mn) or vacancy introduction (P, O), optimizing intermediate adsorption energies. Surface reconfiguration and structural engineering increase active site density *via* amorphization, heteroatom incorporation, or porous architecture design. Morphology and phase engineering exploits nanostructuring (nanosheets, nanorods, nanoflowers) and crystallographic control to maximize surface area and electron transport. Hydrophilicity and wettability enhancement ensures rapid electrolyte penetration and gas bubble release through superhydrophilic/superaerophobic surfaces. Finally, DFT calculations provide mechanistic insights into these enhancement mechanisms, though they face limitations in capturing explicit solvent effects and applied potential. Critically, the most active Ni-based HzOR catalysts reported to date do not rely on a single strategy but rather integrate multiple approaches—

Open Access Article. Published on 12 May 2026. Downloaded on 6/5/2026 6:21:18 AM. This article is licensed under a Creative Commons Attribution 3.0 Unported Licence.

for example, combining heterointerface engineering with defect doping and hierarchical nanostructuring. This multi-strategy synergy appears essential for achieving the record-low overpotentials (<20 mV) and cell voltages (<0.1 V) that make hydrazine-assisted electrolysis commercially attractive.

4 Classification and advances in nickel-based catalysts

4.1 Metallic nickel and its alloys

Various nickel-based alloy catalysts have been strategically developed to advance hydrazine-coupled electrolysis by leveraging synergistic interaction between Ni and other active species.[113] These catalysts consistently demonstrate low overpotentials, high bifunctional activity and exceptional stability, attributes arising from modulated electronic configurations, engineered heterointerfaces, and rationally designed architectures.

The Ni/NCNFs-Rh catalyst, fabricated *via* electrospinning, carbonization, and *in situ* reduction, exhibited excellent bifunctional performance with ultralow overpotentials of 17 mV (HER) and −14 mV (HzOR) at 10 mA cm^{-2}, enabling hydrazine splitting at an ultralow cell voltage of 0.016 V[41] (Fig. 3a). The strong Ni–Rh electronic coupling shifted the d-band center of Rh, optimizing H adsorption ($\Delta G_{H^*} = -0.84$ eV), as supported

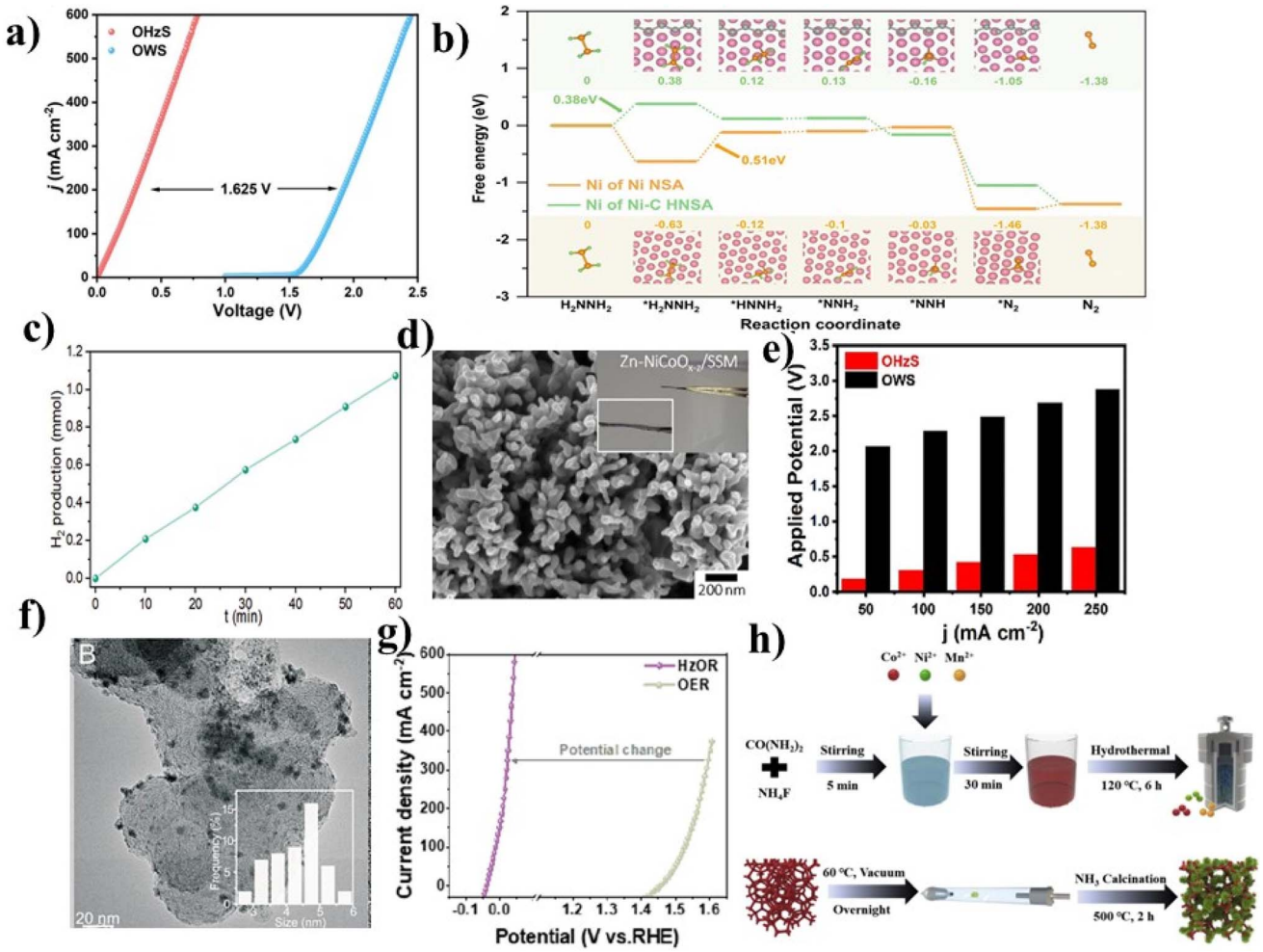

Fig. 3 (a) LSV curves for Ni/NCNFs-Rh in 1.0 M KOH containing 0.5 M N_2H_4 for OHzS and in 1.0 M KOH for OWS, recorded without *iR*-compensation, Reproduced from ref. 41, with permission from Elsevier, *Chemical Engineering Journal*, 2025, **505**, 159561, Copyright 2025. (b) Free energy profiles of HzOR reaction pathways on Ni surfaces of Ni NSA and Ni–C HNSA, along with models of hydrazine and the associated intermediates, Reproduced from ref. 32, with permission from Wiley, *Angewandte Chemie International Edition*, 2022, **61**, e202113082, Copyright 2022. (c) Generation of H_2 and N_2 gas bubbles during catalysis using Ni NCNA, Reproduced from ref. 34, with permission from Wiley, *Small*, 2021, **17**, 2008148, Copyright 2021. (d) SEM image for Zn–$NiCoO_{x-z}$/SSM, Reproduced from ref. 101, with permission from Elsevier, *Journal of Colloid and Interface Science*, 2023, **640**, 737–749, Copyright 2023. (e) Comparison of the required applied potential to reach various current densities for OHzS and OWS by using NiCo/$MoNi_4$ catalyst, Reproduced from ref. 115, with permission from Elsevier, *Chemical Engineering Journal*, 2021, **414**, 128818, Copyright 2021. (f) TEM images of RuNi/C, Reproduced from ref. 116, with permission from Elsevier, *Journal of Colloid and Interface Science*, 2023, **652**, 1848–1856, Copyright 2023. (g) Comparison of LSV curves for HzOR and OER by using Ru-doped MoNi/MoO_2, Reproduced from ref. 117, with permission from Elsevier, *Journal of Colloid and Interface Science*, 2024, **667**, 73–81, Copyright 2024 and (h) the schematic diagram of the synthesis of N–$Ni_1Co_3Mn_{0.4}O$/NF, Reproduced from ref. 118, with permission from Elsevier, *International Journal of Hydrogen energy*, 2022, **47**, 5766–5778, Copyright 2022.

Open Access Article. Published on 12 May 2026. Downloaded on 6/5/2026 6:21:18 AM. This article is licensed under a Creative Commons Attribution 3.0 Unported Licence.

by DFT-derived energy barriers of 1.39 eV (HER) and 0.92 eV (HzOR). The N-doped carbon matrix promoted charge mobility and active site exposure. Similarly, Ni–C hybrid nanosheet arrays (Ni–C HNSA), derived from pyrolysed Ni-MOFs, presented dual-active sites (Ni cores and carbon encapsulation), enabling overpotential of −37 mV (HER) and −20 V mV (HzOR) at 10 mA cm^{-2}. The catalyst achieved hydrazine splitting at 0.14 V (50 mA cm^{-2}), benefiting from optimal ΔG_{H^*} (0.1 eV), a low HzOR barrier (0.38 eV, (Fig. 3b)), and fast kinetics (Tafel slopes: 31.9/16.2 mV dec^{-1}). 100% faradaic efficiency and 50 h stability at 200 mA cm^{-2} were observed.[32]

In another approach, copper-doped nickel cubic nanoporous (Ni(Cu) CNP), prepared *via* pulsed electrodeposition and electrochemical dealloying, showed HER and HzOR overpotentials of 41 mV and −18 mV at 10 mA cm^{-2}, respectively.[33] A 25-fold electrochemical surface area (ECSA) enhancement, combined with Cu doping and NiO/Ni heterojunction, boosted HzOR kinetics (Tafel: 50.2 mV dec^{-1}), enabling a cell voltage of 0.07 V (10 mA cm^{-2}) and stable 24 h operation at 100 mA cm^{-2}. Moreover, Ni–Co(OH)F@$NiCo_2S_4$ core–shell nanorods, synthesised *via* hydrothermal sulfidation, incorporated metallic Ni^0/Ni^{2+} species and conductive interfaces. Overpotentials of 97 mV (HER) and −49 mV (HzOR) at 10 mA cm^{-2}, enabled hydrazine splitting at 250 mV, with improved charge transfer and H adsorption.[27] Similarly, Ni–CoP@NC nanosheets, obtained by electrodeposition and phosphorization, integrated Ni-doped CoP cores with N-doped carbon shells, delivering overpotentials of −143 mV (HER) and 51 mV (HzOR) at 1 A cm^{-2}.[79] Enhanced hydrogen adsorption (−0.08 eV) and low HzOR barriers (0.45 eV) resulted from Ni^0 and N-carbon synergy, enabling seawater electrolysis at 0.49 V.

A further example is the hierarchical Ni NCNA (nanorod-confined nanoflake arrays), constructed *via* hydrothermal-annealing routes, achieved −26 mV (HzOR) and 47 mV (HER) at 10 mA cm^{-2}. Integrated into a seawater electrolyser, the system achieved 1.074 mmol h^{-1} H_2 generation at just 0.485 V (892 mA cm^{-2}), assisted by Ni/NiCo interfaces, MoO_{3-x} conductivity enhancement and superhydrophilic 3D bubble repelling architecture[34] (Fig. 3c). In addition, a Ni(Cu)@NiFeP catalyst, synthesised *via* two-step electrodeposition, exhibited 33 mV (HER) 6 mV (HzOR) at 10 mA cm^{-2}.[114] A triple-hierarchy porous framework enhanced active site exposure, while electronic coupling and dynamic surface hydroxide layers promoted charge transport, enabling 0.491 V at 10 10 mA cm^{-2} hydrazine splitting with 1000 cycles stability. Furthermore, Zn-doped oxygen-deficient $NiCoO_{x-z}$ nanoarrays on stainless steel mesh, hydrothermally synthesised and reduced (Fig. 3d), delivered −0.116 V (HzOR, 50 mA cm^{-2}) with a low Tafel slope of 25 mV dec^{-1}. Zn incorporation and oxygen vacancies enhanced conductivity and durability, lowering overall electrolysis voltage to 0.700 V. The catalyst maintained 82.45% activity after 100 hours.[101] NiCo/$MoNi_4$ heterostructure on Ni foam, derived from hydrothermal synthesis and thermal reduction, showed −30 mV for HzOR and 68 mV for HER at 10 mA cm^{-2}.[115] Moreover, the catalyst delivered 250 mA cm^{-2} at 0.63 V (Fig. 3e).

Likewise, Co-reduced RuNi nanoalloys (~4.1 nm) showed strong Ru–Ni interactions that facilitated water dissociation (E_w = 0.38 eV) and HzOR (barrier = 0.29 eV)[116] (Fig. 3f). Overpotentials of 24 mV (HER) and −65 mV (HzOR) were achieved at 10 mA cm^{-2}, with a mesoporous carbon matrix supporting rapid kinetics and long-term stability. Another highly efficient system, a Ru-doped MoNi/MoO_2 catalyst, with a porous, superhydrophilic 1D structure, exhibited excellent HER and HzOR performance, requiring low overpotentials of 13 mV and −34 mV at 10 mA cm^{-2}, respectively. Ru doping modulated the electronic structure, while Ni–Mo synergy and oxygen vacancies enhanced charge transfer and reaction kinetics. For overall hydrazine splitting, it required only 0.57 V at 50 mA cm^{-2}, demonstrating high efficiency and outstanding stability[117] (Fig. 3g). Furthermore, N–$Ni_1Co_3Mn_{0.4}O$/NF catalyst, comprising interconnected nanosheets, demonstrated −177 mV (HER), −70 mV (HzOR) and 0.272 V (overall) at 100 mA cm^{-2}. Activity enhancements stemmed from multimetallic synergy, CoO heterostructures, and Mn/N-induced electronic modulation[118] (Fig. 3h). In another example, Ni–Zn intermetallic nanosheets, produced by mild etching and ethylene glycol (EG) reduction, featured *meso*-porosity and strong interfacial interaction, attaining 214.3 mA cm^{-2} at 0.1 V. The system retained 87.8% performance after 24 h and enabled hydrazine splitting at 0.8 V (100 mA cm^{-2}).[119]

Surface hydroxylation formed Ni/$Co(OH)_2$, enhancing adsorption while preserving intrinsic active phases. $CoFe_2O_4$@NNWs, formed by growing $CoFe_2O_4$ on nickel nanowires, exhibited excellent bifunctional activity towards HER/HzOR, as summarised in Table 2.[93] The corresponding hydrazine-assisted electrolyser delivered an ultralow operating voltage and demonstrated remarkable durability, retaining >95% current after 3000 cyclic voltametry (CV) cycles and 50 h continuous operation. Furthermore, DFT calculations revealed that nitrogen-doped nanowires (NNWs), defect-rich nanosheets, and interfacial electron redistribution synergistically enhance charge transfer and lower kinetic barriers. In a significant advance, 1.48 nm NiCoMoPtRu high-entropy alloy nanoclusters were synthesised as a solid solution phase.[120] They delivered HER (9.5 mV at 10 mA cm^{-2}) and HzOR (3.26 A mg^{-1}) activities, enabling overall hydrazine splitting at an unprecedently low cell voltage with 150 hours stability (Fig. 4a). High-Angle Annular Dark-Field Scanning Transmission Electron Microscopy (HAADF-STEM), X-ray Absorption Fine Structure (XAFS), and X-ray Absorption Near Edge Structure (XANES) revealed intermetallic electron redistribution that fine-tuned hydrogen adsorption, while the ultrasmall size, and conductive support fully activated the surface and set a new benchmark for efficient hydrogen production.

A hierarchical Co/MoNi heterostructure was hydrothermally grown on oxygen vacancy-rich $CoNiMoO_x$ nanorods and calcined in H_2/Ar.[121] It delivered ultralow −82 mV (HER) and −23 mV (HzOR) overpotentials at 100 mA cm^{-2}. DFT calculations showed the interface accelerates water dissociation, H* adsorption, and N_2H_4 dehydrogenation. In a hybrid electrolyser, the cell required only 0.059 V, cutting energy use by 90%, while enabling hydrazine detoxification and 40 h stability. $MoNi_4$/MoO_2 hollow nanorods were grown on Ni foam *via* hydrothermal-anneal-reduction; the Kirkendall effect generated

Open Access Article. Published on 12 May 2026. Downloaded on 6/5/2026 6:21:18 AM.
This article is licensed under a Creative Commons Attribution 3.0 Unported Licence.

Table 2 Comparative analysis of Ni-based electrocatalyst for HzOR, HER and OHzS

Catalyst types	Catalyst name	Electrolyte KOH/N_2H_4 (M)	HzOR (V *vs.* RHE at 10 mA cm^{-2})	HER (V *vs.* RHE at 10 mA cm^{-2})	Cell voltage (V) at 10 mA cm^{-2}	Stability (h)	Ref. electrode	Faradic efficiency (%)	Major catalytic site	Ref
Metallic Ni and its alloys	Ni/NCNFs-Rh	1/0.5	−0.014	0.017	0.016	40	Hg/HgO	100	Metallic Ni	41
	Ni-HEANCs	1/0.1	−0.020	0.037	0.14@50	30	Hg/HgO	100	All the metals are active	32
	Ni(Cu) CNP	1/0.5	−0.018	0.041	0.07	24	SCE	99.2	Catalytic site is not a single elementsynergistic interface of Cu-doped metallic Ni	33
	Ni–Co(OH)F@$NiCo_2S_4$	1/1.5	−0.049	0.097	0.25	24	Hg/HgO	99.4	Ni–Co(OH)F@$NiCo_2S_4$ heterointerface	27
	Ni–CoP@NC	1/0.2	0.051@1000	0.143@1000	0.49@1000	47	Hg/HgO	—	Ni-modified CoP surface	79
	Ni NCNA	1/0.3	−0.026	0.047	0.023	1	Hg/HgO	—	Metallic Ni	34
	Ni(Cu)@NiFeP	1/0.5	0.006	0.033	0.491@100	12	SCE	100	Ni^0/Cu^0	114
	Zn–$NiCoO_{x-z}$	1/0.6	−0.116@50	—	0.7@50	100	Hg/HgO	—	Oxygen-deficient Ni/Co	101
	RuNi/C	4/1	−0.065	0.024	0.0578	10	Ag/AgCl/KCl	—	Ni metall and Ru electron promotor	116
	Ru–MoNi/MoO_2	1/0.5	−0.034	0.013	0.57@50	16	Ag/AgCl	—	Ni active site and MoO_2 behave conductive support	117
	N–$Ni_1Co_3Mn_{0.4}O$/NF	1/0.5	0.177	0.272@100	0.272@100	20	Hg/HgO	—	Co/CoO heterointerface	118
	Ni–Zn/NF	1 NaOH/0.5	0.1@214.3	—	0.8@100	24	Hg/HgO	—	Ni nanosheets	119
	NiCo/$MoNi_4$/NF	1/0.1	−0.030	0.068	0.63@250	10	Hg/HgO	100	NiCo alloy nanoparticles	115
	$CoFe_2O_4$@NNWs	1/0.5	−0.091	0.045	0.028	120	Hg/HgO	100	Co sites in $CoFe_2O_4$ nanosheets are the primary active centers	93
	NiCoMoPtRu/C	1/0.1	—	0.0095	0.025	150	SCE	—	Multiple metal-atom ensembles (especially hollow sites) on surface	120
	CoNiMo/CoNiMoO_x	1 NaOH/0.5	−0.023@100	0.082@100	0.059	40	Hg/HgO	—	CoNiMo and CoNiMoO_x behave as support	121
	$MoNi_4/MoO_2$/NF	1/0.5	0.47@1000	0.056@100	0.54@1000	100	SCE	100	Ni as primary active center, modulated by Mo	122
	Ni_4Mo/Ni_4W/NF	1/2 NaCl/0.1	−0.067	0.007	0.034	23	A/AgCl	—	Ni sites in Ni_4Mo and Ni_4W nanoalloys	123
	NiCo@C/MXene/CF	1/0.5	−0.025@100	0.049	0.31@500	140	Ag/AgCl	—	NiCo alloy	49

Open Access Article. Published on 12 May 2026. Downloaded on 6/5/2026 6:21:18 AM.
This article is licensed under a Creative Commons Attribution 3.0 Unported Licence.

Table 2 (*Contd.*)

Catalyst types	Catalyst name	Electrolyte KOH/N_2H_4 (M)	HzOR (V *vs.* RHE at 10 mA cm^{-2})	HER (V *vs.* RHE at 10 mA cm^{-2})	Cell voltage (V) at 10 mA cm^{-2}	Stability (h)	Ref. electrode	Faradic efficiency (%)	Major catalytic site	Ref
	CoFeNiCrMnP/NF	1/0.4	0.268@100	0.051@100	0.091@100	20	SCE	98	Cr metal	124
	CoSe–$Ni_{0.95}Se$/MXene/NF	1/0.1	0.1161@400	0.1608@400	0.35@100	7 days	SCE	100	Ni metal	125
	$Ru_{0.91}Ni_{0.09}$-N/O–Ti_3C_2	1/0.5	−0.0299	0.0293	0.02	35	—	97.6	Ni metal	86
	NiCoPt-10/CC	1/0.5	0.068	0.090	0.295	25	Hg/HgO	97	Co atoms	126
	Ni(Cu)/NF	1/0.5	0.038@50	0.203@50	0.41@100	10	SCE	100	Ni^0 sites	21
	NT-Ni–Zn/NF	1 NaOH/0.5	0.04@212	—	0.07	15	Hg/HgO	—	Ni atoms (Ni^0) on the twinned Ni–Zn surface	109
	Ni–Zn/NF	1 NaOH/0.1	0.7@970	0.068	0.497@100	10	SCE	—	Specifically the $Ni^{\delta-}$ sites at the coherent Ni–NiZn interface	127
Oxides and hydroxides	CoPB@NiFe–OH/NF	1/1	−0.135	0.032	0@25	12	Hg/HgO	Close to 100	Ni sites (in NiFe–OH) serve as	128
	Fe/P–$NiMoO_4$/NF	1/0.5	0.09@100	0.023	0.13	24	SCE	100	$NiMoO_4$ nanorods	129
	NiO/Ru/CFC	1/0.5	−0.079	0.0293	0.021	180	Hg/HgO	99	Ru atoms	130
	a-RuMo/$NiMoO_4$/NF	1/0.5	−0.091	0.013	0.007	100	Hg/HgO	100	Amorphous RuMo	131
	NiOOH@CoCu CH	1/0.5	−0.031	0.171	0.087	12	Hg/HgO	—	NiOOH	132
	Ni/β-$Ni(OH)_2$/NF	1/0.3	−0.015	0.058	0.16	60	Hg/HgO	~98.5	Ni/b-$Ni(OH)_2$ NSAs	51
	N_C-FeNi$(OH)_2$/NF	1/0.1	0.99@100	—	1.20@100	60	Ag/AgCl	—	$Ni(OH)_2$	133
	NFS-2@NF	1/0.3	0.19@100	0.150	0.37	70	Ag/AgCl	—	Ni and Fe	92
	CuO_x@$Ni_{1-\gamma}Co_\gamma O$/CF	1/0.5	0.0047	0.0469	0.095	12	Ag/AgCl	—	$Ni_{1-y}Co_yO$	134
Nitrides	Mo–Ni_3N/Ni/NF	1/0.1	−0.003	0.045	0.055	10	Hg/HgO	100	Ni major site along with Ni_3N	91
	Cu_1Ni_2–N/CFC	1/0.5	0.005	0.0714	0.24	75	Hg/HgO	95	Cu1Ni_2–N	135
	Ni-SN@C	1/0.1	0.0168	0.023	0.336	24	Ag/AgCl	100	Nickel surface nitride	136
	W–Ni_3N	1/1	0.081@100	0.046	0.185@50	450	Hg/HgO	—	Ni_3N	50
	Ni_3N–Co_3N/NF	1/0.2	−0.088	0.043	0.071	20	Hg/HgO	100	Ni_3N	44
	Ce–Ni_3N/NF	1/0.5	0.256	0.092	0.156	100	Ag/AgCl	—	Ni_3N	137
	V–Ni_3N/NF	1/0.1	0.002	0.070	0.094	10	Hg/HgO	—	Ni_3N	95
Phosphides	Ni–P/rGO/NF	1/0.1	0.00734	0.117	0.241@100	50	Ag/AgCl	—	Ni–P	138
	Ni–Cu–P@Ni–Cu/NF	1/0.5	0.00388	0.070	0.125	50	Ag/AgCl	—	Ni–Cu–P/NiCu behave as conductive support	139
	$(Co_{0.6}Ni_{0.4})_2P$@PC	1/0.5	−0.083	0.0679	0.048	13	Ag/AgCl	—	$(Co_{0.6}Ni_{0.4})_2P$	140
	NiSeP@NiCo/Cu	1/0.5	0.041	0.040	0.071	150	Ag/AgCl	—	Ni/Co metal sites	141
	$Ni_{1.4}Mn_{0.6}P$/NF	1/0.5	0.055	0.192@50	0.059	60	Ag/AgCl	98	Ni atoms in Mn-doped Ni_2P	96
	N–Ni_5P_4@CoP/CFP	1/0.1	−0.032	0.055	0.037	100	SCE	—	N–Ni_5P_4	142
	Ni–Co–Fe–P/NF	1/0.5	0.025	0.064	0.094	100	Ag/AgCl	—	Ni, Co, and Fe atoms on the surface	143
	Ni–Co/CoP	1/0.4	−0.070	0.053	0.040	50	Ag/AgCl	96.4	Co atoms	106

Open Access Article. Published on 12 May 2026. Downloaded on 6/5/2026 6:21:18 AM.
This article is licensed under a Creative Commons Attribution 3.0 Unported Licence.

Table 2 (*Contd.*)

Catalyst types	Catalyst name	Electrolyte KOH/N_2H_4 (M)	HzOR (V *vs.* RHE at 10 mA cm^{-2})	HER (V *vs.* RHE at 10 mA cm^{-2})	Cell voltage (V) at 10 mA cm^{-2}	Stability (h)	Ref. electrode	Faradic efficiency (%)	Major catalytic site	Ref
	Fe–CoNiP@NC	1/0.5	0.49@1000	0.28@1000	0.56@1000	100	Hg/HgO	100	CoNiP	47
	$Ni(OH)_2/Ni_2P$/NF	1/0.5	−0.014	0.072	0.357@100	24	Ag/AgCl	—	Electrophilic Ni atoms (for HzOR)	144
	Al–Ni_2P/NF	1/0.5	0.300@500	0.205@500	0.717@500	24	Ag/AgCl	96	Ni_2P while Al change the electronic properties	145
	$(Ni_{0.6}Co_{0.4})_2P$/GC	1 mol L^{-1}/0.1 mol L^{-1}	0.463@50	—	0.228	—	Hg/HgO	99	Ni	146
	Ru, Fe–Ni_2P/NF	1/0.5	0.26@1000	0.054	0.69	24	SCE	100	Fe–Ni_2P	89
	Mo–Ni_2P_4@MNF	1/0.5	0.126@1000	0.259@3000	0.571@1000	1000	SCE	100	Ni_2P_4	39
	RuC–NiCoP	1/0.2	−0.089@100	0.010	1.77@300	80	Hg/HgO	—	Ni atoms in the Ru,Fe-doped Ni_2P, where Ru and Fe serve as electronic modulators	85
	Cu_1Co_2–Ni_2P/NF	1/0.1	−0.052	0.051	0.16	20	Hg/HgO	—	Ni_2P	154
	NiMo/Ni_2P	1/0.5	−0.017	0.015	0.343@500	20	SCE	—	Ni_2P	147
	Ru_1–NiCoP	1/0.3	−0.060	0.032	0.090@50	30	Hg/HgO	—	NiCoP–Ru behave as electrone promotor	148
	NiFeP/NF	1/0.5	28.05 mV dec^{-1} (Tafel slope)	0.148	0.1	40	Ag/AgCl	—	NiFeP	149
	Fe–NiCoZnP/NF	1/0.5	0.013@1000	0.121@1000	0.33@100	120	Hg/HgO	—	Fe–NiCoZnP	100
	Fe–Ni_2P/CeO_2	1/0.5	−0.117	0.067	0.051	10	SCE	—	Fe–Ni_2P	57
	(P–Co/Ni_3P)A_3/NF	1/0.4	−0.079	0.010	0.05@300	20	Ag/AgCl	—	P-modified Co (P–Co)	150
	Cysteine-capped Ni_2P	1/0.1	—	0.18	0.46	12	Ag/AgCl	—	Ni_2P	152
	CoP/Ni_2P/NF	1/0.5	−0.0751	0.2161@300	0.108	48	Hg/HgO	98.6	CoP	153
	Ni–Co–P/NF	1/0.1	−0.061	0.037	0.498@500	100	Ag/AgCl	97	Ni–Co–P	84
	Ni_2P/Co_2P/NF	1/0.5	0.230	0.070	0.107@100	96	Hg/HgO	100	Co_2P	151
Sulfides	Ni/Ni_3S_4/1T-MoS_2/CC	1/0.3	0	0.024	0.017	100	Hg/HgO	100	Ni atoms (metallic Ni and Ni in Ni_3S_4)	45
	Co–FeNiSOH/NFF	1/0.4	0.355@100	0.266@100	0.26	10	SCE	96	Co centers	155
	NiCoMoS@$Ni(CN)_2$	1/0.1	0.025@100	0.175@100	0.36@200	10	Hg/HgO	100	Ni	156
	Ru–VO_x/Ni_3S_2	1/0.5	−0.066	0.007	0.015	100	Hg/HgO	100	Vanadium(v) atom in the amorphous VO_x layer	157
	NiMoPSO	1/0.5	−0.059	0.041	0.039	70	Ag/AgCl	—	Mo atoms	158
	P–$NiCo_2S_4$	1/0.5	0.19	0.12	0.24	10	Ag/AgCl	—	Ni	159
Selenides	ZIF67@CoNiSe-3	1/0.1	0.13@400	0.049	0.45@100	30	—	—	Co and Ni atoms on	160
	$MoSe_2$@NiSe/NF	1/0.5	0.064@100	0.105	0.5@100	50	Hg/HgO	—	Ni atoms Se proton acceptor	161
	NiSe-2/NF	1/0.1	0.4@318	—	0.356	12	SCE	100	NiSe-2	28
	$NiSe_2$/CuSe/NF	1/0.25	—	0.0877	0.268	48	SCE	—	$NiSe_2$	162
	NiSe/NF	1/0.5	0.35@100	0.095	0.310	30	SCE	97.8	NiSe	163

Open Access Article. Published on 12 May 2026. Downloaded on 6/5/2026 6:21:18 AM.
This article is licensed under a Creative Commons Attribution 3.0 Unported Licence.

Table 2 (*Contd.*)

Catalyst types	Catalyst name	Electrolyte KOH/N_2H_4 (M)	HzOR (V *vs.* RHE at 10 mA cm^{-2})	HER (V *vs.* RHE at 10 mA cm^{-2})	Cell voltage (V) at 10 mA cm^{-2}	Stability (h)	Ref. electrode	Faradic efficiency (%)	Major catalytic site	Ref
	P/Fe–$NiSe_2$/NF	1/0.7	0.20	0.074	0.31	100	Hg/HgO	100	$NiSe_2$	164
	Ru–NiSe	1/0.5	0.70@100	—	0.78@50	4 days	Ag/AgCl	—	NiSe and Ru behave as the electron modifier	165
Oxalate	Ru–(Ni/Fe)C_2O_4/NF	1/0.1	−0.096	0.042	0.01	50	Hg/HgO	100	Fe (and Ni) atoms on high-index facets of (Ni/Fe)C_2O_4	166
	$SNiC_2O_4$–Nb_2O_5/NF	1/0.5	—	0.155@20	0.33@20	95	Hg/HgO	100	Ni atoms in $SniC_2O_4$	167
Phosphate	Pd/PdO-NiPh	1/0.5	0.506	0.298	0.538	12	Hg/HgO	—	Ni^{2+} (in NiPh)	168
MOFs	Pt@NiFe-MOF	1/0.5	0.357@1500	0.071@100	0.667@2000	190	Ag/AgCl	100	Pt nanoparticles	48
	MIL-(trNiFe)@NF	1/0.5	0.220@500	0.069@100	0.69@1000	24	SCE	100	Ni and Fe atoms	170
	FeCo–Ni_2P@MIL-FeCoNi	1 mol L^{-1}/0.1 mol L^{-1}	0.042@1000	0.310@1000	0.4@1000	1000	Hg/HgO	100	FeCo–Ni_2P	171
	NiRh-BDC	1/0.3	0.017	0.049	0.06	60	Hg/HgO	100	Ni nodes	30
LDHs	Ru/NiCo LDH	1/0.1	−0.118	0.019	0.223@100	42	SCE	—	Ru atoms	172
	Ru_a/NiFe-LDH	1/0.3	0.075	0.026	0.1@1000	100	Hg/HgO	—	Ru atoms	169

41% hollow cavities.[122] The architecture delivered 56 mV HER at 100 mA cm^{-2} and 470 mV HzOR at 1 A cm^{-2}. In a hybrid seawater cell, it required only 0.54 V at 1 A cm^{-2}, saving 2.94 Wh L^{-1} H_2 *vs.* conventional systems while maintaining >100 h stability and ≈100% faradaic efficiency. The performance is attributed to $MoNi_4/MoO_2$ synergy that optimised H* adsorption, oxygen spillover and interfacial charge redistribution. Similarly, Ni_4Mo/Ni_4W (~20–50 nm) nanoparticles anchored on MoO_2/WO_3 cuboids were hydrothermally grown on Ni foam.[123] The catalyst demonstrated excellent bifunctional activity towards HzOR and HER, as summarised in Table 2, enabling efficient hydrazine-assisted seawater electrolysis with a markedly reduced cell voltage compared to conventional systems. DFT calculations attributed to Ni–Mo/W coupling that lowered water-dissociation and $*N_2H_3$ dehydrogenation barriers, while a chloride-resistant MoO_2/WO_3 support maintained >20 h stability at 400 mA cm^{-2}. NiCo@C/MXene/CF was fabricated by MXene wrapping copper foam, NiCo-MOF growth, and NH_3 anneal. The 3D scaffold (400–800 nm nanosheets, 54 m^2 g^{-1}) with 10–20 nm NiCo alloy in carbon delivered 43 mV HzOR and 49 mV HER at 500 mA cm^{-2}.[49] MXene conductivity and superaerophobic/hydrophilic surfaces enabled a 0.7 V seawater electrolyser at 500 mA cm^{-2}, 2.75 kWh m^{-3} H_2, chlorine-free operation, and <3 ppb hydrazine removal.

Electrodeposited CoFeNiCrMnP/NF formed 50 nm porous nanosheets (ECSA = 73 mF cm^{-2}).[124] High entropy synergy, P-doping and super-aerophobic morphology delivered 51 mV HER, 268 mV HzOR at 100 mA cm^{-2}, enabling full-cell hydrazine electrolysis with 98% H_2/N_2 faradaic efficiency over 20 h (Fig. 4b and c). In another strategy, electrodeposited CoSe–$Ni_{0.95}$Se/MXene on Ni foam exhibited 0.269/0.318 nm heterointerfaces and Mxene-driven charge redistribution.[125] The catalyst exhibited excellent bifunctional activity toward HER and HzOR, as summarised in Table 2, along with high faradaic efficiency and long-term operational stability. DFT modelling ascribed the performance to MXene-enhanced electron transfer that lowered ΔG_{H^*} to −0.08 eV and HzOR barrier to 0.16 eV. A hollow N/O–Ti_3C_2 was templated with melamine formaldehyde, then decorated at 350 °C in H_2/Ar with 2.1 nm $Ru_{0.91}Ni_{0.09}$ clusters.[86] The architecture and Ni → Ru charge transfer shifted the d-band centre, enabling 29 mV HER and −30 mV HzOR at 10 mA cm^{-2}. Hydrazine splitting required 0.02 V at 10 mA cm^{-2} and 0.92 V at 1 A cm^{-2} (Fig. 4d), cutting energy to 0.35 kWh m^{-3} H_2, 93% lower than OWS at 150 mA cm^{-2}.

Using pulsed laser irradiation, $NiCoO_x$ + K_2PtCl_4 in ethanol yielded surfactant-free NiCoPt microparticles (14.6 wt% Pt) that catalysed HER at 90 mV and HzOR at 68 mV (10 mA cm^{-2}).[126] A symmetric NiCoPt-10‖NiCoPt-10 cell split hydrazine at 0.295 V (1.4 V lower than water splitting). DFT modelling revealed that Pt lowered ΔG_{H^*} to −0.12 eV and dehydrogenation barriers, while *in situ* Raman confirmed favourable $*OH/*N_2H_4$ adsorption. Coupled to a Zn-hydrazine battery, the system reached 97% energy efficiency for self-powered H_2 production and waste remediation. Electrodeposited Ni(Cu) on Ni foam was dealloyed to create 3D hollow Ni nanotubes (200 nm diameter, 250 nm wall, BET 28.7 m^2 g^{-1}, 18× ECSA boost).[21] A 2 nm NiO shell on a Ni-rich core, with 3 at% Cu, shifted the Ni 3d band

Open Access Article. Published on 12 May 2026. Downloaded on 6/5/2026 6:21:18 AM.
This article is licensed under a Creative Commons Attribution 3.0 Unported Licence.

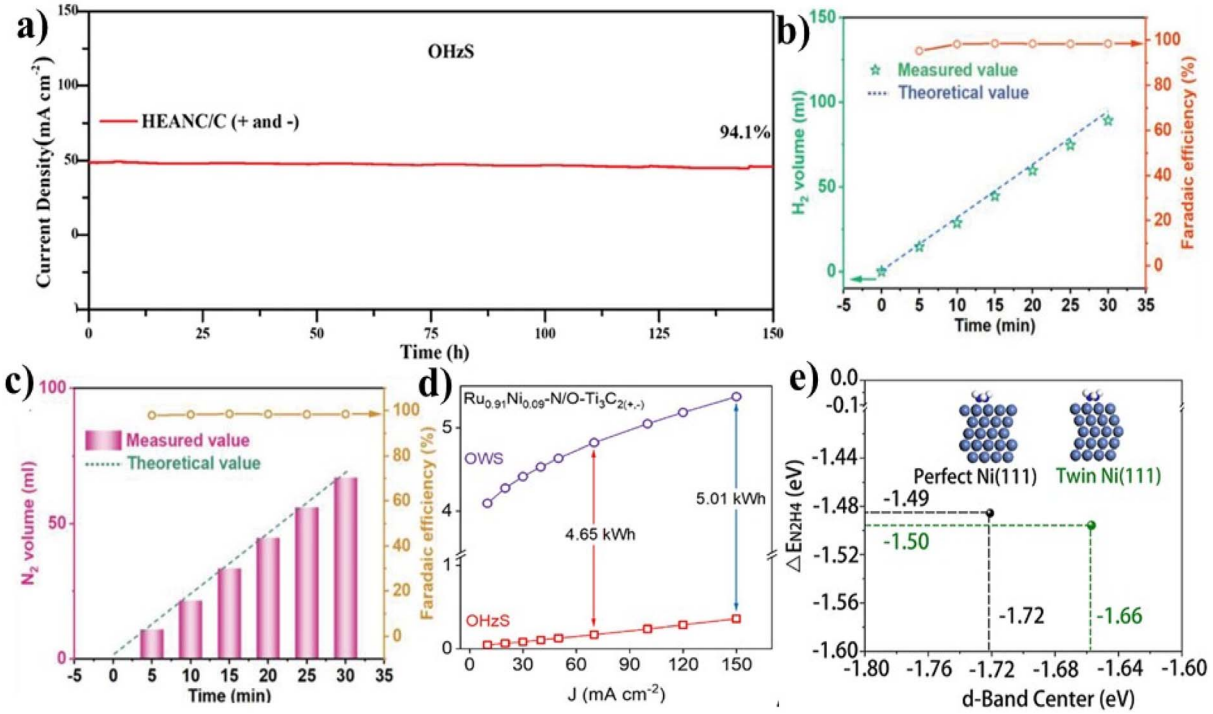

Fig. 4 (a) Long-term electrochemical stability of HEANC/C evaluated under constant potential for 150 h, Reproduced from ref. 120, with permission from Wiley, *Advanced Materials*, 2024, **36**, 2309715, Copyright 2024. (b and c) Faradaic efficiencies and gas evolution profiles for HER and HzOR using CoFeNiCrMnP/NF catalyst, Reproduced from ref. 124, with permission from Wiley, Li *et al.*, *Small*, 2023, **19**, 2302130, Copyright 2023. (d) Electricity cost comparison between OWS and OHzS at different current densities using $Ru_{0.91}Ni_{0.09}$–N/O–Ti_3C_2, Reproduced from ref. 86, with permission from Wiley, *Small*, 2025, **21**, 2502553, Copyright 2025. (e) Calculated hydrazine adsorption energies and d-band centers for twin Ni(111) surfaces, Reproduced from ref. 109, with permission from ACS, *ACS Applied Energy Materials*, 2024, **7**, 5202–5208, Copyright 2024.

down by 0.18 eV, weakening *OH adsorption and lowering the HzOR barrier to 0.41 eV. Curvature focused on the local field (1.8×) and speed bubble release (contact angle 147°), lowering R_{ct} to 1.2 Ω. The electrode delivered 50 mA cm^{-2} HzOR at 38 mV and 100 mA cm^{-2} HER at 203 mV, sustaining 100 mA cm^{-2} at 0.41 V with <15 mV drifting over 10 h.

Likewise, in co-deposited Ni–Zn hydroxide nanosheets on Ni foam mesopores were created by alkaline etch, then H_2 reduced/annealed to yield NT-Ni–Zn, porous nanosheets threaded with ~7 nm spaced nanotwins stabilised by Zn.[109] Twin-boundary strain (±10%) upshifted the Ni d-band centre (−1.61 eV), Fig. 4e, boosting N_2H_4 adsorption (−1.65 eV) and dehydrogenation kinetics. The catalyst delivered 212 mA cm^{-2} HzOR at 0.04 V *vs.* RHE (Tafel 55 mV dec^{-1}) and powered an OHzS cell at 70 mV for 10 mA cm^{-2}, saving ~90% energy *versus* water splitting with 94% activity retained after 15 h. In another example, *via* H_2-bubble-template electrodeposition (800 mA cm^{-2}, 343 K, 90 s) from Ni/Zn/pyrophosphate baths, porous Ni–Zn nanosheets (0.174 nm (200), 0.124 nm (220) planes) were grown on NF.[127] The resulting material exhibited a hierarchical three-dimensional porous network with well-defined crystalline planes and a super-aerophobic surface, leading to a large electrochemically accessible surface area and facilitated gas release during operation. As summarised in Table 2, these structural advantages enabled efficient bifunctional activity toward HER and HzOR with substantially reduced cell voltage compared to conventional water splitting, while maintaining high operational stability over prolonged electrolysis.

To summarise, the NiCoMoPtRu high-entropy alloy (HEA) nanoclusters (1.48 nm), synthesised as a solid-solution phase, exhibited outstanding hydrazine-coupled electrolysis performance. With ultralow HER overpotential (9.5 mV) and high HzOR activity (3.26 A mg^{-1}), they enabled full-cell operation at unprecedentedly low voltages for 150 h. Intermetallic electron redistribution, ultrasmall size, and a conductive matrix synergistically optimised hydrogen adsorption and surface activation, setting a new benchmark in catalytic efficiency.

4.2 Nickel oxides and hydroxides

Nickel-based oxides and hydroxides have emerged as highly effective materials for hydrazine-assisted hydrogen production due to their tunable electronic structures, abundant active sites, and strong compatibility with transition metal dopants. These materials can be engineered to optimise adsorption energies, accelerate charge transfer, and improve gas release, which together boost HER/HzOR activity and overall water-splitting efficiency.

NiFe–OH nanosheets were hydrothermally grown on Ni foam and subsequently coated with cobalt phosphoborate (CoPB) *via* electrodeposition at controlled P/B ratios.[128] The resulting CoPB@NiFe–OH/NF exhibited 32 mV for HER and −135 mV for HzOR at 10 mA cm^{-2}. Hydrazine-assisted electrolysis proceeded

Open Access Article. Published on 12 May 2026. Downloaded on 6/5/2026 6:21:18 AM.
This article is licensed under a Creative Commons Attribution 3.0 Unported Licence.

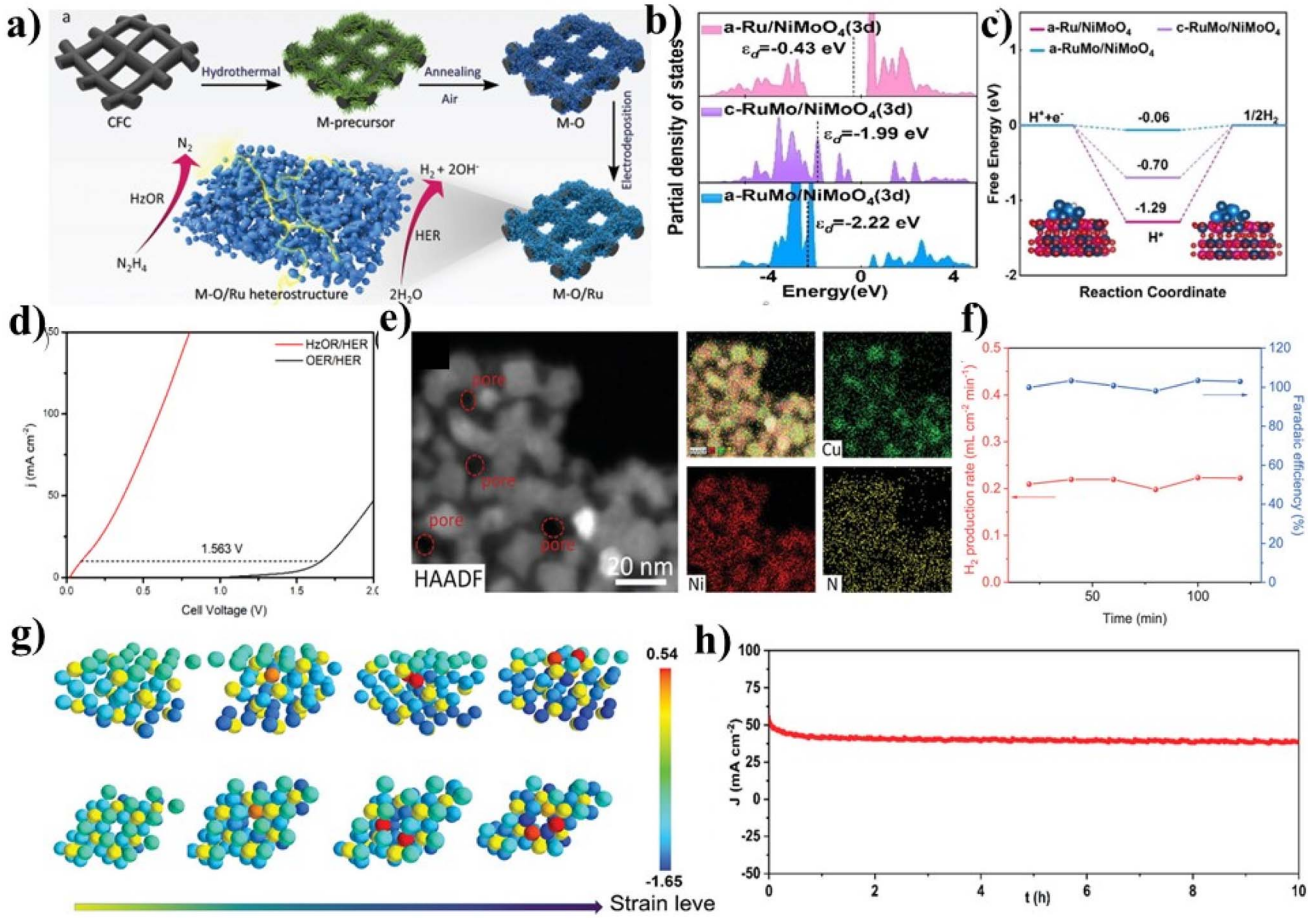

Fig. 5 (a) Schematic representation of the synthesis route for M–O/Ru heterostructured electrocatalyst, Reproduced from ref. 130, with permission from Wiley, *Advanced Functional Materials*, 2025, **35**, 2415058, Copyright 2025. (b) PDOS and corresponding d-band center values for three constructed hybrid electrocatalysts: a-Ru/$NiMoO_4$, c-RuMo/NiMoO4, a-RuMo/$NiMoO_4$, (c) Gibbs free energy diagram for HER pathway for the above catalysts, Reproduced from ref. 131, with permission from Wiley, *Angewandte Chemie International Edition*, 2025, **64**, e202414234, Copyright 2025. (d) LSV curves of the CuO_x@$Ni_{1-\gamma}Co_\gamma O$/CF electrode at a scan rate of 5 mV s^{-1}, comparing performance in pure water electrolysis and hydrazine-assisted systems, Reproduced from ref. 134, with permission from ACS, *ACS Applied Energy Materials*, 2024, **7**, 6248–6257, Copyright 2024. (e) HAADF-STEM image and corresponding elemental distribution maps of the Cu_1Ni_2–N/CFC catalyst, Reproduced from ref. 135, with permission from Wiley, *Advanced Energy Materials*, 2019, **9**, 1900390, Copyright 2019. (f) Hydrogen generation rate and faradaic efficiency for hydrazine-assisted seawater electrolysis using Ni-SN@C, Reproduced from ref. 136, with permission from Wiley, *Advanced Energy Materials*, 2021, **33**, 2007508, Copyright 2021. (g) Atomic-scale ε_d values for Ni_3N, and W-doped (W_1, W_2-, and W_3–Ni_3N) with the N 2p band center set as reference (0 eV), Reproduced from ref. 50, with permission from Wiley, *Advanced Materials*, 2025, **37**, 2417593, Copyright 2025. (h) Chronoamperometric (*I*–*t*) stability profile of V–Ni_3N NS//V–Ni_3N NS measured over 10 h in 1 M KOH and 0.1 M KOH electrolytes, Reproduced from ref. 95 with permission from ACS, *ACS Applied Materials & Interfaces*, 2021, **13**, 3881–3890, Copyright 2021.

at 0 V (25 mA cm^{-2}, 0.48 kWh m^{-3} H_2) with 60 h durability. Electron transfer from CoPB to NiFe–OH shifts the d-band centre, optimising adsorption behaviour. Hydrophilic and gas-repellent surface properties improved bubble release and interface stability.

Similarly, Fe/P-doped $NiMoO_4$ hollow nanorods (8.97 m^2 g^{-1}) required 0.13 V and 0.45 V to reach 10 and 100 mA cm^{-2}, respectively, for seawater-compatible HzOR.[129] Co-doping adjusted the electronic structure and decreased the work function (6.585 eV), facilitating intermediate adsorption. Membrane-electrode assembly (MEA) integration resulted in 2.3 kWh m^{-3} energy input and full chlorine suppression. In another work, NiO/Ru nanoneedles, synthesised by hydrothermal growth, annealing, and Ru electrodeposition, delivered 29.3 mV (HER) and −79 mV (HzOR) (Fig. 5a).[130] Hydrazine-assisted electrolysis required only 0.021 V. Ru incorporation induced a p–n transition and enhanced interfacial conductivity. Lattice strain and oxygen vacancies promoted charge transport. DFT modelling revealed low energy barriers for both reactions.

Likewise, amorphous RuMo/$NiMoO_4$ heterostructures prepared by heteroatom implantation showed excellent bifunctional activity toward HER and HzOR, as summarised in Table 2,[131] together with outstanding long-term operational stability and near-unity faradaic efficiency. Electronic structure analysis revealed a downshifted d-band centre (−2.22 eV), ΔG_{H^*} (−0.06 eV), and a reduced reaction energy barrier (0.47 eV) supported fast kinetics and balanced intermediate binding (Fig. 5b and c). Another effective design, NiOOH@CoCu CH, was fabricated by sequential hydrothermal growth of CoCu CH nanorods and electrodeposition of NiOOH nanosheets.[132] The

Open Access Article. Published on 12 May 2026. Downloaded on 6/5/2026 6:21:18 AM. This article is licensed under a Creative Commons Attribution 3.0 Unported Licence.

aligned nanorods, wrapped with NiOOH, yielded 1.49 V for OER, −171 mV for HER, and −31 mV for HzOR at 10 mA cm^{-2}. In a hydrazine-fed electrolyser, the cell required only 0.087 V to reach 10 mA cm^{-2}, 1.47 V lower than standard water splitting and operated steadily for 12 h. The performance was enabled by strong interface coupling, effective charge/gas diffusion, and abundant active sites.

In another study, Ni/β-$Ni(OH)_2$ nanosheet arrays (NSAs) were developed *via* hydrothermal synthesis and H_2 plasma reduction, integrating metallic Ni nanoparticles to enhance alkaline HER and HzOR performance.[51] DFT calculations revealed that β-$Ni(OH)_2$ had a favourable hydrogen adsorption energy (0.09 eV). The catalyst achieved a low overpotential of 58 mV for HER and 0.16 V for hydrazine coupled electrolysis, exhibiting superior activity, charge transfer, and long-term stability compared to Ni/α-$Ni(OH)_2$ and Pt/C. Moreover, molten-salt-derived $FeNi(OH)_2$ nanosheets on Ni foam incorporated monodentate nitrate at Ni sites.[133] The catalyst oxidised hydrazine at 1.01 V in seawater (100 mA cm^{-2}), 340 mV below the OER. It sustained 100 mA cm^{-2} at 1.20 V for 60 h. Ni^{4+} stabilisation by nitrate and Fe-facilitated electron transfer contributed to high activity. Tafel slope (40 mV/dec), low R_{ct} (0.90 Ω), and high C_{dl} (5.33 mF cm^{-2}) supported fast kinetics and dense active site utilisation (~7.55 × 10^{18} cm^{-2}).

In another example, NiFe hydroxide/sulfide nanosheets (NFS-2@NF), synthesised *via* a one-pot chemical bath, showed 150 mV for HER and 0.19 V for HzOR at 10 mA cm^{-2}.[92] Full-cell operation required 0.37 V, while Mg/seawater batteries delivered 4.02 mW cm^{-2} with 70 h stability. Ni–Fe coupling, sulfur-induced band modulation, and the porous scaffold ensured efficient transport and hydrazine decomposition.

Leng *et al.* designed a hierarchical CuO_x@$Ni_{1-\gamma}Co_\gamma O$/CF catalyst *via in situ* etching, solvothermal deposition, and thermal treatment.[134] The structure consisted of hollow CuOx nanotubes coated with $Ni_{1-\gamma}Co_\gamma O$ nanosheets. The electrode delivered 46.9 mV (HER) and 4.7 mV (HzOR) at 10 mA cm^{-2}. In a symmetric electrolyser, it required 95 mV to operate, outperforming standard OER/HER systems (Fig. 5d). The Cu/Ni/Co combination tailored electronic structure, and binder-free configuration supported efficient charge transfer and 12 h durability.

4.3 Nickel nitrides

Nickel-based nitrides have emerged as highly efficient electrocatalysts for hydrazine-assisted hydrogen production due to their intrinsic metallic conductivity, tunable electronic structures, and robust chemical stability under alkaline conditions. Nitrogen incorporation and transition metal doping enable optimised hydrogen adsorption energetics and enhanced charge transfer, resulting in superior bifunctional activity. Liu *et al.* reported a Mo-doped Ni_3N/Ni heterostructure (Mo–Ni_3N/Ni/NF) synthesised *via* hydrothermal treatment followed by nitridation, which formed porous nanosheets with abundant interfaces.[91] This catalyst exhibited outstanding bifunctional activity, requiring only −0.3 mV for HzOR and 45 mV for HER at 10 mA cm^{-2}, achieving overall hydrazine splitting at 55 mV, outperforming conventional electrolysis. Mo doping optimised H* adsorption (0.06 eV), while Ni_3N/Ni interfaces enhanced charge transfer. The porous, superhydrophilic architecture supported mass transport and durability.

Similarly, Cu_1Ni_2–N nanosheets synthesised through solvothermal growth of Cu_1Ni_2-LDH and subsequent 125 showed strong interfacial coupling between Cu_4N and Ni_3N (Fig. 5e), porous structure (61.83 m^2 g^{-1}) and high conductivity (8.1 × 10^3 S m^{-1}), enabling ultralow potential of 0.5 mV for HzOR and stable bifunctional activity over 75 h.[135] Ni-SN@C catalyst featuring unsaturated surface Ni–N bonds and synthesised by calcining Ni-EDTA complex under NH_3, exhibited remarkable HER and HzOR activity in alkaline seawater with low overpotentials of 23 and 16.8 mV, respectively.[136] Pt-like hydronium generation enabled 100% faradaic efficiency and a high hydrogen production rate of 0.21 mL cm^{-2} min^{-1} (Fig. 5f). In a flow cell, the catalyst achieved 1 A cm^{-2} at 0.7 V, attributed to the synergistic effects of surface Ni–N sites, corrosion-resistant carbon, and charge redistribution.

W-doped Ni_3N nanoribbons with uniform W incorporation and compressed lattice were synthesised *via* controlled doping.[50] The compressive strain (especially at grain boundaries) downshifted the d-band centre, weakening H* and N–H adsorption to optimise hydrogen binding and lower the hydrazine dehydrogenation barrier (Fig. 5g). The catalyst required 46 mV (HER) and 81 mV (HzOR) at 10 and 100 mA cm^{-2}, respectively. In hydrazine electrolysis, it ran stably at 0.185 V for 450 h, cutting energy use by a factor of 4.2 compared with water splitting.

Hierarchical porous Ni_3N–Co_3N nanosheet arrays were grown on Ni foam, creating abundant Ni_3N/Co_3N heterointerfaces that redistributed electrons, lowered hydrogen and hydrazine adsorption energies, and accelerated charge transfer.[44] The porous nanosheet architecture facilitates electrolyte penetration and efficient gas release, while the conductive Ni foam substrate ensures rapid electron transport. As summarised in Table 2, these synergistic structural and electronic features enable highly efficient bifunctional HER and HzOR activity with excellent durability under hydrazine-assisted water-splitting conditions. Ce-doped Ni_3N nanosheets on Ni foam created a porous 3D architecture.[137] Ce lowered the d-band centre, optimising H* binding and boosting HER/HzOR kinetics. The electrode needed 92 mV (HER) and 0.256 V (HzOR) at 10 mA cm^{-2}, and only 0.156 V in hydrazine splitting. It remained stable for 100 h at 400 mA cm^{-2}.

V-doped Ni_3N nanosheets were synthesised through hydrothermal-nitridation, forming a porous structure with abundant active sites.[95] V incorporation modulated the electronic structure by lowering the d-band centre and optimising hydrogen adsorption energy, which enhanced HER (70 mV) and HzOR (2 mV) at 10 mA cm^{-2} in alkaline media. In a hydrazine splitting system, the catalyst achieved a low cell voltage of 0.094 V and sustained performance for over 10 hours (Fig. 5h). The hierarchical nanosheet morphology facilitated mass and charge transport, while the nickel foam substrate ensured mechanical stability. To summarise, the Mo-doped Ni_3N/Ni heterostructure (Mo–Ni_3N/Ni/NF) stands out as the best nickel

 This journal is © The Royal Society of Chemistry 2026

Open Access Article. Published on 12 May 2026. Downloaded on 6/5/2026 6:21:18 AM.
This article is licensed under a Creative Commons Attribution 3.0 Unported Licence.

nitride catalyst for hydrazine-assisted hydrogen production. It achieved ultralow overpotentials of −0.3 mV (HzOR) and 45 mV (HER) at 10 mA cm^{-2}, with a remarkably low full-cell voltage of 55 mV. Mo doping optimised H* adsorption (0.06 eV), while Ni_3N/Ni interfaces enhanced charge transfer. Its porous, superhydrophilic structure enabled excellent mass transport, bifunctional activity, and long-term stability, outperforming conventional water electrolysis.

4.4 Nickel phosphides

Nickel phosphides have emerged as outstanding bifunctional electrocatalysts for hydrazine-assisted hydrogen production. Their tunable electronic structure, diverse phases, and synergy with dopants delivered high conductivity, abundant active sites, and optimal adsorption energies for both HER and HzOR. Through heterostructuring, vacancy engineering, and doping, they surpassed noble-metal benchmarks, offering low overpotentials, long-term stability, and scalable synthesis.

A Ni–P/rGO/NF electrode was fabricated by pulse-reverse electrodeposition of rGO on Ni foam, followed by cyclic voltammetric deposition of amorphous Ni–P.[138] The nano-micro porous architecture provided abundant active sites, strong adhesion, and high conductivity. The electrode required −117 mV (HER) and 7.34 mV (HzOR) at 10 mA cm^{-2}, and −82 mV (HER) and 127 mV (HzOR) at 100 mA cm^{-2}. It retained 94.3% (HER) and 96.7% (HzOR) activity after 50 h of operation and delivered 241 mV at 100 mA cm^{-2} in

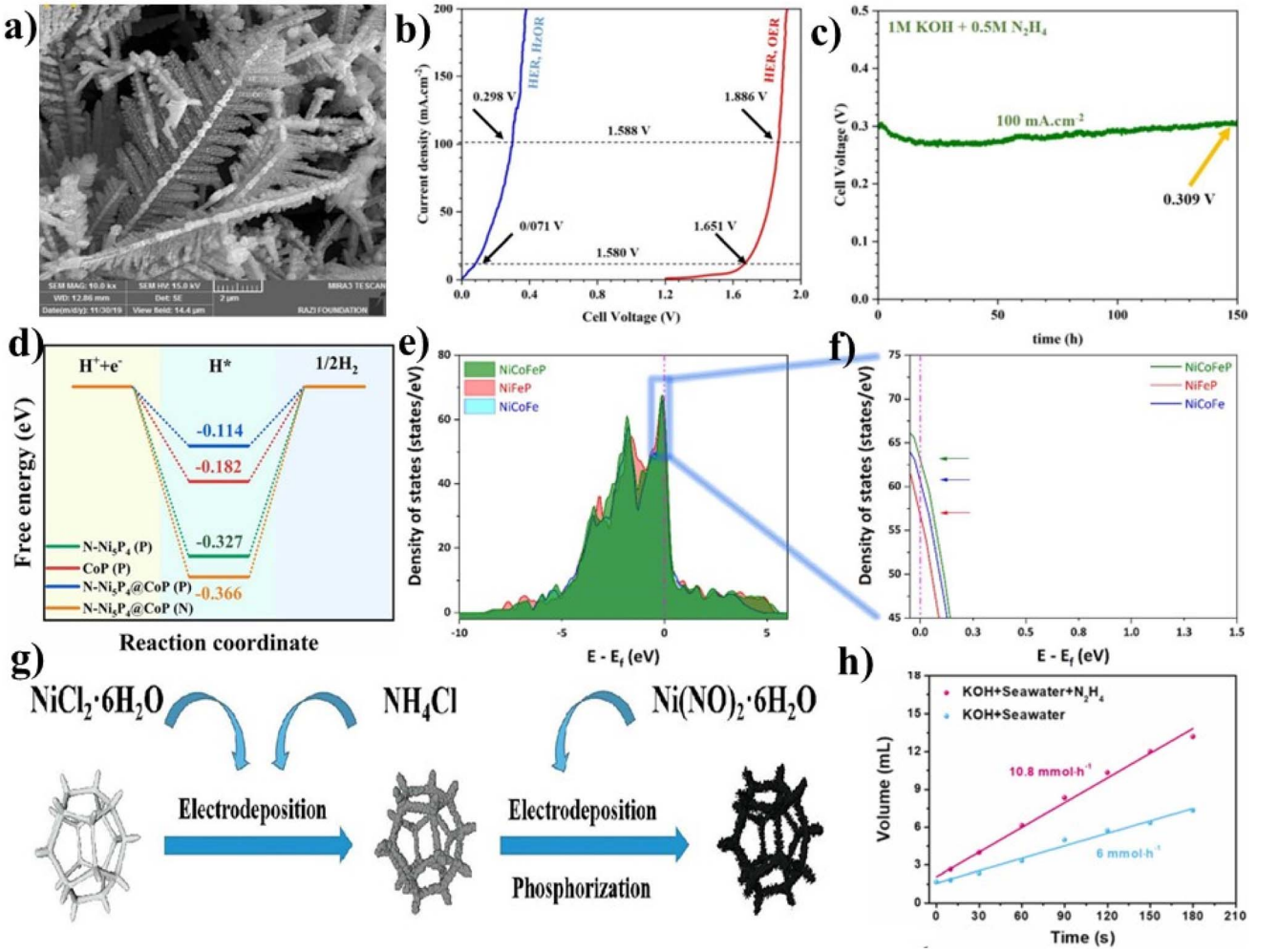

Fig. 6 (a) FESEM images of Ni–Cu–P@Ni–Cu catalyst synthesized after 10 electrodeposition cycles, Reproduced from ref. 139, with permission from Elsevier, *Electrochimica Acta*, 2021, **382**, 138335, Copyright 2021. (b) Cell voltage comparison for overall water splitting (HER + OER) and hydrazine assisted water splitting (HER + HzOR) using LSV curves of NiSeP@NiCo/Cu at a scan rate of 1 mV s^{-1}, (c) chronopotentiometric stability test at 100 mA cm^{-2} over 150 h for NiSeP@NiCo/Cu electrode in HER/HzOR configuration, Reproduced from ref. 141, with permission from Elsevier, *Journal of Colloid and Interface Science*, 2025, **678**, 828–841, Copyright 2025. (d) Gibbs free energy diagram (ΔG_{H^*}), and (g) corresponding P–H* bond lengths for the CoP, N–Ni_5P_4, and N–Ni_5P_4/CoP systems, Reproduced from ref. 142, with permission from Elsevier, *Applied Catalysis B: Environmental*, 2023, **324**, 122207, Copyright 2023. (e and f) Total DOS for Ni–Co–Fe–P, Ni–Fe–P, and Ni–Co–P alloys and a magnified view for detailed comparison, Reproduced from ref. 143, with permission from Elsevier, *International Journal of Hydrogen Energy*, 2023, **48**, 4253–4263, Copyright 2023. (g) Schematic illustration of the synthesis process of $Ni(OH)_2$/Ni_2P on NF, Reproduced from ref. 144, with permission from Elsevier, *Chemical Engineering Journal*, 2023, **475**, 146134, Copyright 2023. (h) Hydrogen generation rate of a self-powered system operating in 1.0 M KOH + seawater and 1.0 M KOH + seawater + 0.5 M N_2H_4 using RuFe–Ni_2P@NF as the catalyst, Reproduced from ref. 89, with permission from Elsevier, *Nano Energy*, 2023, **105**, 108008, Copyright 2023.

Open Access Article. Published on 12 May 2026. Downloaded on 6/5/2026 6:21:18 AM. This article is licensed under a Creative Commons Attribution 3.0 Unported Licence.

a two-electrode hydrazine-splitting cell, demonstrating efficient, durable hydrogen production. Similarly, a two-step electrodeposited Ni–Cu–P@Ni–Cu nano-micro dendrite catalyst (Fig. 6a) with a crystalline core–amorphous shell structure delivered −70 mV HER and 3.88 mV HzOR overpotentials at 10 mA cm^{-2} and drove overall hydrazine splitting at only 125 mV.[139] Synergistic Ni–Cu–P chemistry, superhydrophilic/aerophobic dendrites, and a binder-free self-support conferred 50 h durability, offering a noble-metal-free, highly efficient hydrogen production route.

A one-step pyrolysis of a 1-hydroxyethylidene-1,1-diphosphonic acid-based precursor (CoNi-HEDP) yielded $(Co_{0.6}Ni_{0.4})_2P$ nanoparticles embedded in P-doped carbon ($(Co_{0.6}Ni_{0.4})_2P$@PC).[140] The material delivered 67.9 mV overpotential for HER and −83 mV for HzOR at 10 mA cm^{-2} in alkaline media, leveraging Co/Ni synergy, P-doped carbon conductivity, and *in situ* surface hydroxides. In a hydrazine-assisted water-splitting device, it needed only 0.048 V to reach 10 mA cm^{-2}, far below the 1.60 V required for conventional electrolysis. Moreover, a two-step electrodeposited NiSeP@NiCo/Cu catalyst with 3D nano-microcones and superhydrophilic nanosheets delivered −40 mV for HER and 0.041 V for HzOR at 10 mA cm^{-2}, enabled by Ni–Co–Se–P synergy, 544 cm^2 ECSA, and fast bubble release.[141] A HER/HzOR cell needed only 0.071 V at 10 mA cm^{-2} *versus* 1.886 V for conventional HER/OER, while retaining >96% activity after 150 h and operating under solar power, underscoring its industrial hydrogen-production potential (Fig. 6b and c).

In another example, a colloidal heat-up method with the Kirkendall effect produced hollow Mn-doped Ni_2P nanocrystals ($Ni_{1.4}Mn_{0.6}P$). The catalyst delivered 55 mV for HzOR at 10 mA cm^{-2} and 192 mV for HER at 50 mA cm^{-2} in alkaline media.[96] DFT modelling showed Mn doping lowered ΔG_{H^*} and the hydrazine dehydrogenation barrier, accelerating kinetics. In a two-electrode cell, it required only 59 mV at 10 mA cm^{-2}, and coupled with a Si PV, it reached 14.6% solar-to-hydrogen efficiency. The hollow structure and Mn-induced electronic tuning enhanced site exposure and charge transfer, offering a low-cost noble-metal alternative for sustainable H_2 production. Hydrothermal-phosphorisation yielded N–Ni_5P_4@CoP/carbon fibre paper (CFP) nanowire arrays whose CoP/N–Ni_5P_4 heterointerface, tuned by N-doping, delivered HER overpotentials of 55–59 mV across pH and −32 mV for HzOR at 10 mA cm^{-2}.[142] Nitrogen doping tuned the Ni_5P_4 electronic structure and boosted interfacial charge transfer. DFT calculations showed that P sites in N–Ni_5P_4 ($\Delta G_{H^*} = -0.114$ eV) promoted HER (Fig. 6d), while Co sites accelerated hydrazine dehydrogenation *via* an N-strengthened interfacial field. An overall hydrazine-splitting electrolyser ran at 0.037 V (10 mA cm^{-2}), and solar-cell and lemon-battery tests validated its energy-saving hydrogen production.

A two-step electrodeposition produced self-supported Ni–Co–Fe–P nanosheets. The 3D hierarchical structure, amorphous Ni–Co–Fe–P on vertical Ni nanosheets, offered abundant active sites and high conductivity.[143] The catalyst required 64 mV for HER and 25 mV for HzOR at 10 mA cm^{-2} in alkaline media. In a hydrazine-assisted water-splitting cell, only 94 mV was needed at 10 mA cm^{-2}, far below conventional OER systems. DFT modelling indicated that Ni–Co–Fe–P synergy shifted the d-band centre to −1.43 eV and improved Fermi-level charge transfer, tuning intermediate adsorption (Fig. 6e and f). The binder-free electrode retained performance over 100 h. A low-energy cyclic voltammetry method delivered a Ni-doped Co/CoP amorphous/crystalline hetero-phase. Ni incorporation strained the lattice and tuned the electronic structure.[106] As summarised in Table 2, the catalyst exhibited excellent bifunctional activity toward HER and HzOR. DFT calculations attributed the enhanced performance to a dual-site catalytic mechanism, wherein electron-deficient Co centres facilitate hydrazine activation *via* N–N bond cleavage, while adjacent electron-rich P sites stabilise hydrogen intermediates, thereby enabling highly efficient hydrazine-coupled electrolysis with substantially reduced energy consumption compared to conventional electrolysis.

Likewise, Ni_2P/CoP heterostructures embedded in N-doped carbon nanosheets (Fe–CoNiP@NC).[47] The hierarchical nanosheets delivered 1000 mA cm^{-2} at 0.49 V for HzOR and −0.28 V for HER in alkaline seawater, and a two-electrode OHzS cell required only 0.56 V while remaining stable for 100 h. DFT modelling showed that Fe doping and the carbon shell lowered the d-band centre and accelerated charge transfer, saving 4.03 kWh m^{-3} of H_2 compared with conventional seawater electrolysis while simultaneously degrading hydrazine wastewater.

Moreover, a three-step electrodeposition–phosphorisation–electrodeposition sequence on nickel foam produced hierarchical $Ni(OH)_2/Ni_2P$ microspheres coated with ultrathin amorphous $Ni(OH)_2$ nanosheets (Fig. 6g).[144] The catalyst delivered 72 mV for HER and −14 mV for HzOR at 10 mA cm^{-2} in alkaline media. In a two-electrode cell, it required only 0.357 V at 100 mA cm^{-2} and 0.513 V at 200 mA cm^{-2} for hydrazine-coupled electrolysis, surpassing conventional electrolysis. XPS and kinetic studies traced enhanced performance to interfacial electron transfer that lowered charge-transfer resistance and reduced the HER activation energy to 30.7 kJ mol^{-1}.

A hydrothermal-phosphorisation route produced Al-doped Ni_2P nanoflowers (Al–Ni_2P/NF) with ultrathin nanosheets and phosphorus vacancies.[145] The catalyst delivered −205 mV for HER and 300 mV for HzOR at 500 mA cm^{-2} in alkaline media. In a two-electrode cell, it required only 0.717 V to reach 500 mA cm^{-2}, cutting the energy cost to \$0.68 kg^{-1} H_2. Al doping redistributed electrons, generating electrophilic Ni (HzOR) and nucleophilic P (HER) sites, while P vacancies lowered the activation energy to 34.1 kJ mol^{-1}. In another example, cobalt-doped nickel phosphide ($(Ni_{0.6}Co_{0.4})_2P$) synthesised by hydrothermal-phosphidation delivered an HzOR onset potential of −45 mV and reached 50 mA cm^{-2} at 113 mV, surpassing pure Ni_2P and Co_2P.[146] The Ni/Co synergy created dual active sites: Ni promoted N_2H_4 adsorption and initial dehydrogenation, while Co accelerated later steps and eased nitrogen release. DFT calculations confirmed that Co doping lowered the free energy of the rate-determining step and improved charge redistribution, accelerating kinetics. The catalyst exhibited excellent stability, achieved 263.0 mW cm^{-2} in direct hydrazine fuel cells, and enabled efficient hydrogen generation *via* hydrazine-coupled electrolysis.

 This journal is © The Royal Society of Chemistry 2026

Open Access Article. Published on 12 May 2026. Downloaded on 6/5/2026 6:21:18 AM.
This article is licensed under a Creative Commons Attribution 3.0 Unported Licence.

Likewise, Ru, Fe-doped Ni_2P nanosheets were grown on Ni foam *via* hydrothermal-phosphidation. The catalyst required 54 mV (10 mA cm^{-2}) and 262 mV (1000 mA cm^{-2}) for seawater HER, and 0.26 V for HzOR at 1000 mA cm^{-2}.[89] A two-electrode cell operated at 0.69 V, saving 4.70 Wh L^{-1} H_2. A self-powered device produced 10.8 mmol H_2 h^{-1} (Fig. 6h), outperforming 6.0 mmol h^{-1} for alkaline seawater electrolysis. Ru tuned H adsorption (−0.13 eV), and Fe lowered the $*N_2H_3 \rightarrow *N_2H_2$ barrier. The catalyst also reduced hydrazine wastewater to 8 ppb.

Hydrothermal growth and phosphidation produced Mo-doped Ni_2P nanosheets with phosphorus vacancies (Mo–Ni_2P_4@MNF). The catalyst required 259 mV for seawater HER at 3000 mA cm^{-2} and 126 mV for HzOR at 1000 mA cm^{-2}.[39] In a two-electrode cell, overall hydrazine splitting operated at 571 mV (1000 mA cm^{-2}) and remained stable for 1000 h at 100 mA cm^{-2} (Fig. 7a). Mo doping delivered near-thermoneutral hydrogen adsorption (−0.171 eV) for HER, while P vacancies cut the HzOR $*N_2H_4 \rightarrow *NHNH_2$ barrier from 1.11 eV to 0.40 eV. A self-powered module delivered 37.06 mW cm^{-2} and reduced hydrazine wastewater to <5 ppb. Ru-cluster-decorated NiCoP (RuC–NiCoP) surpassed its single-atom analogue (RuSA-NiCoP) for both HER and HzOR.[85] A direct hydrazine fuel cell with the RuC–NiCoP anode recorded a peak power density of 226 mW cm^{-2} (Fig. 7b). The catalyst required only 10 mV for HER and

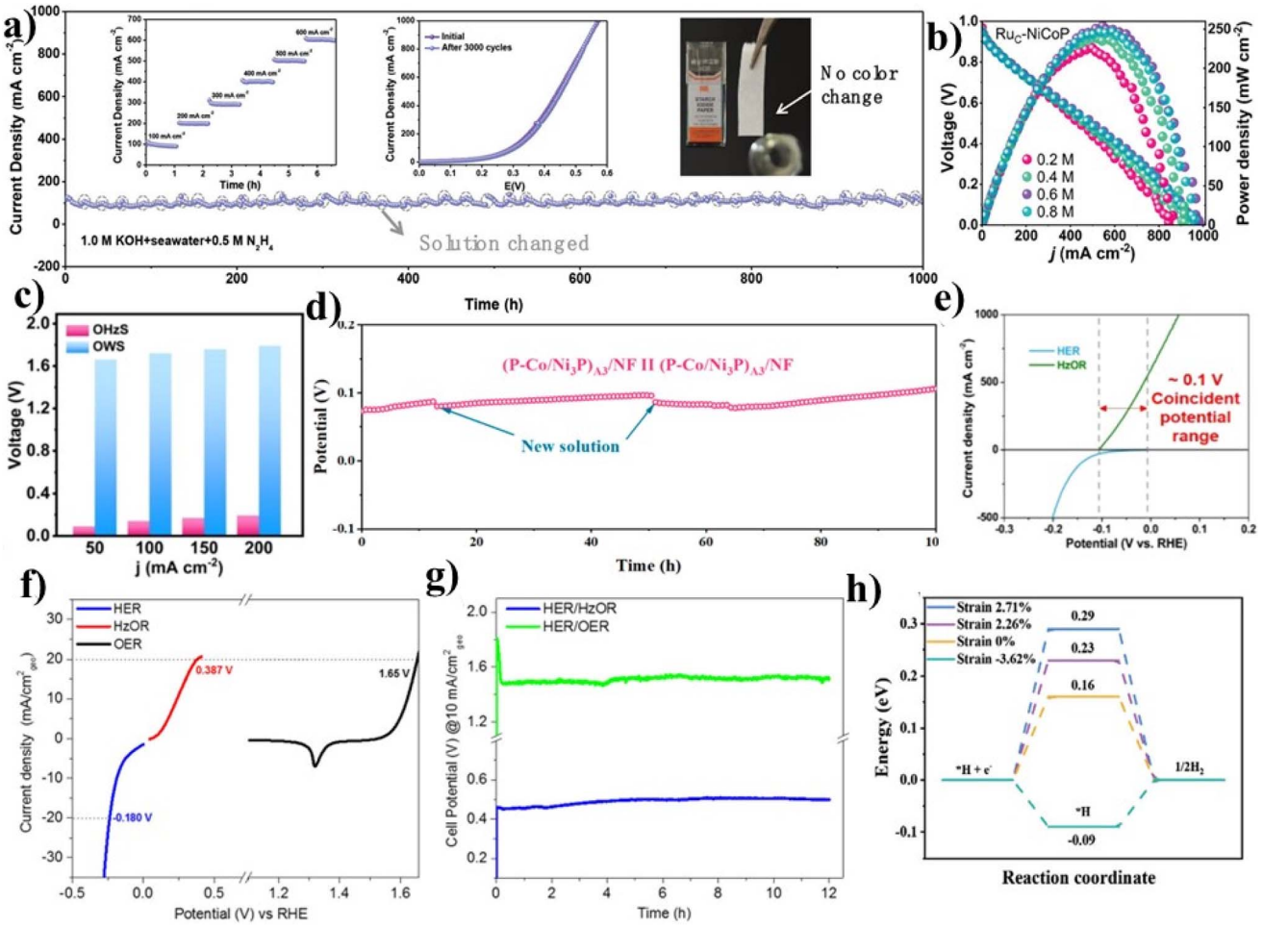

Fig. 7 (a) Chronoamperometric *I*–*t* curve for Mo–Ni_2P_v@MNF electrode pair measured in 1.0 M KOH + seawater + 0.5 M N_2H_4 over 1000 h, Reproduced from ref. 39, with permission from Wiley, *Advanced Functional Materials*, 2023, **33**, 2300625, Copyright 2023. (b) Discharge polarization curves and corresponding power density plots for direct hydrazine-oxygen fuel cell (DHzFCs) using Ru_C–NiCoP catalyst, Reproduced from ref. 85, with permission from Wiley, *Advanced Functional Materials*, 2025, **35**, 2422634, Copyright 2025. (c) Comparison of the cell voltages at 50, 100, 150 and 200 mA cm^{-2} for OWS and OHzS using symmetric Ru_1–NiCoP electrodes, Reproduced from ref. 148, with permission from Wiley, *Angewandte Chemie International Edition*, 2023, **62**, e202308800, Copyright 2023. (d) Chronoamperometric stability of $(P–Co/Ni_3P)_{A3}$/NF-based electrolyzer, Reproduced from ref. 150, with permission from ACS, *ACS Sustainable Chemistry & Engineering*, 2023, **11**, 14186–14196, Copyright 2023. (e) overlapping potential region between HER and HzOR polarization curves observed for NiCoP/NF, Reproduced from ref. 151, with permission from ACS, *ACS Nano*, 2023, **17**, 10965–10975, Copyright 2023. (f) LSV curves of hydrazine electrolysis (1.0 M KOH with 100 mM hydrazine), the HER, and water oxidation (1.0 M KOH), (g) chronopotentiometric curve to obtain a current density of 10 mA cm_{geo}^{-2} in 1.0 M KOH with 0.5 M hydrazine (blue line) and without hydrazine using the Ni_2P-cys||Ni_2P-cys (green line) electrode, Reproduced from ref. 152, with permission from ACS, *Inorganic Chemistry*, 2022, **61**, 4394–4403, Copyright 2022. and (h) ΔG_{H*} diagram for Ni_2P/NF, Cu_1Co_2–Ni_2P/NF, Co–Ni_2P/NF, and Cu–Ni_2P/NF with 0%, −3.62%, +2.26%, and +2.71% strains, respectively, Reproduced from ref. 154, with permission from Wiley, *Advanced Materials*, 2023, 35, 2305598, Copyright 2023.

Open Access Article. Published on 12 May 2026. Downloaded on 6/5/2026 6:21:18 AM. This article is licensed under a Creative Commons Attribution 3.0 Unported Licence.

−89 mV for HzOR at 10 and 100 mA cm^{-2}, respectively, and cut the cell voltage for hydrazine coupled electrolysis by 1.77 V *versus* conventional electrolysis. DFT modelling revealed that Ru clusters strengthened charge redistribution and lowered energy barriers for key intermediates. A self-powered system subsequently achieved an H_2 production rate of 4.9 mmol cm^{-2} h^{-1}.

A hierarchical NiMo/Ni_2P heterojunction with an ohmic interface was fabricated *via* hydrothermal-phosphatidic electrodeposition.[147] As summarised in Table 2, the catalyst exhibited excellent bifunctional activity toward HER and HzOR. The presence of ohmic-contact-driven charge transfer and strain-induced electron redistribution optimised hydrogen adsorption thermodynamics and lowered the energy barrier for hydrazine dehydrogenation, thereby accelerating reaction kinetics and enabling highly efficient hydrazine coupled electrolysis.

Ru single atoms anchored on NiCoP nanowire arrays (Ru_1–NiCoP) were produced by hydrothermal growth, phosphorization, and Ru immobilisation, yielding twisted nanowires with 0.9 wt% isolated Ru.[148] These Ru atoms formed Ni(Co)–Ru–P sites (Ru–P_4Ni/Co_2). The catalyst required −60 mV for HzOR and 32 mV for HER at 10 mA cm^2; in a two-electrode cell, it delivered 522 mA cm^{-2} at 0.3 V and only 90 mV at 50 mA cm^{-2} (Fig. 7c). DFT calculations showed that Ru shifted the d-band centre, strengthened N_2H_4 adsorption, balanced H adsorption, and lowered barriers. Coupled to a direct hydrazine fuel cell, the system produced 24.0 mol H_2 h^{-1} m^{-2}. Hydrothermal-phosphidation produced vertically aligned NiFeP nanosheets on Ni foam.[149] The catalyst delivered 148 mV for HER and 0.1 V for overall hydrazine splitting at 10 mA cm^{-2}, operating stably for 40 h. Synergistic Ni–Fe sites, high conductivity, and porous nanosheets accelerated charge/mass transfer. Seawater tests showed chlorine-free operation, confirming practical viability.

Fe-doped NiCoZnP nanoneedle-assembled nanospheres on Ni foam were prepared *via* hydrothermal growth, Fe doping and phosphidation.[100] As summarised in Table 2, the catalyst exhibited excellent bifunctional activity toward HER and HzOR together with outstanding long-term stability. Fe doping shifted the d-band center, optimized intermediate adsorption and lowered barriers, while the Ni_2P–Co_2P–Zn_3P_2 heterostructure and nanoneedle morphology provided abundant active sites and rapid charge transfer. In a two-electrode cell, overall hydrazine splitting operated at 0.33 V for 100 mA cm^{-2}, substantially outperforming conventional water splitting. A hydrothermal-phosphorization sequence delivered Fe-doped Ni_2P nanosheets decorated with CeO_2 (Fe–Ni_2P/CeO_2).[57] The ultrathin nanosheet architecture provides abundant exposed active sites and facilitates rapid charge transport. As summarised in Table 2, the catalyst exhibits efficient bifunctional activity toward HER and HzOR and stable operation in hydrazine-assisted electrolysis. Synergistic Fe doping and CeO_2 decoration tuned the electronic structure, optimised intermediate adsorption, and lowered water-dissociation barriers while suppressing chlorine evolution, enabling energy-efficient seawater hydrogen production.

Alternating electrodeposition produced (P–Co/Ni_3P)A_3/NF, a hierarchical heterostructure that required 10 mV for HER and −79 mV for HzOR at 10 mA cm^{-2} and remained stable for 20 h (Fig. 7d).[150] Synergistic P–Co/Ni_3P phases furnished abundant active sites, tuned electronic structure, and accelerated charge transfer. The electrolyser operated at 50 mV for 300 mA cm^{-2}, cutting 1.77 V off conventional water splitting. The method offered scalable, low-cost fabrication of self-supporting electrodes. Electrodeposition plus phosphidation produced a 3D Ni_2P/Co_2P microsphere array on Ni foam.[151] XPS and DFT calculations showed interfacial electron redistribution that set ΔG_{H^*} to 0.07 eV for HER and lowered HzOR barriers. The catalyst required 70 mV for HER and 230 mV for HzOR at 10 mA cm^{-2}, with Tafel slopes of 69 and 14 mV dec^{-1}. A 0.1 V potential coincidence region (Fig. 7e) enabled self-activated electrolysis without external power. Practical uses included seawater hydrazine splitting (107 mV@100 mA cm^{-2}, 96 h stable), wastewater treatment, and Zn-Hz batteries achieving 95% efficiency. A ligand-controlled hydrothermal route selectively produced Ni_2P and $Ni_{12}P_5$ phases.[152] Thiol ligands stabilised Ni_2P, whereas carboxylate ligands drove conversion to $Ni_{12}P_5$ within 5 h. The ligand-capped Ni_2P exhibited a mesoporous architecture and a high electrochemically accessible surface area (100 μF cm^{-2}), resulting in superior bifunctional activity toward HER and HzOR, as summarised in Table 2. The performance arose from favourable H_2O adsorption, rapid charge transfer, cysteine-mediated electron donation, and a stable nanoparticle network that endured 12 h of operation (Fig. 7f and g). A hydrothermal-phosphating route produced CoP/Ni_2P nanowires on Ni foam.[153] Vertically aligned heterostructures delivered −75.1 mV for HzOR and 216.1 mV for HER at 10 and 300 mA cm^{-2}, respectively, and required only 0.108 V for hydrazine-assisted splitting *versus* 1.695 V for conventional electrolysis. Synergistic CoP–Ni_2P interfaces accelerated charge transfer, tuned intermediate adsorption, and exposed abundant active sites, while nanowires promoted mass transport.

Hydrothermal growth followed by phosphidation produced Ni–Co–P/NF, a 3D nanoarray of CoP nanoparticles on NiCoP nanowires.[84] It required 37 mV for HER and −61 mV for HzOR at 10 mA cm^{-2}, and remained stable for 100 h. The heterostructure tuned the electronic configuration, lowered energy barriers, and introduced a new N–N cleavage pathway above 0.2 V. Transiently oxidised MPO_x was self-repaired by hydrazine to active MP, ensuring durability. An electrolyser reached 500 mA cm^{-2} at 0.498 V, and a hydrazine-fuel-cell-coupled system delivered 19.6 mol h^{-1} m^{-2} of H_2. A dual-cation Cu/Co co-doping strategy introduced −3.62% compressive strain into Ni_2P, yielding the Cu_1Co_2–Ni_2P/NF catalyst.[154] This strain-optimised material delivered 10 and 100 mA cm^{-2} at only 0.16 V and 0.39 V, respectively, for hydrazine-coupled electrolysis. The strain tightened intermediate adsorption, lowered energy barriers, and shifted the d-band centre toward the Fermi level (Fig. 7h). DFT confirmed that the compression reduced the potential-determining step barrier for HzOR and accelerated water dissociation for HER, leading to markedly enhanced bifunctional performance.

 This journal is © The Royal Society of Chemistry 2026

Open Access Article. Published on 12 May 2026. Downloaded on 6/5/2026 6:21:18 AM.
This article is licensed under a Creative Commons Attribution 3.0 Unported Licence.

Among the catalysts studied, Ru-cluster-decorated NiCoP (RuC–NiCoP) stands out for its exceptional bifunctional activity. It required only 10 mV (HER) and −89 mV (HzOR) at 10 and 100 mA cm^{-2}, cutting 1.77 V off traditional electrolysis. Ru clusters enhanced charge redistribution and lowered energy barriers. Coupled with a direct hydrazine fuel cell, it produced 4.9 mmol H_2 cm^{-2} h^{-1}, offering superior efficiency, low energy consumption, and remarkable stability, ideal for industrial hydrogen production.

4.5 Nickel chalcogenides

Nickel chalcogenides, especially sulfides and selenides, have emerged as promising bifunctional electrocatalysts owing to their metallic conductivity, tunable electronic structure, and intrinsic catalytic activity. The integration of heteroatoms, interface engineering, and vacancy modulation within these systems has yielded significant progress in HzOR and HER, often surpassing traditional OER-based electrolysers.

4.5.1 Sulfides. Ni-based sulfides have demonstrated excellent activity in HzOR and HER due to their intrinsic metallic conductivity, defect tolerance, and favourable surface chemistry.

The Ni/Ni_3S_4/1T-MoS_2/CC catalyst, synthesised *via* a one-step hydrothermal approach, featured a hierarchical architecture with expanded interlayer spacing (1.17 nm) and a metallic 1T-MoS_2 phase.[45] Its superhydrophilic and superaerophobic

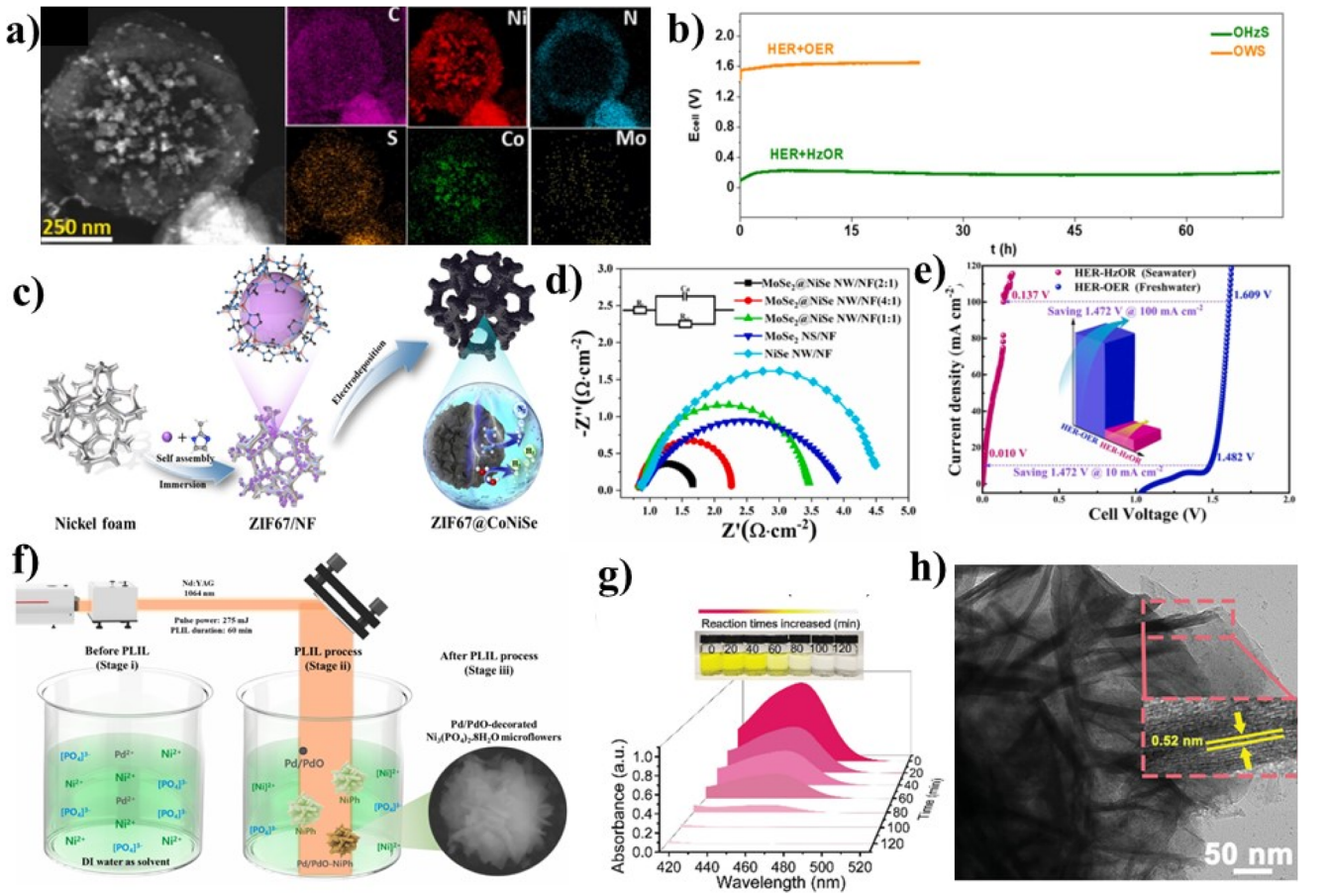

Fig. 8 (a) EDS elemental mapping images of NiCoMoS@$Ni(CN)_2$, Reproduced from ref. 156, with permission from Elsevier, *International Journal of Hydrogen Energy*, 2024, **86**, 554–563., Copyright 2024. (b) Long-term durability test of hydrazine electrolysis at a current density of 100 mA cm^{-2} without *iR* compensation using symmetric NiMoPSO NCAs/NF electrodes, Reproduced from ref. 158, with permission from ACS, *ACS Catalysis*, 2022, **12**, 14387–14397, Copyright 2022. (c) Schematic illustration of the synthesis strategy for ZIF67@CoNiSe hybrid nanostructure. Reproduced from ref. 160, with permission from Elsevier, *Journal of Colloid and Interface Science*, 2023, **630**, 888–899, Copyright 2023. (d) Nyquist plots measured at 0.2 V *vs.* RHE along with H_2 generation performance comparison using a two electrode $MoSe_2$@NiSe NW/NF (2 : 1) electrolyser, Reproduced from ref. 161, with permission from Elsevier, *International Journal of Hydrogen Energy*, 2024, **78**, 1048–1059, Copyright 2024. (e) Comparison of HER-OER coupling in freshwater and HER-HzOR coupling in seawater using Ru–(Ni/Fe)C_2O_4 catalyst at 25 °C, Reproduced from ref. 166, with permission from Elsevier, *Applied Catalysis B: Environmental*, 2023, **325**, 122354, Copyright 2023. (f) Schematic diagram of PLIL-assisted synthesis method for Pd/PdO nanoparticle decorated $Ni_3(PO_4)_2 \cdot 8H_2O$ microflower structure, Reproduced from ref. 168, with permission from Elsevier, *International Journal of Hydrogen Energy*, 2024, **57**, 176–186, Copyright 2024. (g) UV-vis absorption spectra and optical image showing the colourimetric detection of N_2H_4 in electrolyte after electrolysis at 500 mA cm^{-2} using Pt@NiFc-MOF, evaluated at different time intervals, Reproduced from ref. 48, with permission from Wiley, *Advanced Functional Materials*, 2025, 35, 2401011, Copyright 2025. (h) TEM image of Ru_c/NiFe-LDH electrocatalyst, Reproduced from ref. 169, with permission from Wiley, *Advanced Materials*, 2024, **36**, 2401694, Copyright 2024.

Open Access Article. Published on 12 May 2026. Downloaded on 6/5/2026 6:21:18 AM. This article is licensed under a Creative Commons Attribution 3.0 Unported Licence.

surface enhanced electrolyte access and gas evolution, enabling excellent bifunctional activity with a 24 mV HER overpotential and near-zero HzOR onset. DFT studies revealed a remarkably low energy barrier (0.06 eV) for HzOR. Notably, seawater electrolysis required only 17 mV at 10 mA cm^{-2} and remained stable for 100 h under solar power, highlighting the synergy of phase engineering and Ni doping.

A Co incorporated hybrid, Co–FeNiSOH/NFF, fabricated *via* a two-step oxidation process, comprised CoS-decorated nanosheets with uniformly distributed Co^{2+}, Fe^{3+}, and Ni^{2+} species.[155] As summarised in Table 2, the resulting multiphase interphase exhibits excellent bifunctional activity toward HER and HzOR together with high faradaic efficiency and long-term operational stability. The superior performance is attributed to synergistic charge redistribution and adsorption-energy modulation at the multiphase interface, as well as a large electrochemically accessible surface area and accelerated charge-transfer kinetics. In another design, NiCoMoS@$Ni(CN)_2$ core–shell catalyst was synthesised *via* thiolate-induced defect engineering. The metallic NiCoMoS core offered high conductivity, while the $Ni(CN)_2$ shell ensured structural integrity Fig. 8a.[156] Abundant sulfur vacancies and interfacial modulation promoted efficient kinetics, enabling HzOR and HER at overpotentials of 25 mV and 175 mV, respectively, at 100 mA cm^{-2}. The catalyst delivered 0.36 V at 200 mA cm^{-2} with 100% faradaic efficiency, highlighting its practical potential.

A mixed-phase Ru–VO_x/Ni_3S_2 heterostructure, developed through hydrothermal synthesis and Ru doping, integrated a crystalline Ni_3S_2 core with an amorphous Ru–VO_x shell.[157] As summarised in Table 2, the amorphous/crystalline interphase together with Ru-induced electronic modulation substantially increases the density of accessible active sites and promotes rapid charge transport. These synergistic effects endow the catalyst with outstanding multifunctional electrocatalytic capability and long-term operational stability in hydrazine-assisted water-splitting systems. Gao *et al.* introduced a high-entropy NiMoPSO electrode with a hierarchical nanocolumn structure and multiphase composition.[158] DFT calculations and scanning electrochemical microscopy (SECM) analyses confirmed superior electronic conductivity and reaction kinetics. The catalyst achieved ultralow overpotentials of 41 mV (HER) and −59 mV (HzOR) and long-term stability (Fig. 8b). When powered by waste solar cells, the system delivered 1600 mA cm^{-2} at 0.551 V, reducing energy costs by ~73%.

In another report, Praveen *et al.* developed a P–$NiCo_2S_4$ electrocatalyst *via* one-step hydrothermal synthesis using red phosphorus, which enabled direct phase formation and enhanced electronic properties.[159] The catalyst exhibited outstanding bifunctional activity, requiring only 0.19 V for HzOR and 0.24 V for overall hydrazine splitting, significantly lower than traditional water electrolysis. DFT analysis revealed improved charge distribution and lattice stability. The catalyst also demonstrated long-term durability without relying on costly metal substrates. Among Ni-based sulfides, the mixed-phase Ru-VO_x/Ni_3S_2 heterostructure excels due to its crystalline core and amorphous Ru-VO_x shell, which synergistically enhances active site density and charge transport. It delivered ultralow overpotentials of 7 mV (HER), −66 mV (HzOR), and 215 mV (OER) at 10 mA cm^{-2}, with a record-low hydrazine splitting cell voltage of 15 mV and stable for 100 hours operation, marking it as a highly efficient, durable catalyst for hydrogen production.

4.5.2 Selenides. Nickel selenides exhibit superior electrocatalytic performance due to their enhanced conductivity, tunable Ni–Se interactions, and superior corrosion resistance.

The ZIF67@CoNiSe-3 catalyst, featuring a core–shell nanoflower structure with porous ultrathin nanosheets.[160] Fabricated *via* ultrasound-assisted self-assembly and electrodeposition (Fig. 8c), the catalyst offered a high surface area (476.9 m^2 g^{-1}) and abundant active sites. It exhibited excellent HER (49 mV at 10 mA cm^{-2}) and HzOR (400 mA cm^{-2} at 0.13 V) performance. DFT calculations revealed that synergistic effects and favourable energetics enhanced its catalytic activity and stability.

A hierarchical $MoSe_2$@NiSe core–shell heterostructure nanoarray grown on nickel foam as an efficient bifunctional electrocatalyst for water splitting and hydrazine-assisted hydrogen production.[161] Synthesised *via in situ* selenylation of $Ni(OH)_2$ nanorods with $MoSe_2$ deposition, the catalyst featured a unique 1D/2D architecture. It achieved low overpotentials for HER (105 mV) and OER (220 mV) and required only 0.50 V for hydrazine-assisted splitting. EIS confirmed excellent charge transfer kinetics, revealing a low charge transfer resistance of just 0.5 Ω cm^{-2} for HzOR (Fig. 8d). DFT analysis showed that enhanced activity was due to interfacial electron transfer and optimised intermediate adsorption. The NiSe-2 catalyst, synthesised *via* one-step electrodeposition, exhibits a nanoporous morphology, with an optimised Ni/Se ratio (1 : 1).[28] This structure promoted a highly active surface area and facilitated electron transport. NiSe-2 achieved a low OER overpotential (252 mV at 10 mA cm^{-2}) and high HzOR current density (318 mA cm^{-2} at 0.4 V *vs.* RHE). Its superaerophobic nature and mixed conductive Ni_3Se_4/$NiSe_2$ phases facilitated mass transport and stability.

In a hybrid electrolysis setup, it delivered a low cell voltage of 0.356 V, underscoring its practical viability. The study developed a defect-rich Ni–Cu–Se electrocatalyst with hierarchical porous nanosheets and $NiSe_2$/CuSe heterojunctions *via* hydrothermal synthesis and defect engineering.[162] As summarised in Table 2, the catalyst exhibits excellent bifunctional activity and stability in hydrazine-assisted hybrid electrolysis systems. The enhanced performance is attributed to defect-induced charge redistribution at the heterointerface and superaerophobic surface characteristics, which collectively facilitate efficient gas release, rapid charge transfer, and durable operation, offering a cost-effective strategy for sustainable hydrogen production.

Li *et al.* developed a bifunctional NiSe/NF electrocatalyst composed of ultrathin NiSe nanosheets (3–5 nm) grown on nickel foam *via* hydrothermal synthesis and selenization.[163] The catalyst exhibited excellent HER (95 mV at 10 mA cm^{-2}) and HzOR (100 mA cm^{-2} at 0.35 V) performance. In a two-electrode system, it achieved an ultralow cell voltage of 310 mV and stable operation for 30 hours. Its high activity stemmed from the nanosheet structure, electronic optimisation, and strong substrate adhesion.

 This journal is © The Royal Society of Chemistry 2026

Open Access Article. Published on 12 May 2026. Downloaded on 6/5/2026 6:21:18 AM. This article is licensed under a Creative Commons Attribution 3.0 Unported Licence.

Wang *et al.* developed a bifunctional P/Fe co-doped $NiSe_2$ electrocatalyst with ultrathin nanosheets (3–5 nm) grown on modified nickel foam for efficient hydrazine coupled electrolysis.[164] Synthesised *via* electrodeposition, selenisation, and phosphorus doping, the catalyst achieved low overpotentials of 74 mV for HER and 200 mV for HzOR. In a two-electrode system, it delivered a cell voltage of just 310 mV at 10 mA cm^{-2} and maintained excellent stability over 100 hours, attributed to P/Fe-induced electronic tuning and a favourable "2 + 2" reaction mechanism. Ru-doped NiSe (Ru–NiSe) nanoparticles synthesised *via* hydrothermal synthesis for efficient freshwater and seawater electrocatalysis.[165] Ru^{3+} incorporation into the NiSe lattice enhanced charge mobility and active site density. The catalyst achieved excellent HzOR (0.70 V) and OER (1.57 V) performance, with even better efficiency in seawater. The substitution of OER with HzOR reduced the cell voltage by 0.78 V and boosted hydrogen production by 1.8×, demonstrating strong promise for seawater splitting applications.

Among nickel selenides, the Ru-doped NiSe (Ru–NiSe) nanoparticles stand out for their enhanced charge mobility and increased active site density due to Ru^{3+} incorporation. They deliver excellent HzOR (0.70 V) and OER (1.57 V) performance, reducing cell voltage by 0.78 V when replacing OER with HzOR, thereby boosting hydrogen production by 1.8×, demonstrating superior efficiency and strong potential for sustainable freshwater and seawater hydrogen electrocatalysis.

4.6 Nickel oxalate and phosphate

Nickel oxalate and phosphate materials were explored as versatile platforms for HzOR and hydrazine-coupled electrolysis due to their structural flexibility and tunable electronic properties.

A notable example was a Ru-implanted Ni/Fe-oxalate solid-solution electrocatalyst (Ru-(Ni/Fe)C_2O_4), synthesised through an impregnation and solvothermal method. The catalyst featured a hierarchical microstructure with abundant high-index facets and exhibited outstanding trifunctional activity, achieving ultralow overpotentials for HER (42 mV), HzOR (0.062 V), and OER (1.486 V).[166] In a HER-HzOR seawater electrolyser, it delivered a current density of 10 mA cm^{-2} at only 0.01 V, representing a 1.4 V reduction compared to conventional HER-OER systems (Fig. 8e). This exceptional performance was attributed to the Ru–Ni/Fe synergistic interaction, efficient charge transport, and long-term stability at 500 mA cm^{-2} and 80 °C without chlorine evolution. Another study reported the development of an $SNiC_2O_4$–Nb_2O_5/NF hybrid catalyst with a unique prism-sphere morphology, synthesised *via* a low-temperature two-step method.[167] Electron transfer from Ni to Nb optimised the electronic structure, enhancing both HER and OER performance. Additionally, Nb_2O_5 promoted water dissociation and reduced the energy barrier for the Volmer step. The catalyst exhibited low overpotentials for HER (155 mV) and OER (293 mV) and enabled a 1.41 V reduction in overall voltage by replacing the sluggish OER with HzOR, owing to synergistic interactions and improved charge transfer dynamics.

In a separate study, a Pd/PdO-NiPh hybrid catalyst was fabricated *via* a one-step pulsed laser irradiation method, forming a microflower-like morphology with Pd/PdO nanoparticles uniformly distributed on NiPh[168] (Fig. 8f). Structural and XPS analysis confirmed monoclinic $Ni_3(PO_4)_2 \cdot 8H_2O$ formation and revealed electron transfer from Ni to Pd/PdO, which modulated the electronic environment and enhanced catalytic performance. The catalyst achieved overpotentials for HER (298 mV) and HzOR (506 mV) and enabled hydrazine coupled electrolysis at just 0.538 V. Synergistic effects and phosphate-induced electron donation boosted performance, offering a scalable, energy-efficient hydrogen production strategy.

4.7 Nickel-based metal–organic frameworks (MOFs)

Nickel-based MOFs have shown great promise for HzOR and HER due to their tunable porosity, high surface area, and ability to host multi-metal active sites. Interface engineering, doping, and heterostructure formation further enhance their catalytic efficiency.

For example, a Pt@NiFe-MOF Mott–Schottky heterojunction catalyst was synthesised *via* a two-step hydrothermal and *in situ* etching method,[48] exhibiting excellent performance for hydrazine oxidation (1500 mA cm^{-2} at 357 mV) and hydrogen evolution (100 mA cm^{-2} at 71 mV). The built-in electric field at the Pt/NiFe-MOF interface enhanced electron transfer and intermediate adsorption, while the nanosheet morphology and oxygen vacancies improved mass transport and conductivity. Beyond electrocatalysis, it degraded hydrazine in wastewater (718 ppb to 6 ppb in 120 min, (Fig. 8g)) and achieved 415.2 mW cm^{-2} in a hydrazine-H_2O_2 fuel cell.

A hierarchical Ir-doped Ni/Fe-MOF (MIL-(IrNiFe)@NF) catalyst synthesised *via* a one-step hydrothermal method.[170] It achieved 100 mA cm^{-2} at 69 mV for HER and 500 mA cm^{-2} at 220 mV for HzOR in seawater. In a two-electrode setup, it enabled overall seawater splitting at 1000 mA cm^{-2} with only 0.69 V, significantly reducing energy input. The superior performance was attributed to Ir-induced electronic modulation, abundant active sites from the microsphere morphology, and stable NiFe oxyhydroxide formation during operation.

In another study, FeCo–Ni_2P@MIL-FeCoNi heterostructure arrays were fabricated on nickel foam *via* hydrothermal synthesis and phosphorization.[171] The catalyst showed excellent bifunctional activity with ultralow overpotentials (42 mV for HzOR, 310 mV for HER at 1000 mA cm^{-2}) and long-term stability. Dual doping and heterojunction engineering optimised electronic structure and reaction kinetics, which enabled efficient hydrazine-assisted seawater splitting, requiring only 400 mV and saving 3.03 kWh Nm^{-3} H_2, offering a promising route for sustainable hydrogen production. The study synthesised NiRh-terephthalic acid (BDC) nanosheets on nickel foam *via* a solvothermal method, with Rh atoms partially substituting Ni in the framework.[30] The catalyst exhibited vertically aligned nanosheets with atomic Rh dispersion, achieving ultralow overpotentials of 49 mV for HER and 17 mV for HzOR at 10 mA cm^{-2} in alkaline seawater. Dual active sites

Open Access Article. Published on 12 May 2026. Downloaded on 6/5/2026 6:21:18 AM. This article is licensed under a Creative Commons Attribution 3.0 Unported Licence.

and electronic modulation enhanced activity, enabling overall hydrazine-assisted seawater splitting at just 0.06 V with excellent 60 hours stability.

Among nickel-based MOFs, the NiRh-BDC nanosheets show ultralow overpotentials of 49 mV (HER) and 17 mV (HzOR) at 10 mA cm^{-2} in alkaline seawater. Their vertically aligned nanosheets with atomic Rh dispersion create dual active sites and optimised electronic structure, enabling efficient hydrazine-assisted seawater splitting at only 0.06 V with excellent 60 hours stability, making them highly promising for sustainable hydrogen production.

4.8 Nickel-based layer double hydroxides

Nickel-based LDHs have emerged as promising electrocatalysts for HzOR and HER due to their layered architecture, high surface area, and tunable composition. Recent advances have shown that incorporating noble metals such as Ru into Ni-based LDHs can significantly enhance their electrocatalytic activity through electronic structure modulation and improved active site exposure. A Ru/NiCo LDH heterostructured catalyst, synthesised *via* hydrothermal and impregnation methods, showed excellent bifunctional activity with overpotentials of 19 mV (HER) and −118 mV (HzOR) at 10 mA cm^{-2}.[172] Ru doping optimised the electronic structure, lowered the d-band centre and ΔG_{H^*} (0.23 eV), and enhanced reaction kinetics. The catalyst offered low charge transfer resistance, abundant active sites, and achieved 100 mA cm^{-2} at just 0.223 V in hydrazine-coupled electrolysis.

Another Ru cluster-anchored NiFe-LDH heterostructure (Ru_a/NiFe-LDH) was synthesised *via* a one-step hydrothermal method, with TEM confirming uniform Ru dispersion on nanosheets[169] (Fig. 8h). The catalyst achieved ultralow overpotentials of 26 mV (HER) and −75 mV (HzOR) at 10 mA cm^{-2} and maintained stability for 100 hours. It delivered industrial-scale current (1 A cm^{-2} at 0.43 V), offering 79.3% energy savings. Ru–O–Ni/Fe bridges modulated the d-band and optimised ΔG_{H^*} (−0.21 eV), as validated by DFT.

4.9 Discussion

The classification of nickel-based catalysts into metallic/alloy, oxide/hydroxide, nitride, phosphide, and chalcogenide families provides a clear framework for analysing their distinct structural and electronic features toward HzOR and hydrazine-assisted HER. Considerable progress has been achieved across all these material classes, with many systems demonstrating remarkably low overpotentials and favourable reaction kinetics. At the same time, continued efforts are needed to further clarify intrinsic activity, stability, and the identity of the true catalytically active phases under operating conditions.

In many reports, catalytic performance is primarily evaluated using geometric current densities, which allows rapid comparison but may not fully capture intrinsic activity. Metrics such as turnover frequency (TOF), electrochemically active surface area (ECSA)-normalised activity, and detailed kinetic parameters remain less frequently reported.[173,174] For example, Ni/NCNFs–Rh reported by Wang *et al.*[41] and Ni–C hybrid nanosheets by Liu *et al.*[32] achieved outstanding bifunctional performance at cell voltages below 0.2 V. These impressive results clearly highlight the effectiveness of hierarchical architectures and conductive supports in enhancing apparent activity. Complementary intrinsic metrics would further enable meaningful benchmarking across different catalyst families and help distinguish active-site enhancement from surface-area or mass-transport effects.

For metallic nickel and its alloys, synergistic electronic effects between Ni and other transition metals have been widely explored to optimise the d-band centre and enhance the adsorption/desorption behaviour of key intermediates. Ni–Cu CNPs[33] and NiCo/$MoNi_4$ heterostructures[115] are typical examples, demonstrating improved conductivity and faster electron transfer. However, the underlying electronic interactions are often only qualitatively discussed based on XPS or DFT-derived charge distribution, without quantitative correlation to experimentally measured reaction kinetics. In addition, most alloy catalysts exhibit surface segregation or partial leaching of secondary metals during long-term electrolysis, leading to unstable surface compositions.[13,175] Extended durability studies at industrially relevant current densities (>0.5 A cm^{-2}) are rarely reported.[32,33] Therefore, although Ni alloys exhibit excellent initial bifunctional activity, their mechanical robustness and compositional stability under continuous hydrazine operation remain key bottlenecks.

In the case of nickel oxides and hydroxides, redox flexibility (Ni^{2+}/Ni^{3+}) and rich defect chemistry contribute to high intrinsic activity. Catalysts such as CoPB@NiFe–OH/NF,[128] NiO/Ru,[130] and NiOOH@CoCu–CH[132] have displayed remarkable HzOR performance due to facile charge transfer and oxygen vacancy-mediated adsorption sites. However, these materials are known to undergo dynamic surface reconstruction under reaction conditions, forming amorphous NiOOH or mixed-metal oxyhydroxide layers. The actual catalytically active species are therefore difficult to identify conclusively. Few studies have conducted *operando* or *in situ* analyses to monitor this phase transformation in real time. Moreover, the poor electrical conductivity of oxide and hydroxide catalysts often necessitates the use of conductive supports such as Ni foam or reduced graphene oxide, which complicates attribution of the observed activity to the intrinsic Ni-based phase.[51,104,176] Additionally, stability under neutral or saline electrolytes remains insufficiently examined, limiting the practical deployment of these systems for large-scale hydrazine-assisted water electrolysis.

Nickel nitrides and phosphides exhibit metallic conductivity and strong hydrazine adsorption, offering promising bifunctional performance at low cell voltages. However, while nitridation or phosphorisation enhances activity *via* electron delocalisation and optimised hydrogen binding, these materials often undergo surface oxidation or *in situ* conversion to hydroxide/phosphate species under alkaline operation.[95,139] The majority of nickel nitrides and phosphides report remarkable overpotential values (as low as 7–55 mV) but do not critically address whether the true catalytically active phase is the pristine nitride/phosphide or a reconstructed derivative. The lack of *operando* XPS/XAFS and isotope labelling studies leaves

Open Access Article. Published on 12 May 2026. Downloaded on 6/5/2026 6:21:18 AM. This article is licensed under a Creative Commons Attribution 3.0 Unported Licence.

mechanistic ambiguities unresolved.[142] In addition, the scalability of synthesis routes (such as ammonolysis or phosphidation under reducing atmospheres) poses environmental and economic challenges rarely discussed in the literature.[135,146]

Across all catalyst categories, integrating kinetic modelling more closely with experimental observations represents a key opportunity for future progress. Although DFT modelling is frequently invoked and has provided valuable insight, future studies should aim to include solvent effects, double-layer interactions, and applied potential influence,[50,91] which will assist predictive catalyst design. Another important dimension is mass transport and wettability. Several studies have reported superhydrophilic or superaerophobic architectures that facilitate bubble release and enhance electrolyte infiltration, such as 3D Ni NCNA and Zn–$NiCoO_{x-z}$ electrodes.[34,45] Future work should aim to include a quantitative analysis of bubble dynamics or hydrazine diffusion under operating current densities.[46] Since gas evolution and mass transfer strongly influence apparent activity, integrating high-speed imaging, *in situ* gas analysis, and modelling of bubble detachment could offer a more rigorous understanding of structure–function relationships.[177,178]

Finally, although nickel-based catalysts show outstanding laboratory performance, long-term stability, safety, and scalability remain major challenges. Hydrazine is a highly toxic and volatile compound; therefore, strategies to minimise crossover, leakage, or decomposition must accompany catalytic studies to ensure safe operation.[87,179] Only a few reports, such as Mo–Ni_2P_4@MNF bifunctional electrodes[39] and W–Ni_3N nanosheets,[50] have demonstrated extended operation (>450 h), yet even these are under controlled laboratory conditions. Expanding such durability evaluations to industrially relevant electrolytes and current densities, combined with *operando* diagnostic tools such as ICP–MS and XAFS, will be crucial for advancing nickel-based catalysts toward real-world deployment.

5 Machine learning (ML): insights and prospects for hydrazine oxidation

The integration of ML and deep learning (DL) into electrocatalysis research has revolutionised the discovery and optimisation of active materials by enabling data-driven predictions and mechanistic understanding that go beyond conventional experimental and computational paradigms.[180–182] Unlike conventional trial-and-error or even high-throughput DFT screening approaches, ML accelerates the identification of high-performance catalysts through the extraction of quantitative structure–property activity relationships and predictive modelling.[183] By learning from both experimental and computational data, ML enables the rapid exploration of vast chemical spaces with minimal human bias.[184] Particularly in the context of the HER and OER, ML has already demonstrated remarkable success in identifying interpretable descriptors, conducting high-throughput screening, and guiding rational catalyst synthesis.[182,185–187] Extending these strategies to the HzOR offers a transformative pathway toward designing energy-efficient and sustainable electrocatalysts for hydrazine-coupled electrolysis.

5.1 ML in HER catalyst design

The HER, proceeding *via* the Volmer–Tafel or Volmer–Heyrovsky pathway, is highly sensitive to surface electronic structure and hydrogen adsorption free energy (ΔG_{H^*}).[70,188,189] ML has been extensively employed to identify key descriptors governing HER activity, including the d-band centre, Bader charge, work function, and local coordination environment, providing insights beyond the traditional Sabatier principle.[190,191]

Early ML–DFT frameworks demonstrated the ability to rapidly screen non-noble metal catalysts with near-optimal ΔG_{H^*} values, significantly expanding the catalyst design space beyond Pt.[192] Neural-network-based approaches, including convolutional neural networks trained on surface structures or electronic density-of-states representations, have further enabled large-scale prediction of adsorption energies with near-DFT accuracy.[193,194] In parallel, interpretable symbolic regression methods such as SISSO have successfully derived low-dimensional descriptors linking electronic structure to HER activity, particularly for transition-metal-based and single-atom catalysts.[195,196]

Beyond computational screening, ML has also been applied to experimental optimisation of HER catalysts, guiding precursor ratios, dopant selection, and synthesis conditions using relatively small datasets.[197,198] Representative examples of descriptor discovery and feature-importance analysis in ML-assisted HER catalyst design are summarised in Fig. 9. Overall, these studies establish ML as a powerful and transferable framework for accelerating HER catalyst discovery.

Furthermore, the availability of extensive computational databases (such as Materials Project, Open Quantum Materials Database (OQMD), Catalysis-Hub and the Open Catalyst Project) has facilitated data-driven catalyst discovery.[200,201] These datasets, when combined with feature engineering or graph-based neural networks like crystal graph convolutional networks (CGCNN), spectral convolutional network (SchNet), and materials graph network (MEGNe), have enabled automated discovery of TM-based HER catalysts with minimal human intervention.[202]

5.2 ML in OER catalyst design

The oxygen evolution reaction (OER) is the kinetic bottleneck in conventional water electrolysis, involving a complex four-electron transfer with multiple oxygen-containing intermediates. Machine learning (ML) has emerged as a powerful approach for uncovering descriptors that correlate electronic structure with catalytic performance, enabling data-driven discovery and optimisation of efficient OER catalysts.[201,202]

Using diverse ML models such as artificial neural networks (ANN), random forest (RF), gradient boosting regression (GBR), and XGBoost regression (XGBR), multiple studies have established predictive frameworks linking catalyst composition, morphology, and testing conditions to electrochemical performance.[203–205] Interpretable tools such as Shapley Additive

Open Access Article. Published on 12 May 2026. Downloaded on 6/5/2026 6:21:18 AM.
This article is licensed under a Creative Commons Attribution 3.0 Unported Licence.

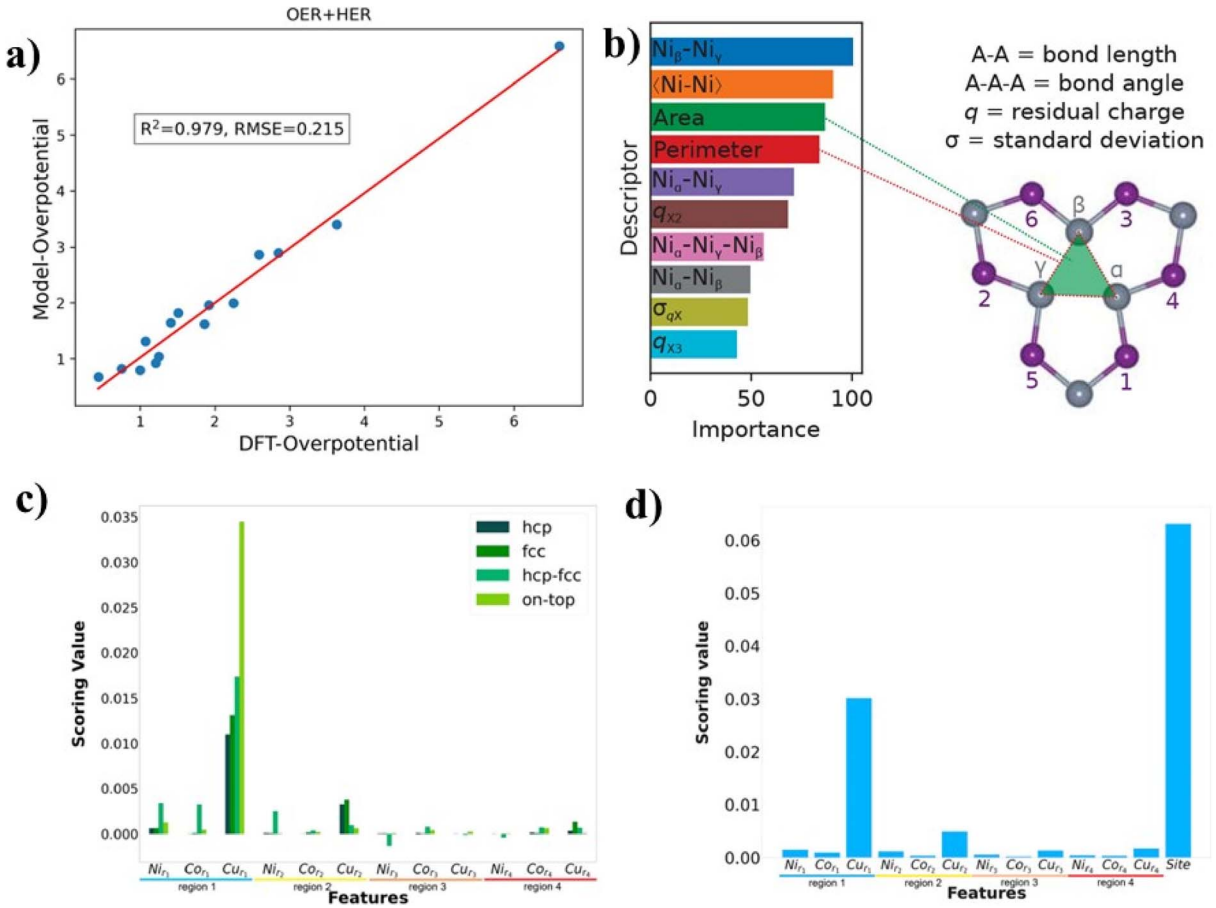

Fig. 9 (a) Performance of the SISSO model for overall water splitting, Reproduced from ref. 196, with permission from ACS, *Chemistry of Materials*, 2025, **37**, 3608–3621, Copyright 2025. (b) Relative importance of descriptors calculated from the RRF model, where the dotted lines represent the definition of descriptors. The authors designate the three Ni atoms as α, β, and γ according to their respective distance from the primary doping site, Reproduced from ref. 198, with permission from ACS, *Journal of the American Chemical Society*, 2018, **140**, 4678–4683, Copyright 2018. (c) Visualization of feature importance based on scoring values (negative mean squared error) for (a) 12 features in individual ML1 models ($ML1_{hcp}$, $ML1_{fcc}$, $ML1_{hcp\text{-}fcc}$, and $ML1_{on\text{-}top}$) using method 1, and (b) 13 features in the ML2 model obtained by merging all the four data sets using method 2. (d) Metal-wise subscripts r_1, r_2, r_3, and r_4 correspond to region 1, 2, 3, and 4 with the microstructures, respectively. Reproduced from ref. 199, with permission from ACS, *The Journal of Physical Chemistry Letters*, 2022, **13**, 7583–7593, Copyright 2022.

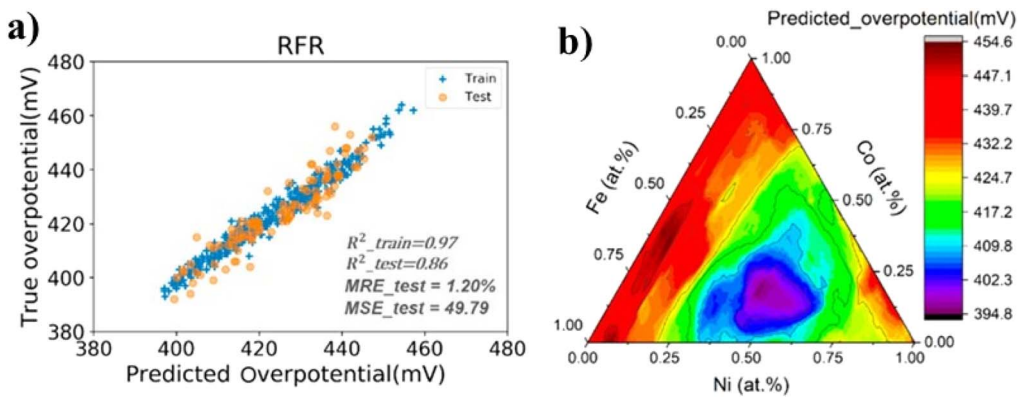

Fig. 10 ML model by RFR, (a) diagonal scatter plot for the predicted OP and the ground truth by RFR, (b) contour map of the predicted overpotential by the RFR model under different compositions. Reproduced from ref. 209, with permission from ACS, *ACS Omega*, 2022, **7**, 14160–14164, Copyright 2022.

Open Access Article. Published on 12 May 2026. Downloaded on 6/5/2026 6:21:18 AM.
This article is licensed under a Creative Commons Attribution 3.0 Unported Licence.

Explanations (SHAP) have revealed that intrinsic properties—including d-electron count, electronegativity, atomic radius, magnetic moment, and orbital occupancy (e_g/t_{2g})—play dominant roles in governing OER activity across oxides, LDHs, MOFs, and multimetallic systems.[203–206]

Notably, ML analysis of ternary NiFeCo (hydro)oxides identified the magnetic moment of metal atoms as a critical descriptor, explaining why ternary active-site environments outperform mono- and bimetallic counterparts and enabling ultra-low overpotentials below 200 mV, consistent with experimental observations of amorphous NiFeCo catalysts exhibiting high activity and long-term stability.[205] Similarly, descriptor-based ML frameworks have shown that OER performance can often be predicted from fundamental atomic features without reliance on exhaustive DFT calculations.[204,207] Beyond descriptor discovery, ML has also been applied directly to experimentally derived OER datasets, enabling prediction of overpotential, optimisation of synthesis parameters, and mapping of composition–activity relationships.[208–210] For example, regression models have been used to optimise Cu/Ni ratios in CuO–NiO composites and to predict OER activity of (Ni–Fe–Co)O_x catalysts with high accuracy, with composition–performance trends visualised through ML-derived contour maps (Fig. 10a and b).[208,209]

It is important to distinguish these data-driven ML approaches, which aim to extract structure–activity relationships and interpretable descriptors, from machine-learned interatomic potentials (MLIPs). MLIPs have primarily been used to accelerate atomistic simulations and explore phase stability or reaction dynamics, such as in metadynamics studies of Ni-doped $BaTiO_3$ and multicomponent Ru-based alloys.[211,212] While valuable for understanding structural evolution, MLIPs do not directly provide catalytic descriptors and are therefore complementary to, rather than substitutes for, descriptor-based ML screening. Advanced symbolic regression methods such as SISSO have further demonstrated strong capability in deriving low-dimensional analytic descriptors for small datasets typical of electrocatalysis, including multitask prediction of OER-related overpotentials and stability windows.[196,213,214] In addition, regularised regression and ensemble models have been successfully applied to large catalyst datasets, enabling rapid identification of OER catalysts outperforming benchmark RuO_2 and guiding the rational design of bifunctional electrocatalysts.[215,216]

Importantly, the descriptor-discovery and data-driven optimisation strategies developed for OER catalysis provide a transferable methodological framework that can be adapted to other multi-electron oxidation reactions, including hydrazine

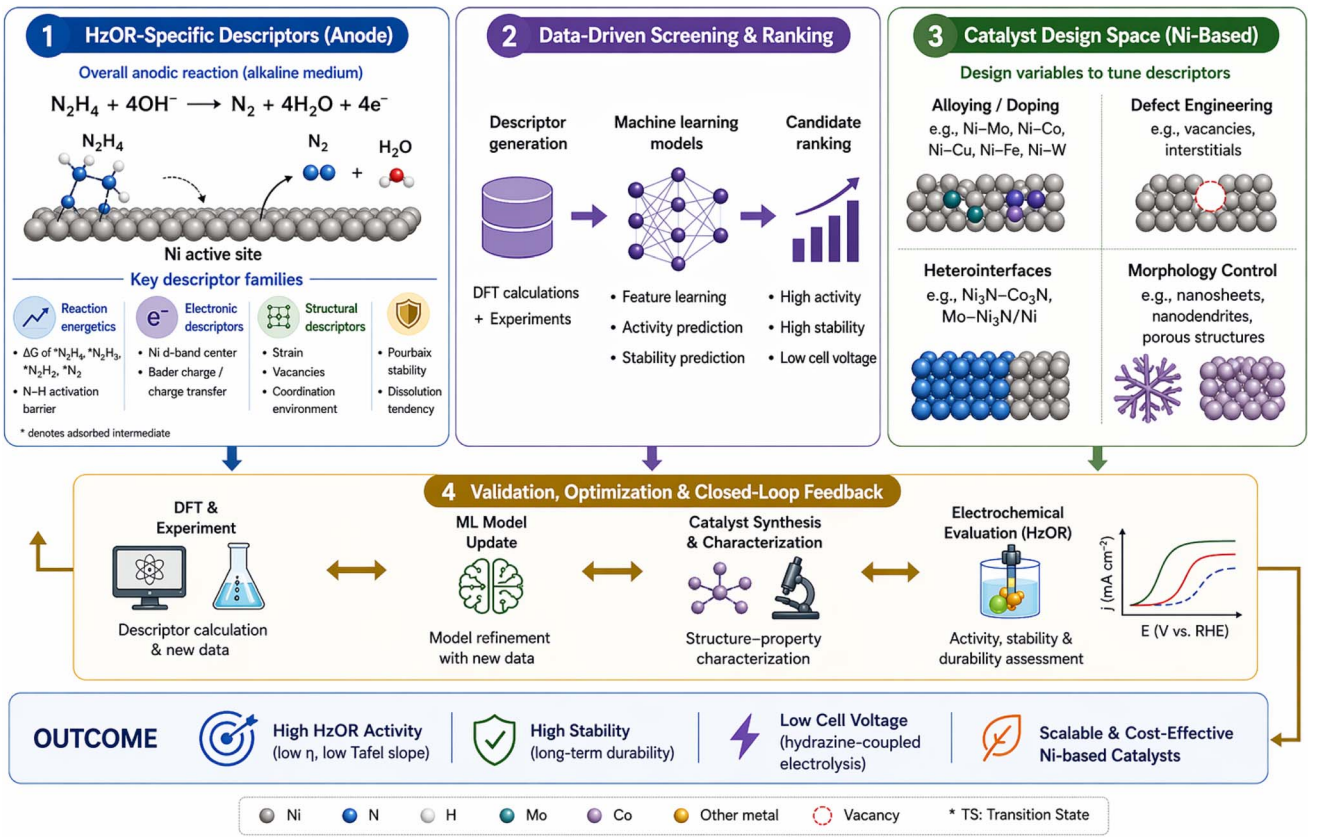

Fig. 11 Roadmap for data-driven HzOR catalyst design. Descriptor-guided framework for designing Ni-based hydrazine oxidation catalysts, linking HzOR-specific reaction, electronic, structural and stability descriptors with machine-learning screening, catalyst design strategies and closed-loop experimental validation to identify active, stable and low-voltage electrocatalysts.

Open Access Article. Published on 12 May 2026. Downloaded on 6/5/2026 6:21:18 AM.
This article is licensed under a Creative Commons Attribution 3.0 Unported Licence.

Table 3 Summary of ML and DL strategies for electrocatalyst design

Reaction/ electrocatalysts	ML/DL algorithm model	Descriptors	Output	Key findings	Ref
HER (Ni_2P, phosphides)	RFF	Ni–Ni bond length, charge distribution	HER activity, ΔG_{H^*}	Nonmetal doping tunes Ni–Ni bond length, enhancing HER activity	198
HER (alloys, intermetallics)	Surrogate ML + DFT	Adsorption energy descriptors (atomic number, electronegativity, coordination)	ΔG_{H^*} and adsorption energy trends	Identified 258 active surfaces across 102 alloys *via* active learning-guided DFT	192
HER ($MoNi_4$/MoO_2@Ni)	ML-enhanced multi-scale X-ray tomography	3D voxel intensity data, morphological parameters (particle size, alignment, porosity)	3D morphology reconstruction, surface area, active-site distribution	ML suppressed artefacts (beam hardening, motion, misalignment) and resolved catalyst hierarchical architecture (20–100 nm NPs on 10–20 μm cuboids); correlated with low HER overpotential (15 mV @ 10 mA cm^{-2})	224
HER + OER (2D structures)	Regression + structural descriptor ML	Rotation angle, bond length, interlayer spacing, bandgap ratio	HER and OER overpotential	$MoTe_2$/WTe_2 predicted as optimal HER-OER bifunctional catalyst	216
HER (amorphous Ni_2P)	ML gemotrical descriptors	Bond distance, cutoff radius, local environment	Adsorption energy (ΔE_{ads})	Decomposed adsorption energy into frozen + relaxation components for amorphous surfaces	225
HER (NiCoCu alloys)	XGBR, SVR (supervised ML)	12 microstructural features (*e.g.*, local composition, atomic radius, coordination, Cur1 region composition)	ΔE_H	ML models predicted ΔE_H for 5400 Ni–Co–Cu alloys; Cu in region 1 (Cur1) most influential; XGBR and SVR efficiently screened active non-precious HER catalysts	199
HER (single atom catalysts)	Compressed sensing (SISSO) and CNNs	Bader charge, d-band center, covalent radius, DOS	HER (overopotential), ΔG_{H^*}	Identified interpretable descriptors linking charge redistribution to HER kinetics	196 and 226
OER (TM/C_3B catalysts)	GBR and SHAP	No. of d-electrons, electronegativity, atomic radius, first ionization energy	ΔG_{OH} and OER overpotential	GBR model accurately predicted ΔG_{OH} (MAE = 0.14 eV); d-electron count (importance = 0.58) most influential; Ni/C_3B exhibited η = 0.41 V	204
OER (NiFeCo ternary oxides)	SISSO	Magnetic moment, oxidation state, composition ratio	Adsorption energy & overpotential	SISSO identified magnetic moment as key descriptor; ternary NiFeCo sites achieved η < 200 mV; amorphous NiFeCo showed 146 mV @ 10 mA cm^{-2}, 300 h stability	205
OER (Ni doped $BaTiO_3$)	ML-accelerated metadynamics	Ni dopant position, bond distortion, surface energy barrier	Free energy barrier, overpotential	Ni doping reduced barrier (1.20 *vs.* 1.57 eV) and η (−0.03 *vs.* 0.34 V); experimentally confirmed η reduction by 0.34 V	211
OER (multi-component alloys)	MLIP and replica-exchange MD	Atomic interactions, mixing energy, short-range order	Phase stability & overpotential	MLIP predicted fcc/hcp mix near equimolar; $Ru_{0.20}(Ir,Fe,Co,Ni)_{0.80}$ showed $\eta \approx$ 237 mV @ 10 mA cm^{-2} & 1.1 mV h^{-1} degradation	212
					227

Open Access Article. Published on 12 May 2026. Downloaded on 6/5/2026 6:21:18 AM.
This article is licensed under a Creative Commons Attribution 3.0 Unported Licence.

Table 3 (*Contd.*)

Reaction/ electrocatalysts	ML/DL algorithm model	Descriptors	Output	Key findings	Ref
OER (Ni electrode thermodynamics)	Regression ML (volcano model)	ΔG_{OH}, ΔG_{O}, ΔG_{OOH} under different pH	Thermodynamic overpotential	ML revealed broad ΔG distribution and pH-dependent η; optimum ΔG_{OH} = 1.23 eV at volcano apex; uncovered hidden reaction pathways	
OER (Ni based LDH)	SVR and RF	e_g and t_{2g} orbital occupancy, orbital center and width (Φ^{M} and Φ^{Ni})	OER overpotential	ML-derived orbital descriptors achieved <0.1 V deviation from DFT; Fe/Co systems enhanced *via* t_{2g} vacancy spin effects, Cu/Zn *via* e_g occupancy (John–Teller); NiZn-LDH most active	206
OER (NiFeCo oxides)	RFR	Variance of first ionization energy (δ_{FIE}), variance of d-orbital electrons (δ_{DE})	OER overpotential	Achieved mean relative error = 1.20%; δ_{FIE} and δ_{DE} identified as dominant features with inverse correlation to overpotential; enabled composition-to-activity mapping for oxides	209
OER ($NiAgO_2$-rGO hybrid)	LR, KNN, SVM, LR	Scan rate, applied potential (experimental inputs)	Current density and overpotential	Four ML models trained on experimental data; LR achieved $R^2 = 1.000$ (at 50 mV s^{-1}), SVM $R^2 \approx 0.86$–0.87; identified 50 mV s^{-1} as optimal scan rate and overpotential = 1.4959 V for 10 mA cm^{-2}; demonstrated ML optimization of real OER performance	210
OER (single atom catalysts)	Multitask SISSO	Bader charge on O*/OH*, d-band center shift	HER + OER or OER + ORR overpotential	Coupling between charge redistribution and d-band shift as governing factor for bifunctional activity; interpretable and transferable descriptors	196
OER (acid stable oxides)	SISSO + Pourbaix data	Charge stability, redox potential, dissolution energy	OER stability and activity	Unified thermodynamic and kinetic descriptors for acid stable OER catalysts	213
OER (2D conducting MOFs)	GBR	17 features (intrinsic metal properties + structural parameters such as bond length & atom count)	ΔG_{OH}, ΔG_{O}, ΔG_{OOH}, overpotential	GBR ($R^2 = 0.937$–0.943) identified 18 MOF catalysts with $\eta < RuO_2$; demonstrated rapid screening of 413 Fe/Ni/Co-based MOFs	228
HER/OER (DL frameworks)	CNN, CGCNN, SchNet, MEGNet	Atomic structure, charge density, DOS images	ΔG_{H^*}, surface stability and adsorption energy	DL eliminates feature engineering; learns from atomic graphs and crystal structure	202
HER/OER (oxides and bifunctional catalysts)	GBR	d-band center, adsorption energy, electronic structure parameters	HER and OER overpotential prediction	GBR model (100 estimators, learning rate 0.05, depth 4) achieved RMSE = 0.043 V, $R^2 = 0.94$ (5-fold CV); efficient for large-scale screening	215

Open Access Article. Published on 12 May 2026. Downloaded on 6/5/2026 6:21:18 AM. This article is licensed under a Creative Commons Attribution 3.0 Unported Licence.

oxidation, where similar challenges in intermediate adsorption and reaction kinetics are encountered.

5.3 Lesson for hydrazine oxidation reaction

The HzOR, a key half-reaction in hydrazine-assisted hydrogen generation, involves sequential N–H bond cleavage and multi-electron transfer steps, rendering its mechanistic complexity comparable to that of the OER. Despite extensive experimental and DFT studies on Ni-based HzOR catalysts, data-driven ML approaches have not yet been systematically applied to this reaction. Lessons from ML-guided HER and OER research indicate that HzOR activity could be effectively modelled using descriptors related to adsorption energies of hydrazine-derived intermediates ($N_2H_4^*$, $N_2H_3^*$, $N_2H_2^*$, N_2H^*), N–H and N–N bond dissociation energies, charge transfer characteristics, and local coordination environments.[217–221]

To move beyond descriptor concepts borrowed from HER and OER, we propose a preliminary framework for HzOR-specific descriptor-guided catalyst design, summarised in Fig. 11. The framework links reaction energetics descriptors (*e.g.*, adsorption energetics and N–H activation barriers), electronic descriptors (*e.g.*, Ni d-band centre and charge transfer), structural descriptors (*e.g.*, vacancies, strain and coordination environment), and stability descriptors (*e.g.*, Pourbaix-informed phase stability) with machine-learning screening and catalyst design variables, including alloying, defect engineering, heterointerfaces and morphology control. Through an iterative feedback loop between DFT, experiment and data-driven optimisation, this framework provides a roadmap for accelerating the discovery of active and stable Ni-based HzOR electrocatalysts.

Furthermore, integrating experimental electrochemical data with DFT-derived descriptors, an approach demonstrated for OER catalysts, could enable holistic modelling of HzOR kinetics and stability (Table 3).[210,216] Multi-objective ML strategies that simultaneously consider activity and durability, combined with small-data methods such as SISSO or Gaussian process regression, offer a practical pathway for accelerating HzOR catalyst discovery.[213,222,223] The absence of ML studies in HzOR, therefore, represents an opportunity to directly transfer mature HER/OER methodologies to hydrazine-coupled electrolysis.

5.4 Discussion

The section highlights the growing potential of ML and DL approaches in electrocatalysis, as evidenced by extensive progress in hydrogen evolution (HER) and oxygen evolution (OER) research. These studies demonstrate that ML can effectively extract interpretable structure–activity relationships, identify key electronic and geometric descriptors, and accelerate catalyst screening and optimisation. Within this context, hydrazine oxidation (HzOR) represents an emerging and promising reaction space where these established methodologies can be naturally extended.

Although HzOR involves sequential N–H bond cleavage steps, it is thermodynamically favourable toward hydrogen evolution ($E^\circ = -0.33$ V *vs.* RHE) and follows a comparatively well-defined reaction pathway. In contrast to the OER, which requires four-electron transfer and multiple oxygen-containing intermediates, HzOR offers a reaction landscape that is amenable to systematic modelling. As such, the application of ML to HzOR is well positioned to benefit from the rich methodological foundation developed for HER and OER, rather than facing fundamentally greater complexity.

Experience from HER and OER research underscores the importance of thoughtful feature selection and descriptor engineering for successful ML implementation. For HzOR, relevant descriptors can be defined in direct analogy to these reactions, including adsorption energies of hydrazine-derived intermediates ($N_2H_4^*$, $N_2H_3^*$, $N_2H_2^*$, N_2H^*), Bader charge analysis, local coordination environment, and N–H or N–N bond

Table 4 Proposed ML and DL models for HzOR catalyst discovery

Proposed model	Representative alograthim	Input descriptors (transferable from HER/OER)	Target output
Descriptor-driven small-data modeling	SISSO/GPR	Adsorption energies of intermediates ($N_2H_4^*$, $N_2H_3^*$, $N_2H_2^*$, N_2H^*); N–H/N–N bond dissociation barriers; Bader charge redistribution; d-band center; work function	ΔE_{ads}, ΔG_{HzOR}, kinetic barriers
Hybrid experimental-computational ML	GBR/RF/SVR	Combined DFT and electrochemical data: adsorption energies, charge transfer, Tafel slope, overpotential, current density	Overpotential, current density, onset potential
High-throughput virtual screening	CNN/GNN/CGCNN/ MEGNet	Atomic structure, coordination graph, DOS maps, charge density, strain tensor	Predicted ΔG_{HzOR}, active site ranking
Active-learning closed loop	Surrogate ML + DFT + experimental feedback	Dynamically updated descriptor database (adsorption, stability, conductivity)	Multi-objective optimization: activity + stability + selectivity
Multitask and stability-aware ML	Multitask SISSO/Pourbaix integrated ML	Formation energy, dissolution potential, vacancy formation, electronic descriptors	Joint prediction of overpotential + stability

Open Access Article. Published on 12 May 2026. Downloaded on 6/5/2026 6:21:18 AM.
This article is licensed under a Creative Commons Attribution 3.0 Unported Licence.

dissociation energies. Compared to OER, HzOR does not require consideration of multiple oxygen intermediates or detailed e_g/t_{2g} orbital occupancy effects, which may simplify descriptor construction. In addition, the integration of experimental electrochemical data with computational descriptors—an approach successfully demonstrated in OER studies—offers a practical route to improving predictive accuracy for HzOR catalysts.

Moreover, the broad range of ML techniques already established in HER and OER research provides a versatile toolkit for HzOR investigations. Supervised learning methods (*e.g.*, RF, SVR, GBR), symbolic regression approaches such as SISSO, and graph-based deep learning models (*e.g.*, GNN, CGCNN) offer complementary strengths in capturing both linear and nonlinear relationships between structure and activity. These approaches enable iterative optimisation of catalytic activity and stability, while interpretable feature-importance analyses support rational catalyst design. Importantly, the current scarcity of large HzOR-specific datasets can be viewed as an opportunity to employ small-data methodologies, such as SISSO and Gaussian process regression (GPR), which are well-suited to extracting meaningful insights from limited but high-quality data (Table 4).

Fig. 12 Schematic roadmap for future directions in Ni-based electrocatalysts for hydrazine-assisted hydrogen production (OHzS).

6 Scalability and practical implementation considerations

Despite substantial advances in nickel-based electrocatalysts for hydrazine oxidation–coupled hydrogen production, their practical deployment remains limited by scalability and system-level challenges. Beyond catalytic activity, scalable synthesis, safe and energy-efficient fabrication, stable operation at industrially relevant current densities, long-term durability, and electrolyser/system integration must be addressed. From a manufacturing perspective, the scalability and reproducibility of electrode fabrication are decisive. Many high-performing nickel-based catalysts are produced *via* multistep hydrothermal/solvothermal synthesis followed by high-temperature post-treatments, which can be batch-limited and less attractive for large-scale electrode manufacturing. In contrast, electrodeposition is widely recognised as an industry-compatible route because it is scalable, controllable, and directly applicable to large-area conductive substrates (*e.g.*, Ni foam, stainless steel), enabling binder-free architectures and improved electrical/mechanical integrity.[229] More broadly, binder-less/self-supported electrodes are increasingly emphasised for practical electrolysis because they simplify manufacturing and mitigate binder-induced resistive losses and delamination risks.[230]

A second critical bottleneck is robust operation at industrially relevant current densities. Many hydrazine-assisted systems are still evaluated at modest current densities, whereas practical electrolysers commonly operate at high current densities (often on the order of $\geq$1 A cm^{-2}, depending on technology and conditions), making mass transport, gas management, and electrode mechanical stability decisive.[231] Accordingly, electrocatalyst benchmarking is increasingly shifting toward ultrahigh-current and long-duration protocols, since degradation processes (surface reconstruction, dissolution/leaching, interfacial failure) can be strongly accelerated under high-rate operation.[232] In parallel, stability-focused perspectives highlight that rigorous durability evaluation must account for structural/chemical evolution of non-noble catalysts under operating conditions, rather than assuming the as-synthesised phase is maintained.[233,234]

Finally, hydrazine introduces distinct system-level constraints. While hydrazine-coupled electrolysis can reduce the required cell voltage and enable application extensions (*e.g.*, wastewater contexts and hybrid configurations), translation beyond the laboratory requires careful attention to fuel logistics, containment, monitoring, and end-to-end process evaluation.[38] In addition, hydrazine's high toxicity necessitates stringent safety controls during handling and operation, reinforcing the importance of system design and risk management for scale-up.[37,88]

7 Conclusions and future perspectives

Hydrazine coupled electrolysis (OHzS) offers a highly promising approach for energy-efficient hydrogen production by leveraging the favourable thermodynamics of the HzOR to bypass the sluggish OER. Among transition metal-based catalysts, nickel-based materials stand out due to their abundance, redox versatility (Ni^{2+}/Ni^{3+}), and strong hydrazine adsorption capability. This review has systematically summarised recent

Open Access Article. Published on 12 May 2026. Downloaded on 6/5/2026 6:21:18 AM. This article is licensed under a Creative Commons Attribution 3.0 Unported Licence.

advances in the synthesis, structural design, and performance optimisation of Ni-based catalysts, including alloys, oxides/hydroxides, phosphides, chalcogenides, nitrides, and MOFs, for efficient HzOR and HER. Key strategies such as synergistic and interface engineering, electronic structure modulation, defect and vacancy engineering, surface reconfiguration, heterostructuring, and wettability control have been shown to significantly reduce overpotentials, accelerate reaction kinetics, and improve long-term stability. Furthermore, integrated bifunctional systems and hybrid electrolysers have achieved record-low operational voltages, enabling scalable hydrogen production in freshwater, seawater, and even neutral/acidic media. DFT calculations and *operando* characterisation have deepened mechanistic insights, reinforcing structure–property-performance relationships. Despite significant progress, several challenges and opportunities remain for advancing Ni-based catalysts toward practical hydrazine-assisted electrolysers. Fig. 12 presents a schematic roadmap summarising the future directions as follows:

• Atomic-scale interface and electronic structure optimisation; the catalytic performance of bifunctional Ni-based systems strongly depends on their local electronic environment. Future work should focus on precise interface design, heterostructuring, and lattice engineering to optimize N–H bond activation, ΔG_{H^*}, and hydrazine adsorption. Advanced synthetic approaches such as high-entropy alloying (*e.g.*, NiCoMoPtRu nanoclusters), atomic layer deposition, and controlled strain induction (*e.g.*, *via* nanotwinning or core–shell lattice mismatch) may unlock new levels of activity and stability. A particularly promising direction is the use of single-atom catalysts with isolated Ni sites on MXene or graphene supports, enabling near-100% atom utilisation and unique coordination environments that cannot be achieved with nanoparticles.

• Robust ctivity in non-alkaline electrolytes; most high-performance catalysts are evaluated in alkaline electrolytes (typically 1 M KOH), while neutral and acidic media remain severely underexplored. Developing acid-tolerant and corrosion-resistant Ni-based catalysts is crucial for practical applications, especially in seawater and wastewater matrices where pH can vary widely. Surface passivation strategies (*e.g.*, carbon coatings, hydrophobic layers), heteroatom doping (*e.g.*, with Cr or Mo), and core–shell architectures may help maintain activity while suppressing competing HER and metal dissolution. Future studies should systematically evaluate HzOR performance across pH 1–14 using standardised protocols, and explore gradient alloying to combine an acid-stable shell with an active Ni-rich core.

• *Operando* mechanistic studies: the multistep HzOR mechanism requires a deeper understanding under realistic conditions. Future research should integrate *operando* characterisation, such as X-ray Absorption Spectroscopy (XAS), Raman, Fourier Transform Infrared Spectroscopy (FTIR), Differential Electrochemical Mass Spectrometry (DEMS) and XPS, with theoretical modelling to identify true active sites, track dynamic restructuring, and unravel intermediate pathways. These insights will guide rational catalyst design beyond trial-and-error synthesis.

• High-current density and long-term stability: for industrial relevance, catalysts must maintain high performance at current densities >500–1000 mA cm^{-2} for extended operation (>150 h). Robust 3D nanoarchitectures, corrosion-resistant supports, and superaerophobic/hydrophilic surfaces are essential for fast mass transport, bubble removal, and mechanical durability. Future reports should include stability data at industrially relevant current densities rather than only at 10 mA cm^{-2}. Self-healing catalysts that dynamically repair surface defects or leached atoms *via* reversible Ni^{3+}/Ni^{3+} redox chemistry, as well as pulsed electrolysis protocols that periodically reverse potential to reduce surface poisoning, are emerging concepts that could dramatically extend catalyst lifetime.

• Sustainable and scalable synthesis: while many high-performance Ni-based catalysts rely on complex laboratory-scale syntheses (*e.g.*, multistep hydrothermal or solvothermal methods, high-temperature ammonolysis), scalable and cost-effective fabrication methods are needed for practical deployment. Approaches such as electrodeposition, roll-to-roll processing, continuous flow hydrothermal synthesis, and spray pyrolysis should be optimised for large-area, binder-free electrodes. Flash Joule heating (millisecond-scale thermal pulses) and plasma-engineered defect creation represent transformative techniques that can directly convert low-cost metal salts into defect-rich Ni-based catalysts in seconds, without solvents or lengthy annealing. Life-cycle assessment and techno-economic analysis will further guide sustainable implementation.

• Computational and ML approaches; computational and machine learning approaches. DFT calculations have been invaluable in revealing adsorption energetics and reaction barriers. Emerging ML methods, once supported by open datasets, can complement DFT by accelerating descriptor discovery, predicting stable catalyst phases, and enabling virtual high-throughput screening. Future work should focus on developing HzOR-specific descriptor libraries (d-band center, N–H bond dissociation energy, hydrazine deformation energy, N–N bond length change) and applying small data ML methods (SISSO, Gaussian process regression, random forest) to guide catalyst discovery. Graph neural networks and uncertainty-aware active learning can iteratively query the most informative DFT calculations, maximizing model accuracy with minimal computational cost. ML should serve as a supportive tool within broader experimental–theoretical frameworks rather than the sole driver of discovery. Integration with Renewable Energy and Environmental Applications; future studies should focus on coupling OHzS with renewable energy sources (*e.g.*, solar, wind) for decentralised hydrogen production. In parallel, testing catalysts in real wastewater or pollutant-rich environments can enable dual benefits of hydrogen generation and pollutant remediation. Designing selective, fouling-resistant catalysts will be critical for bridging laboratory advances with practical, sustainable energy systems.

In conclusion, the path forward for OHzS lies in a synergistic combination of advanced synthesis, *operando* mechanistic studies, scalable electrode design, and system-level integration. Computational methods, including DFT and ML, will play an

Open Access Article. Published on 12 May 2026. Downloaded on 6/5/2026 6:21:18 AM. This article is licensed under a Creative Commons Attribution 3.0 Unported Licence.

increasingly important role in guiding discovery, but practical advances will ultimately rely on the convergence of experimental innovation and engineering solutions. By embracing this multi-faceted approach, the field can accelerate the transition from laboratory-scale studies to efficient, durable, and commercially viable hydrazine-assisted hydrogen production systems.

Conflicts of interest

There are no conflicts to declare.

Data availability

No primary research results, software or code have been included and no new data were generated or analysed as part of this review.

Acknowledgements

P. L acknowledges the Natural Science Research Project of Universities in Anhui Province (2022AH050112), the Project of Anhui Provincial Department of Education (2022AH010004), and the Fund of Key Laboratory of Advanced Materials of the Ministry of Education No. Advmat-2401.

References

1 A. Mehtab, S. A. Ali, I. Sadiq, S. Shaheen, H. Khan, M. Fazil, N. A. Pandit, F. Naaz and T. Ahmad, *ACS Sustainable Resour. Manage.*, 2024, **1**, 604–620.
2 I. Dincer and M. I. Aydin, *Energy Convers. Manage.*, 2023, **283**, 116950.
3 S. Elahi and S. Seddighi, *J. Power Sources*, 2024, **609**, 234682.
4 I. Tariq, M. A. Asghar, A. Ali, A. Badshah, S. M. Abbas, W. Iqbal, M. Zubair, A. Haider and S. Zaman, *Catalysts*, 2022, **12**, 1242.
5 I. Tariq, A. Ali, A. Haider, W. Iqbal, M. A. Asghar, A. Badshah, M. A. Mansoor, T. Nisar, V. Wagner and S. M. Abbas, *Energy Technol.*, 2024, **12**, 2301504.
6 Y. Du, H. Wang, J. Chen, H. Chen, S. Wang and X. F. Lu, *Chem. Commun.*, 2025, **61**, 17854–17857.
7 S. Li, E. Li, X. An, X. Hao, Z. Jiang and G. Guan, *Nanoscale*, 2021, **13**, 12788–12817.
8 S. Aralekallu, L. K. Sannegowda, M. D. Kurkuri, R. K. Pai and H.-Y. Jung, *Sustain. Energy Fuels*, 2025, **9**, 2928–2940.
9 I. Tariq, W. Iqbal, A. Haider and M. Ma, *Int. J. Hydrogen Energy*, 2025, **142**, 40–53.
10 W. Iqbal, A. Hameed, I. Tariq, S. S. A. Shah and M. A. Nadeem, *Electrochim. Acta*, 2023, **467**, 143055.
11 J. Liu, Y. Du, D. Zheng, S. Wang, Y. Hou, J. Zhang and X. F. Lu, *ACS Mater. Lett.*, 2023, **6**, 466–481.
12 J. Liu, X. Liu, J. Zhang, Z. Liang, W. Lin and X. F. Lu, *ACS Catal.*, 2026, **16**, 7726–7737.
13 Y. Tong and P. Chen, *Inorg. Chem. Front.*, 2024, **11**, 6218–6245.
14 S. Zhang, X. Wei, S. Dai, H. Wang and M. Huang, *Adv. Funct. Mater.*, 2024, **34**, 2311370.
15 F. Liaqat, M. Jamil, I. Tariq, A. Haider and M. A. Khan, *J. Appl. Polym. Sci.*, 2023, **140**, e54112.
16 J. E. Troyan, *Ind. Eng. Chem.*, 1953, **45**, 2608–2612.
17 Y. Zhou, L. Zhang, X. Yang, G. Xu, C. Meng, G. Li, Y. Lin, C. Sun, N. Zhang and R. Yi, *Chem. Commun.*, 2025, **61**, 4739–4756.
18 T. Yu, G. Liu, T. Nie, Z. Wu, Z. Song, X. Sun and Y.-F. Song, *ACS Catal.*, 2024, **14**, 14937–14946.
19 J. Xu, M. Zhong, S. Yan, X. Chen, W. Li, M. Xu, C. Wang and X. Lu, *J. Colloid Interface Sci.*, 2025, **679**, 171–180.
20 A. M. A.-A. Otron, L.-H. Tran and J.-F. Blais, *Environ. Technol.*, 2025, **46**, 1369–1383.
21 Q. Sun, L. Wang, Y. Shen, M. Zhou, Y. Ma, Z. Wang and C. Zhao, *ACS Sustain. Chem. Eng.*, 2018, **6**, 12746–12754.
22 T. Y. Burshtein, Y. Yasman, L. Munoz-Moene, J. H. Zagal and D. Eisenberg, *ACS Catal.*, 2024, **14**, 2264–2283.
23 J. Zhang, X. Cao, M. Guo, H. Wang, M. Saunders, Y. Xiang, S. P. Jiang and S. Lu, *ACS Appl. Mater. Interfaces*, 2019, **11**, 19048–19055.
24 G. Liu, Z. Sun, X. Zhang, H. Wang, G. Wang, X. Wu, H. Zhang and H. Zhao, *J. Mater. Chem. A*, 2018, **6**, 19201–19209.
25 B. Liang, Y. Wang, X. Liu, T. Tan, L. Zhang and W. Wang, *J. Alloys Compd.*, 2019, **807**, 151648.
26 M. Du, H. Sun, J. Li, X. Ye, F. Yue, J. Yang, Y. Liu and F. Guo, *Chemelectrochem*, 2019, **6**, 5581–5587.
27 Y. Dong, P. Wang, J.-Y. Zhang, W. Song, Y. Chen, F. Wang, Y. Liu, C. Zhu and W. Li, *Sustain. Energy Fuels*, 2023, **7**, 84–91.
28 Z. Feng, H. Zhang, L. Wang, B. Gao, P. Lu and P. Xing, *J. Electroanal. Chem.*, 2020, **876**, 114740.
29 W. Liu, J. Xie, Y. Guo, S. Lou, L. Gao and B. Tang, *J. Mater. Chem. A*, 2019, **7**, 24437–24444.
30 X. Xu, H.-C. Chen, L. Li, M. Humayun, X. Zhang, H. Sun, D. P. Debecker, W. Zhang, L. Dai and C. Wang, *ACS Nano*, 2023, **17**, 10906–10917.
31 J. Li, S. Wang, J. Chang and L. Feng, *Adv. Powder Mater.*, 2022, **1**, 100030.
32 Y. Zhu, J. Zhang, Q. Qian, Y. Li, Z. Li, Y. Liu, C. Xiao, G. Zhang and Y. Xie, *Angew. Chem., Int. Ed.*, 2022, **61**, e202113082.
33 Q. Sun, Y. Li, J. Wang, B. Cao, Y. Yu, C. Zhou, G. Zhang, Z. Wang and C. Zhao, *J. Mater. Chem. A*, 2020, **8**, 21084–21093.
34 Y. Li, J. Li, Q. Qian, X. Jin, Y. Liu, Z. Li, Y. Zhu, Y. Guo and G. Zhang, *Small*, 2021, **17**, 2008148.
35 H. Liu, Y. Liu, M. Li, X. Liu and J. Luo, *Mater. Today Adv.*, 2020, **7**, 100083.
36 D. Khalafallah, M. Zhi and Z. Hong, *ChemCatChem*, 2021, **13**, 81–110.
37 S. Li, Y. Hou, L. Jiang, G. Feng, Y. Ge and Z. Huang, *Energy Rev.*, 2025, **4**, 100105.
38 H.-Y. Wang and Z.-Y. Yuan, *Mater. Horiz.*, 2025, **12**, 5123–5148.

Open Access Article. Published on 12 May 2026. Downloaded on 6/5/2026 6:21:18 AM. This article is licensed under a Creative Commons Attribution 3.0 Unported Licence.

39 J. Chi, L. Guo, J. Mao, T. Cui, J. Zhu, Y. Xia, J. Lai and L. Wang, *Adv. Funct. Mater.*, 2023, **33**, 2300625.
40 H. N. Nguyen MC USAF, J. A. Chenoweth, V. S. Bebarta MC USAF, T. E. Albertson, C. D. Nowadly and M. C. USAF, *Mil. Med.*, 2021, **186**, e319–e326.
41 Y. Wang, X. Yu, J. Xu, M. Zhong, J. Hao, M. Gao and X. Lu, *Chem. Eng. J.*, 2025, **505**, 159561.
42 X. Xu, H. C. Chen, L. Li, M. Humayun, X. Zhang, H. Sun, J. Jia, C. Xu, M. Bououdina and L. Sun, *Adv. Funct. Mater.*, 2024, **34**, 2408823.
43 S. Zhou, Y. Zhao, R. Shi, Y. Wang, A. Ashok, F. Héraly, T. Zhang and J. Yuan, *Adv. Mater.*, 2022, **34**, 2204388.
44 Q. Qian, J. Zhang, J. Li, Y. Li, X. Jin, Y. Zhu, Y. Liu, Z. Li, A. El-Harairy and C. Xiao, *Angew. Chem.*, 2021, **133**, 6049–6058.
45 M. Hao, C. Li, M. Wu, Q. Li, Z. Xiao, D. Shen and W. Wang, *J. Colloid Interface Sci.*, 2025, **679**, 966–974.
46 X. Wei, T. Wang, H. Dai and S. Li, *J. Alloys Compd.*, 2024, **997**, 174898.
47 X. Wang, W. Zhang, Q. Yu, X. Liu, Q. Liang, X. Meng, X. Wang and L. Wang, *Chem. Eng. J.*, 2022, **446**, 136987.
48 Y. Huang, X. Zhang, L. Li, M. Humayun, H. Zhang, X. Xu, S. P. Anthony, Z. Chen, J. Zeng and D. V. Shtansky, *Adv. Funct. Mater.*, 2025, **35**, 2401011.
49 F. Sun, J. Qin, Z. Wang, M. Yu, X. Wu, X. Sun and J. Qiu, *Nat. Commun.*, 2021, **12**, 4182.
50 H. Qin, G. Lin, J. Zhang, X. Cao, W. Xia, H. Yang, K. Yuan, T. Jin, Q. Wang and L. Jiao, *Adv. Mater.*, 2025, **37**, 2417593.
51 D. Shao, Q. Wang, X. Yao, Y. Zhou and X.-Y. Yu, *J. Mater. Chem. A*, 2022, **10**, 21848–21855.
52 T. Zhang and T. Asefa, *Adv. Mater.*, 2019, **31**, 1804394.
53 P. Tang, H. Wen and P. Wang, *Chem. Eng. J.*, 2022, **431**, 134123.
54 A. Wittstock, A. Wichmann and M. Baumer, *ACS Catal.*, 2012, **2**, 2199–2215.
55 Y.-Y. Tang, C.-L. Kao and P.-Y. Chen, *Anal. Chim. Acta*, 2012, **711**, 32–39.
56 J. Wang, A. Khaniya, L. Hu, M. J. Beazley, W. E. Kaden and X. Feng, *J. Mater. Chem. A*, 2018, **6**, 18050–18056.
57 R.-Q. Li, S. Guo, X. Wang, X. Wan, S. Xie, Y. Liu, C. Wang, G. Zhang, J. Cao and J. Dai, *Chem. Sci.*, 2024, **15**, 10084–10091.
58 N. K. Katiyar, S. Dhakar, A. Parui, P. Gakhad, A. K. Singh, K. Biswas, C. S. Tiwary and S. Sharma, *ACS Catal.*, 2021, **11**, 14000–14007.
59 S. S. Narayanan and F. Scholz, *Electroanalysis: an International Journal Devoted to Fundamental and Practical Aspects of Electroanalysis*, 1999, vol. 11, pp. 465–469.
60 Y. Xu and B. Zhang, *Chemelectrochem*, 2019, **6**, 3214–3226.
61 A. Bard, *Anal. Chem.*, 1963, **35**, 1602–1607.
62 J. Stetter, K. Blurton, A. Valentine and K. Tellefsen, *J. Electrochem. Soc.*, 1978, **125**, 1804–1807.
63 J. Yang, L. Xu, W. Zhu, M. Xie, F. Liao, T. Cheng, Z. Kang and M. Shao, *J. Mater. Chem. A*, 2022, **10**, 1891–1898.
64 W. Q. Zaman, W. Sun, M. Tariq, Z. Zhou, U. Farooq, Z. Abbas, L. Cao and J. Yang, *Appl. Catal., B*, 2019, **244**, 295–302.
65 R. A. Krivina, Y. Ou, Q. Xu, L. P. Twight, T. N. Stovall and S. W. Boettcher, *Acc. Mater. Res.*, 2021, **2**, 548–558.
66 W. Xiong, H. Yin, T. Wu and H. Li, *Chem.–Eur. J.*, 2023, **29**, e202202872.
67 Y. Liu, X. Er, X. Wang, H. Ren, W. Wang, F. Cao, T. Zhang, P. Liu, Y. Yuan and F. Yu, *Nano-Micro Lett.*, 2025, **17**, 329.
68 Y. Chen, X. Zhan, S. L. Bueno, I. H. Shafei, H. M. Ashberry, K. Chatterjee, L. Xu, Y. Tang and S. E. Skrabalak, *Nanoscale Horiz.*, 2021, **6**, 231–237.
69 P. Kumar, A. P. Murthy, L. S. Bezerra, B. K. Martini, G. Maia and J. Madhavan, *Int. J. Hydrogen Energy*, 2021, **46**, 622–632.
70 E. E. Siddharthan, S. Ghosh and R. Thapa, *ACS Appl. Energy Mater.*, 2023, **6**, 8941–8948.
71 Q. Zhang, Y. Li, F. Luo and Z. Yang, *Chem. Commun.*, 2025, **61**, 10747–10763.
72 G. Meng, Z. Chang, L. Zhu, C. Chen, Y. Chen, H. Tian, W. Luo, W. Sun, X. Cui and J. Shi, *Nano-Micro Lett.*, 2023, **15**, 212.
73 W. Zhu, A. G. Naidu, Q. Wu, H. Yan, M. Zhao, Z. Wang and H. Liang, *Chem. Eng. Sci.*, 2022, **258**, 117769.
74 Z. Zhou, Z. Pei, L. Wei, S. Zhao, X. Jian and Y. Chen, *Energy Environ. Sci.*, 2020, **13**, 3185–3206.
75 Z. Yu, C. Si, F. Sabaté, A. P. LaGrow, Z. Tai, V. M. Diaconescu, L. Simonelli, L. Meng, M. J. Sabater and B. Li, *Chem. Eng. J.*, 2023, **470**, 144050.
76 J. Li, Y. Ma, X. Mu, X. Wang, Y. Li, H. Ma and Z. Guo, *Advanced Science*, 2025, **12**, 2411964.
77 J.-F. Liu, H. Wen, Z.-Y. Zhang and P. Wang, *J. Mater. Chem. A*, 2023, **11**, 14213–14220.
78 Y. Liu, X. Hong, X. Liu, W. Chen and J. Tang, *ACS Sustain. Chem. Eng.*, 2024, **12**, 11520–11530.
79 F.-X. Yan, H.-Y. Wang, L. Wang, H. Wang and Z.-Y. Yuan, *Inorg. Chem. Front.*, 2024, **11**, 6376–6386.
80 H.-H. Wu, H. Huang, J. Zhong, S. Yu, Q. Zhang and X. C. Zeng, *Nanoscale*, 2019, **11**, 12210–12219.
81 L. Chen, J. T. Ren and Z. Y. Yuan, *Adv. Energy Mater.*, 2023, **13**, 2203720.
82 B. Xu, J. Liang, X. Sun and X. Xiong, *Green Chem.*, 2023, **25**, 3767–3790.
83 L. Zhao, Y. Li, M. Yu, Y. Peng and F. Ran, *Advanced Science*, 2023, **10**, 2300283.
84 L. Zhu, J. Huang, G. Meng, T. Wu, C. Chen, H. Tian, Y. Chen, F. Kong, Z. Chang and X. Cui, *Nat. Commun.*, 2023, **14**, 1997.
85 C. Liu, S. Wu, Y. Yang, J. Wei, S. Chen, X. Q. Sun, S. Luo, M. B. Hussain, R. Feng and X. Z. Fu, *Adv. Funct. Mater.*, 2025, **35**, 2422634.
86 T. H. Nguyen, D. T. Tran, D. Malhotra, P. K. L. Tran, V. A. Dinh, T. T. N. Ta, C. L. Dong, N. H. Kim and J. H. Lee, *Small*, 2025, **21**, 2502553.
87 J. K. Niemeier and D. P. Kjell, *Org. Process Res. Dev.*, 2013, **17**, 1580–1590.
88 H. N. Nguyen, J. A. Chenoweth, V. S. Bebarta, T. E. Albertson and C. D. Nowadly, *Mil. Med.*, 2021, **186**, e319–e326.
89 X. Zhai, Q. Yu, J. Chi, X. Wang, B. Li, B. Yang, Z. Li, J. Lai and L. Wang, *Nano Energy*, 2023, **105**, 108008.

Open Access Article. Published on 12 May 2026. Downloaded on 6/5/2026 6:21:18 AM. This article is licensed under a Creative Commons Attribution 3.0 Unported Licence.

90 M. A. Ahsan, T. He, J. C. Noveron, K. Reuter, A. R. Puente-Santiago and R. Luque, *Chem. Soc. Rev.*, 2022, **51**, 812–828.
91 Y. Liu, J. Zhang, Y. Li, Q. Qian, Z. Li and G. Zhang, *Adv. Funct. Mater.*, 2021, **31**, 2103673.
92 P. J. Sharma, K. K. Joshi, P. Sahatiya, C. Sumesh and P. M. Pataniya, *J. Mater. Chem. A*, 2025, **13**, 9865–9877.
93 R. Guo, Y. Zhang, X. Zhang, H. Yang and T. Hu, *Chem. Eng. J.*, 2024, **491**, 152028.
94 N. Zhao, W. Luo, S. Li, H. Wang, Y. Mao, Y. Jiang, W. Wang, M. Li, W. Su and R. He, *Adv. Sci.*, 2025, **12**, 2411526.
95 J. Zhang, Y. Liu, J. Li, X. Jin, Y. Li, Q. Qian, Y. Wang, A. El-Harairy, Z. Li and Y. Zhu, *ACS Appl. Mater. Interfaces*, 2021, **13**, 3881–3890.
96 U. P. Suryawanshi, U. V. Ghorpade, P. V. Kumar, J. S. Jang, M. He, H. J. Shim, H. R. Jung, M. P. Suryawanshi and J. H. Kim, *Appl. Catal., B*, 2024, **355**, 124165.
97 J. P. Perdew, K. Burke and M. Ernzerhof, *Phys. Rev. Lett.*, 1996, **77**, 3865.
98 V. Ulevičienė, A. Balčiūnaitė, D. Upskuvienė, A. Plavniece, A. Volperts, G. Dobele, A. Zhurinsh, G. Niaura, L. Tamašauskaitė-Tamašiūnaitė and E. Norkus, *Catalysts*, 2025, **15**, 400.
99 G. Liu, Z. Wang, T. Shen, X. Zheng, Y. Zhao and Y.-F. Song, *Nanoscale*, 2021, **13**, 1869–1874.
100 T. Shi, B. Gao, H. Meng, Y. Fu, D. Kong, P. Ren, H. Fu and Z. Feng, *Green Chem.*, 2024, **26**, 4209–4220.
101 A. A. Kashale, A. S. Rasal, F.-C. Hsu, C. Chen, S. N. Kulkarni, C. H. Chang, J.-Y. Chang, Y. Lai and I.-W. P. Chen, *J. Colloid Interface Sci.*, 2023, **640**, 737–749.
102 S. Song, Y. Li, Y. Shi, Y. Xu and Y. Niu, *J. Electroanal. Chem.*, 2022, **906**, 115986.
103 S. Taghaddosi, S. Rezaee and S. Shahrokhian, *J. Electroanal. Chem.*, 2020, **873**, 114437.
104 T. Mohammadi, K. Asadpour-Zeynali, M. R. Majidi and M. G. Hosseini, *Heliyon*, 2023, **9**(6), e16888.
105 E. A. Vorms, V. Papaefthymiou, T. Faverge, A. Bonnefont, M. Chatenet, E. R. Savinova and A. G. Oshchepkov, *Electrochim. Acta*, 2024, **507**, 145056.
106 J. Yu, X. Li, Q. Zhang, W. Li, M. Zhou, Y. Zhang and P. Xiao, *Appl. Catal., B*, 2025, **373**, 125374.
107 Z. Feng, T. Shi, W. Liu, W. Zhang and H. Zhang, *Int. J. Energy Res.*, 2022, **46**, 15938–15947.
108 P. E. Blöchl, *Phys. Rev. B: Condens. Matter Mater. Phys.*, 1994, **50**, 17953.
109 X. Wei, T. Wang, H. Dai and S. Li, *ACS Appl. Energy Mater.*, 2024, **7**, 5202–5208.
110 S. L. Dudarev, G. A. Botton, S. Y. Savrasov, C. Humphreys and A. P. Sutton, *Phys. Rev. B: Condens. Matter Mater. Phys.*, 1998, **57**, 1505.
111 K. Mathew, R. Sundararaman, K. Letchworth-Weaver, T. Arias and R. G. Hennig, *J. Chem. Phys.*, 2014, **140**, 084106.
112 M. M. Melander, T. Wu, T. Weckman and K. Honkala, *npj Comput. Mater.*, 2024, **10**, 5.
113 M. Jafarian, T. Rostami, M. Mahjani and F. Gobal, *J. Electroanal. Chem.*, 2016, **763**, 134–140.
114 Q. Sun, M. Zhou, Y. Shen, L. Wang, Y. Ma, Y. Li, X. Bo, Z. Wang and C. Zhao, *J. Catal.*, 2019, **373**, 180–189.
115 Q. Qian, Y. Li, Y. Liu, Y. Guo, Z. Li, Y. Zhu and G. Zhang, *Chem. Eng. J.*, 2021, **414**, 128818.
116 Y. Zhao, Y. Sun, H. Li, S. Zeng, R. Li, Q. Yao, H. Chen, Y. Zheng and K. Qu, *J. Colloid Interface Sci.*, 2023, **652**, 1848–1856.
117 M. Zhang, B. Zhou, Y. Gong, M. Shang, W. Xiao, J. Wang, C. Dai, H. Zhang, Z. Wu and L. Wang, *J. Colloid Interface Sci.*, 2024, **667**, 73–81.
118 T. Wang, Y. Cao, H. Wu, C. Feng, Y. Ding and H. Mei, *Int. J. Hydrogen Energy*, 2022, **47**, 5766–5778.
119 X. Wei, H. Dai, C. Liu and S. Li, *Prog. Nat. Sci. Mater. Int.*, 2023, **33**, 710–717.
120 G. Feng, Y. Pan, D. Su and D. Xia, *Adv. Mater.*, 2024, **36**, 2309715.
121 Z. Xiao, J. Wang, H. Lu, Y. Qian, Q. Zhang, A. Tang and H. Yang, *J. Mater. Chem. A*, 2023, **11**, 15749–15759.
122 L. Guo, Q. Yu, X. Zhai, J. Chi, T. Cui, Y. Zhang, J. Lai and L. Wang, *Nano Res.*, 2022, **15**, 8846–8856.
123 K. Wang, C. Liang, Z. Yi, F. Xu, Y. Wang, L. Lei, L. Zhuang and Z. Xu, *Sci. China Mater.*, 2023, **66**, 3846–3854.
124 K. Li, J. He, X. Guan, Y. Tong, Y. Ye, L. Chen and P. Chen, *Small*, 2023, **19**, 2302130.
125 Z. Feng, H. Meng, Y. Fu, L. Ren, B. Gao and W. Liu, *Small*, 2024, **20**, 2403270.
126 A. P. Sundar Rajan, R. A. Senthil, C. J. Moon, A. Kumar, A. Min, M. Ubaidullah and M. Y. Choi, *Small Methods*, 2025, **9**, 2401709.
127 H. Zhang, Z. Feng, L. Wang, D. Li and P. Xing, *Nanotechnology*, 2020, **31**, 365701.
128 J. Wang, S. Qing, X. Tong, T. Xiang, G. Luo, K. Zhang and L. Xu, *Green Energy Environ.*, 2025, **10**(10), 1957–1967.
129 Z. Zhao, Z. Li, Z. Zhang and X. Meng, *Appl. Catal., B*, 2024, **347**, 123805.
130 M. Zhou, Z. Yu, G. Yu, R. Fu, S. Wang, W. Yang, X. Liao, Y. Zhao and Z. Wang, *Adv. Funct. Mater.*, 2025, **35**, 2415058.
131 Y. Chang, L. Kong, D. Xu, X. Lu, S. Wang, Y. Li, J. Bao, Y. Wang and Y. Liu, *Angew. Chem., Int. Ed.*, 2025, **64**, e202414234.
132 B. Li, K. Wang, J. Ren and P. Qu, *New J. Chem.*, 2022, **46**, 7615–7625.
133 B. Singh, R. Kumar, T. Ansari, A. Indra and A. Draksharapu, *Chem. Commun.*, 2024, **60**, 9432–9435.
134 X. Leng, L. Zhao, W. Shi, J. Lian and X. Zhang, *ACS Appl. Energy Mater.*, 2024, **7**, 6248–6257.
135 Z. Wang, L. Xu, F. Huang, L. Qu, J. Li, K. A. Owusu, Z. Liu, Z. Lin, B. Xiang and X. Liu, *Adv. Energy Mater.*, 2019, **9**, 1900390.
136 H. Jin, X. Wang, C. Tang, A. Vasileff, L. Li, A. Slattery and S. Z. Qiao, *Adv. Mater.*, 2021, **33**, 2007508.
137 R.-Q. Li, S. Zeng, B. Sang, C. Xue, K. Qu, Y. Zhang, W. Zhang, G. Zhang, X. Liu and J. Deng, *Nano Res.*, 2023, **16**, 2543–2550.
138 M. Zabihinezhad, T. Shahrabi, C. Zheng, T. Shao, G. B. Darband and J. Li, *Appl. Catal., A*, 2023, **666**, 119415.
139 G. B. Darband, N. Lotfi, A. Aliabadi, S. Hyun and S. Shanmugam, *Electrochim. Acta*, 2021, **382**, 138335.

Open Access Article. Published on 12 May 2026. Downloaded on 6/5/2026 6:21:18 AM. This article is licensed under a Creative Commons Attribution 3.0 Unported Licence.

140 A. Zhang, H. Liu and C. Wang, *Electrochim. Acta*, 2022, **435**, 141406.
141 M. A. Kenari, A. S. Rouhaghdam and G. B. Darband, *J. Colloid Interface Sci.*, 2025, **678**, 828–841.
142 S. Zhang, C. Zhang, X. Zheng, G. Su, H. Wang and M. Huang, *Appl. Catal., B*, 2023, **324**, 122207.
143 G. B. Darband, M. Maleki, A. Toghraei and S. Shanmugam, *Int. J. Hydrogen Energy*, 2023, **48**, 4253–4263.
144 H.-M. Yang, H.-Y. Wang, M.-L. Sun and Z.-Y. Yuan, *Chem. Eng. J.*, 2023, **475**, 146134.
145 H.-M. Yang, H.-Y. Wang, S. Zhai, J.-T. Ren and Z.-Y. Yuan, *Chem. Eng. J.*, 2024, **489**, 151236.
146 B. Zhou, M. Li, Y. Li, Y. Liu, Y. Lu, W. Li, Y. Wu, J. Huo, Y. Wang and L. Tao, *Chin. J. Catal.*, 2022, **43**, 1131–1138.
147 Y. Yang, X. Li, G. Liu, H. Liu, Y. Shi, C. Ye, Z. Fang, M. Ye and J. Shen, *Adv. Mater.*, 2024, **36**, 2307979.
148 Y. Hu, T. Chao, Y. Li, P. Liu, T. Zhao, G. Yu, C. Chen, X. Liang, H. Jin and S. Niu, *Angew. Chem., Int. Ed.*, 2023, **62**, e202308800.
149 J. Hou, K. Mei, T. Jiang, X. Yu and M. Wu, *Dalton Trans.*, 2024, **53**, 4574–4579.
150 K. Li, G. Zhou, Y. Tong, Y. Ye and P. Chen, *ACS Sustain. Chem. Eng.*, 2023, **11**, 14186–14196.
151 H.-Y. Wang, L. Wang, J.-T. Ren, W. Tian, M. Sun, Y. Feng and Z.-Y. Yuan, *ACS Nano*, 2023, **17**, 10965–10975.
152 A. E. Praveen, S. Ganguli, D. Sarkar and V. Mahalingam, *Inorg. Chem.*, 2022, **61**, 4394–4403.
153 W. Liu, W. Liu, T. Hou, J. Ding, Z. Wang, R. Yin, X. San, L. Feng, J. Luo and X. Liu, *Nano Res.*, 2024, **17**, 4797–4806.
154 C. Feng, M. Lv, J. Shao, H. Wu, W. Zhou, S. Qi, C. Deng, X. Chai, H. Yang and Q. Hu, *Adv. Mater.*, 2023, **35**, 2305598.
155 X. Ren and Y. Tong, *Int. J. Hydrogen Energy*, 2024, **49**, 489–497.
156 N. Nwaji, B. Fikadu, M. Osial, Z. M. Goudarzi, S. Asgaran, L. T. Tufa, J. Lee and M. Giersig, *Int. J. Hydrogen Energy*, 2024, **86**, 554–563.
157 Z. Liu, Y. Li, H. Guo, J. Zhao, H. Zhang and R. Song, *J. Mater. Chem. A*, 2023, **11**, 24667–24677.
158 X. Gao, R. He, J. Du, D. Zhou, A. Chen and X. Sun, *ACS Catal.*, 2022, **12**, 14387–14397.
159 A. E. Praveen, V. Mishra, S. Ganguli, A. Chandrasekar and V. Mahalingam, *Inorg. Chem.*, 2023, **62**, 16149–16160.
160 W. Liu, T. Shi and Z. Feng, *J. Colloid Interface Sci.*, 2023, **630**, 888–899.
161 J. Mao, W. Wang, J. Kang, K. Fang, Y. Shao and J. Yuan, *Int. J. Hydrogen Energy*, 2024, **78**, 1048–1059.
162 D. Khalafallah, Y. Zhang and Q. Zhang, *FlatChem*, 2024, **43**, 100602.
163 Y. Li, Y. Zhao, F.-M. Li, Z. Dang and P. Gao, *ACS Appl. Mater. Interfaces*, 2021, **13**, 34457–34467.
164 H.-Y. Wang, L. Wang, J.-T. Ren, W.-W. Tian, M.-L. Sun and Z.-Y. Yuan, *Nano-Micro Lett.*, 2023, **15**, 155.
165 S. Verma, L. Singh, A. Goyal, B. Singh and A. Draksharapu, *ACS Appl. Nano Mater.*, 2025, **8**, 13522–13531.
166 J. Zhao, H. Guo, Q. Zhang, Y. Li, L. Gu and R. Song, *Appl. Catal., B*, 2023, **325**, 122354.
167 X. H. Chen, H. C. Fu, L. L. Wu, X. L. Li, B. Yang, T. Li, F. Gu, J. L. Lei, N. B. Li and H. Q. Luo, *Green Chem.*, 2022, **24**, 5559–5569.
168 H. Lee, J. Theerthagiri, M. A. Kumari, A. Min, C. J. Moon, V. Anbazhagan, R. L. Brutchey and M. Y. Choi, *Int. J. Hydrogen Energy*, 2024, **57**, 176–186.
169 Y. Zhu, Y. Chen, Y. Feng, X. Meng, J. Xia and G. Zhang, *Adv. Mater.*, 2024, **36**, 2401694.
170 X. Zhai, Q. Yu, G. Liu, J. Bi, Y. Zhang, J. Chi, J. Lai, B. Yang and L. Wang, *J. Mater. Chem. A*, 2021, **9**, 27424–27433.
171 Q. Yu, J. Chi, G. Liu, X. Wang, X. Liu, Z. Li, Y. Deng, X. Wang and L. Wang, *Sci. China Mater.*, 2022, **65**, 1539–1549.
172 J. Wei, Y. Song, M. Gan, G. An, Y. Shen, X. Zhao, Y. Zhang, P. Liu, B. Xu and J. Guo, *Sustain. Mater. Technol.*, 2025, e01413.
173 C. Wei, S. Sun, D. Mandler, X. Wang, S. Z. Qiao and Z. J. Xu, *Chem. Soc. Rev.*, 2019, **48**, 2518–2534.
174 S. Anantharaj, P. E. Karthik and S. Noda, *Angew. Chem., Int. Ed.*, 2021, **60**, 23051–23067.
175 V.-H. Do and J.-M. Lee, *Chem. Soc. Rev.*, 2024, **53**, 2693–2737.
176 M. S. Ratsoma, B. L. Poho, K. Makgopa, K. Raju, K. D. Modibane, C. J. Jafta and K. O. Oyedotun, *J. Electron. Mater.*, 2023, **52**, 2264–2291.
177 L. Zhang, R. Iwata, Z. Lu, X. Wang, C. D. Díaz-Marín and Y. Zhong, *Chem. Rev.*, 2024, **124**, 10052–10111.
178 X. Zhao, H. Ren and L. Luo, *Langmuir*, 2019, **35**, 5392–5408.
179 E. W. Schmidt, *Hydrazine and its Derivatives: Preparation, Properties, Applications, 2 Volume Set*, John Wiley & Sons, 2001.
180 A. H. Wani and A. Sharma, in *Electrocatalytic Materials*, Springer, 2024, pp. 247–269.
181 D. Khalafallah, F. Lai, H. Huang, J. Wang, X. Wang, Q. Zhang and S. Tong, *Mater. Chem. Front.*, 2025, **9**, 2322–2353.
182 R. Ding, J. Chen, Y. Chen, J. Liu, Y. Bando and X. Wang, *Chem. Soc. Rev.*, 2024, **53**, 11390–11461.
183 J. Benavides-Hernandez and F. Dumeignil, *ACS Catal.*, 2024, **14**, 11749–11779.
184 R. Batra, T. D. Loeffler, H. Chan, S. Srinivasan, H. Cui, I. V. Korendovych, V. Nanda, L. C. Palmer, L. A. Solomon and H. C. Fry, *Nat. Chem.*, 2022, **14**, 1427–1435.
185 M. Karthikeyan, D. M. Mahapatra, A. S. A. Razak, A. A. Abahussain, B. Ethiraj and L. Singh, *Catal. Rev.*, 2024, **66**, 997–1027.
186 Y. Zhao, S.-S. Gao, P.-H. Ren, L.-S. Ma and X.-B. Chen, *J. Mater. Chem. A*, 2025, **13**, 4186–4196.
187 H. Adamu, S. I. Abba, P. B. Anyin, Y. Sani, Z. H. Yamani and M. Qamar, *ACS Mater. Lett.*, 2022, **5**, 299–320.
188 S. Zhao, Z. X. Li, H. T. Guo, J. Li, Z. L. Liu, P. F. Wang, L. L. Wang and T. F. Yi, *Adv. Funct. Mater.*, 2025, e09799.
189 S. Bai, C. Ning, G. Liu, Y. Xu, Z. Wu and Y.-F. Song, *J. Mater. Chem. A*, 2025, **13**, 36825–36852.
190 T. Wang, Q. Wu, Y. Han, Z. Guo, J. Chen and C. Liu, *Appl. Phys. Rev.*, 2025, **12**, 011316.
191 A. Badreldin, O. Bouhali and A. Abdel-Wahab, *Adv. Funct. Mater.*, 2024, **34**, 2312425.

 This journal is © The Royal Society of Chemistry 2026

Open Access Article. Published on 12 May 2026. Downloaded on 6/5/2026 6:21:18 AM. This article is licensed under a Creative Commons Attribution 3.0 Unported Licence.

192 K. Tran and Z. W. Ulissi, *Nat. Catal.*, 2018, **1**, 696–703.
193 A. Palizhati, W. Zhong, K. Tran, S. Back and Z. W. Ulissi, *J. Chem. Inf. Model.*, 2019, **59**, 4742–4749.
194 V. Fung, G. Hu, P. Ganesh and B. G. Sumpter, *Nat. Commun.*, 2021, **12**, 88.
195 G. Yin, H. Zhu, S. Chen, T. Li, C. Wu, S. Jia, J. Shang, Z. Ren, T. Ding and Y. Li, *Molecules*, 2025, **30**, 759.
196 S. Ram, A. S. Lee, S.-C. Lee and S. Bhattacharjee, *Chem. Mater.*, 2025, **37**, 3608–3621.
197 C. Y. J. Lim, R. I. Made, Z. H. J. Khoo, C. K. Ng, Y. Bai, J. Wang, G. Yang, A. D. Handoko and Y.-F. Lim, *Mater. Horiz.*, 2023, **10**, 5022–5031.
198 R. B. Wexler, J. M. P. Martirez and A. M. Rappe, *J. Am. Chem. Soc.*, 2018, **140**, 4678–4683.
199 N. K. Pandit, D. Roy, S. C. Mandal and B. Pathak, *J. Phys. Chem. Lett.*, 2022, **13**, 7583–7593.
200 B. M. Abraham, M. V. Jyothirmai, P. Sinha, F. Viñes, J. K. Singh and F. Illas, *Wiley Interdiscip. Rev.: Comput. Mol. Sci.*, 2024, **14**, e1730.
201 P. Schlexer Lamoureux, K. T. Winther, J. A. Garrido Torres, V. Streibel, M. Zhao, M. Bajdich, F. Abild-Pedersen and T. Bligaard, *ChemCatChem*, 2019, **11**, 3581–3601.
202 M. Wang and H. Zhu, *ACS Catal.*, 2021, **11**, 3930–3937.
203 C. Wei, D. Shi, F. Zhou, Z. Yang, Z. Zhang, Z. Xue and T. Mu, *Phys. Chem. Chem. Phys.*, 2023, **25**, 7917–7926.
204 C. Chen, B. Xiao, Z. Qin, J. Zhao, W. Li, Q. Li and X. Yu, *ACS Appl. Mater. Interfaces*, 2023, **15**, 40538–40548.
205 D. Zhang, H. Li, H. Lu, Z. Yin, Z. Fusco, A. Riaz, K. Reuter, K. Catchpole and S. Karuturi, *Energy Environ. Sci.*, 2023, **16**, 5065–5075.
206 M. J. Pei, X. Gao, Y. K. Shuai, J. M. Xu, J. C. Chen, Q. Zeng, Y. Liu, W. Yan and J. Zhang, *Small*, 2025, 2506357.
207 Z. Fang, S. Li, Y. Zhang, Y. Wang, K. Meng, C. Huang and S. Sun, *J. Phys. Chem. Lett.*, 2024, **15**, 281–289.
208 A. Fatima, M. Asad, G. Eid, F. Zafar, M. M. Alsabban, M. M. H. Maqbool, N. Akhtar, M. A. Khan, C. Yu and M. M. El-Toony, *Energy Fuels*, 2025, **39**, 5877–5885.
209 X. Jiang, Y. Wang, B. Jia, X. Qu and M. Qin, *ACS Omega*, 2022, **7**, 14160–14164.
210 S. Iqbal, K. Aftab, M. A. Khan, M. R. Khan, N. Javed, F. T. Jannat, N. Ahmad and M. Hussain, *Int. J. Hydrogen Energy*, 2025, **174**, 151403.
211 K. Boonpalit and N. Artrith, *arXiv*, 2024, preprint, arXiv:2412.15452, DOI: 10.48550/arXiv.2412.15452.
212 A. L. Maulana, S. Han, Y. Shan, P.-C. Chen, C. Lizandara-Pueyo, S. De, K. Schierle-Arndt and P. Yang, *J. Am. Chem. Soc.*, 2025, **147**, 10268–10278.
213 R. Ouyang, S. Curtarolo, E. Ahmetcik, M. Scheffler and L. M. Ghiringhelli, *Phys. Rev. Mater.*, 2018, **2**, 083802.
214 A. S. Nair, L. Foppa and M. Scheffler, *npj Comput. Mater.*, 2025, **11**, 150.
215 N. Raza, S. Pervaiz and U. Haroon, *Next Research*, 2025, p. 00778.
216 L. Ge, H. Yuan, Y. Min, L. Li, S. Chen, L. Xu and W. Goddard, *J. Phys. Chem. Lett.*, 2020, **11**, 869–876.
217 B. Wang and F. Zhang, *Angew. Chem., Int. Ed.*, 2022, **61**, e202111026.
218 M. Tamtaji, H. Gao, M. D. Hossain, P. R. Galligan, H. Wong, Z. Liu, H. Liu, Y. Cai, W. A. Goddard and Z. Luo, *J. Mater. Chem. A*, 2022, **10**, 15309–15331.
219 H. Mai, T. C. Le, D. Chen, D. A. Winkler and R. A. Caruso, *Chem. Rev.*, 2022, **122**, 13478–13515.
220 M. Andersen and K. Reuter, *Acc. Chem. Res.*, 2021, **54**, 2741–2749.
221 S. Wang and J. Jiang, *ACS Catal.*, 2023, **13**, 7428–7436.
222 W. Xu, M. Andersen and K. Reuter, *ACS Catal.*, 2020, **11**, 734–742.
223 J. Krzywanski, M. Sosnowski, K. Grabowska, A. Zylka, L. Lasek and A. Kijo-Kleczkowska, *Materials*, 2024, **17**, 3521.
224 E. Topal, Z. Liao, M. Löffler, J. Gluch, J. Zhang, X. Feng and E. Zschech, *BMC Mater.*, 2020, **2**, 5.
225 J. Zhang, P. Hu and H. Wang, *J. Phys. Chem. C*, 2020, **124**, 10483–10494.
226 V. Fung, G. Hu, Z. Wu and D.-e. Jiang, *J. Phys. Chem. C*, 2020, **124**, 19571–19578.
227 T. Fukushima, K. Tsuchimoto, M. Itatani and K. Murakoshi, *Electrochemistry*, 2025, **93**, 094013.
228 Y. Liu, J. Sun, Y. Chai, Y. Yang and Z. Yang, *J. Mater. Sci.*, 2025, **60**, 2863–2877.
229 M. B. Kale, R. A. Borse, A. Gomaa Abdelkader Mohamed and Y. Wang, *Adv. Funct. Mater.*, 2021, **31**, 2101313.
230 S. S. Koshy, J. Rath and A. Kiani, *Heliyon*, 2024, **10**, e37188.
231 S. S. Kumar and H. Lim, *Energy Rep.*, 2022, **8**, 13793–13813.
232 Q. Wen, Y. Zhao, Y. Liu, H. Li and T. Zhai, *Small*, 2022, **18**, 2104513.
233 D. Hochfilzer, I. Chorkendorff and J. Kibsgaard, *ACS Energy Lett.*, 2023, **8**, 1607–1612.
234 W. Zhai, Y. Ma, D. Chen, J. C. Ho, Z. Dai and Y. Qu, *InfoMat*, 2022, **4**, e12357.